USING FOREST STRUCTURE TO MODEL VERTICAL VARIATIONS OF CANOPY RADIATION AND PRODUCTIVITY

by

Martin van Leeuwen

B.Sc., Wageningen University, 2005

M.Sc., Wageningen University, 2007

M.Sc.Agr., University College Dublin, 2009

A THESIS SUBMITTED IN PARTIAL FULFILLMENT OF THE REQUIREMENTS FOR THE DEGREE OF

DOCTOR OF PHILOSOPHY

in

The Faculty of Graduate and Postdoctoral Studies

(Forestry)

THE UNIVERSITY OF BRITISH COLUMBIA

(Vancouver)

January 2014

Abstract

The productivity of autotrophic organisms affects all life on Earth; hence, gaining insight in the variability of autotrophic productivity has received significant research interest. At cell to organism level, much knowledge has been gained under controlled conditions through laboratory analysis. At the stand level and beyond, control over the driving variables is limited, and hence experiments have relied on extensive time series, and geospatial analysis to observe changes in productivity across a wide range of environmental conditions. Significant technologies at these scales are eddy covariance that provides point sample estimates of productivity by measuring CO_2 fluxes between land and atmosphere, and remote sensing that provides for extrapolating eddy-covariance measurements across the landscape using canopy-reflectance data. Challenges in fusing eddy covariance with remote sensing relate to the limited capacity of airborne and spaceborne instruments to observe changes in the biophysical state of deep canopy strata; hence, eddy-covariance estimates that capture the productivity of an arbitrarily dense canopy volume are extrapolated based on top-of-canopy reflectance data. Proximal-sensing technology extends the acquisition of reflectance data to arbitrary locations within the canopy; however, these data are affected by the immediate canopy structure surrounding the sensor that introduces a sensor-location bias, and the direct use of these data in stand-level models is therefore challenging. This thesis explores the simulation of photosynthetic down-regulation using geometrically explicit forest models and meteorological records. The geometrically explicit models are constructed by combining laser-scanning data with tree-regeneration models, and are used to simulate a time series of leaf-level incident radiation. The parameters of a leaf-level photosynthesis model are then optimized against eddy-covariance productivity estimates. Finally, the potential of geometrically explicit models for the fusion of remote sensing and proximal sensing data is discussed.

Preface

This dissertation contains three scientific papers of which I am the first author. The initial project overview was proposed by my supervisor, Dr. Nicholas Coops. Ground-based laser scanning data were collected by members of the Faculty of Forestry, The University of British Columbia, Vancouver, and the Commonwealth Scientific and Industrial Research Organisation, Melbourne, Australia. Airborne LiDAR data was collected by McElhanney Consulting Services Ltd., Vancouver, Canada. Biometeorology data and eddy-covariance estimates of primary productivity were collected and prepared by members of Dr. Andrew Black's team in the Faculty of Land and Food Systems, The University of British Columbia, Vancouver. I performed the interpretation and analysis of the data presented in this thesis, prepared the final manuscripts, and developed the methods for constructing the geometrically explicit models, detailed in Chapter 2 and 3, as well as methods for the simulation of light transport that are detailed in Chapter 4 and the Appendix. Co-authors provided advice on methodology and made editorial comments as required. Publications arising from the thesis thus far include:

- Van Leeuwen, M., Coops, N.C., Wulder, M.A. (2010). Canopy surface reconstruction from a LiDAR point cloud using Hough transform. *Remote Sensing Letters, 1*, 125-132.

- Van Leeuwen, M., Coops, N.C., Hilker, T.H., Wulder, M.A., Newnham, G.J., Culvenor, D.S. (2013). Automated reconstruction of tree and canopy structure for modeling the internal radiation regime. *Remote Sensing of Environment, 136*, 286-300.

Chapter 4 is currently in review by a leading scientific journal.

In addition to the work presented in this thesis, a concept for a wireless narrow-waveband sensor network for the measurement of the photochemical reflectance index was developed and field tested and the technical design and data observations are currently prepared for submission as a manuscript to a scientific journal. Finally, as research assistant, I conducted a literature review about the potential of airborne LiDAR data for estimating wood fibre quality attributes of standing trees, that has been published as:

- Van Leeuwen, M., Hilker, T., Coops, N.C., Frazer, G.W., Wulder, M.A., Newnham, G.J., Culvenor, D.S. (2011). Assessment of standing wood fiber quality using ground and airborne laser scanning: A review. *Forest Ecology and Management*, *261*, 1467-1478.

Table of Contents

List of Tables

List of Figures

List of Symbols

α	quantum yield of photosynthesis (µmol µmol^{-1})
α_c	cone angle (°)
α_{span}	angular width of objects in the panoramically projected EVI data (°)
$\alpha_l - \alpha_u$	parameter boundaries for cone opening angle (°)
β_{RH}	sensitivity of photosynthetic capacity to changes in relative humidity (%)
β_S	sensitivity of photosynthetic capacity to changes in mean daily temperature (°C)
β_T	sensitivity of photosynthetic capacity to changes in temperature (°C)
γ_{RH}	lag in response of photosynthetic capacity to changes in relative humidity (unitless)
γ_S	lag in response of photosynthetic capacity to changes in mean daily temperature (unitless)
γ_T	lag in response of photosynthetic capacity to changes in temperature (unitless)
Δz_l - Δz_u	parameter boundaries for z-displacement relative to local maximum (m)
$\delta_{i,j}$	range tolerance between neighbouring pixels i and j applicable to hard-targets (m)
Θ	vector of model parameters
ξ	change in angle along the medial axis measured within image coordinates (°)
χ	duration of initial linear response for three-parameter non-rectangular hyperbole
ρ	reflectance (unitless)
σ_K	standard deviation of Gaussian smoothing kernel (m)
τ	transmittance (unitless)
Ω	clumping index (unitless)

A_p	size of facet p (m^2)
B_i	radiosity of surface element i (µmol photons m^{-2} s^{-1})
D	stem diameter (m)
d	cumulative Manhattan distance (°)
E	irradiance (emission in radiosity model) (µmol m^{-2} s^{-1})
F_{dist}, $F_{dist,ind}$	distance transformation (°), indices of nearest feature pixels
F_{ij}	view factor expressing the fraction of radiation that leaves scene element i and reaches j
G	grid cell size of surface model (m)
$g(\theta_i)$	directional gap fraction of a branch (unitless)
h_{CHM}	height of local maximum in canopy height model (m)
h_{PHM}	height of local maximum in parametric height model (m)
h_{raw}	height of local maximum in raw point cloud data (m)
K	size of Gaussian smoothing kernel (m)
k	number of medial axis pixels
L	radiance (µmol m^{-2} s^{-1} sr^{-1})
L_s	length of occlusion measured along the stem (m)
L_z, $L_{\mathrm{z,max}}$	z-component of L_s, user defined maximum for L_z (m)
m	PHM threshold distance for voting 'True' (m)
n_{MR}	the minimum number of pixels contained in a medial axis (count)
P	photosynthetic assimilation (µmol m^{-2} s^{-1})

P_{gap}	gap probability (unitless)
P_{hit}	hit probability (unitless)
P_{max}	photosynthetic capacity (µmol m^{-2} s^{-1})
P_{opt}	optimal photosynthetic capacity, used in conjunction with down-regulating modifier functions to establish P_{max} (µmol m^{-2} s^{-1})
p	image element (i.e. pixel) or three-dimensional scene element (i.e. facet)
p_{left}, p_{right}	boundary pixels left and right of the medial axis
p_{MAT}	medial axis pixel (medial atom)
Q	fraction of diffuse to total photochemically active radiation (unitless)
R	range (m)
r	normalized cross-correlation coefficient (filtering criterion for stem detection)
RH	relative humidity (%)
RH_{mod}	relative humidity modifier (unitless)
s, s_{max}	angle between paired tangent vectors, user defined maximum for s (°)
T	temperature (°C)
t	time
T_{daily}	mean daily temperature (°C)
T_{mod}	temperature modifier (unitless)
T_{opt}	temperature at which photosynthetic assimilation is optimal (°C)
w	connecting segment, used in bridging occlusion along stems

List of Acronyms

APAR	absorbed photosynthetically active radiation
BR	boundary representation
BRDF	bidirectional reflectance distribution function
BTDF	bidirectional transmittance distribution function
CHM	canopy height model
CT	computed tomography
DBH	diameter at breast height
DEM	digital elevation model
DT	distance transformation
EC	eddy covariance
EVI	Echidna™ validation instrument
fAPAR	fraction of absorbed to incident photosynthetic active radiation
GEP	gross ecosystem productivity
GPP	gross primary productivity
IPAR	incident photosynthetically active radiation
LAI	leaf area index
LiDAR	light detection and ranging
MAT	medial axis transformation
MR	medial representation

*n*D	dimensionality (e.g. 1D, 2D, 3D)
NPQ	non-photochemical quenching
PAR	photosynthetically active radiation
PHM	parametric height model
PRI	photochemical reflectance index
RMSE	root mean squared error
RTM	radiative transfer model
RuBP	ribulose-1,5-bisphosphate
se	standard error
SLAM	simultaneous localization and mapping
TOC	top of canopy
UTM	universal transverse Mercator

Acknowledgements

Parts of this research were funded by an NSERC Discovery grant to Dr. Coops, as well as a Graduate Fellowship of The University of British Columbia, Vancouver, to Van Leeuwen. Other funds were made available through Research Assistantship in the Lodgepole Pine Partnership Project funded by the Canadian Forest Service and the Canadian Wood Fibre Centre.

I would like to thank my advisor Dr. Nicholas Coops for the opportunity to conduct my research here at UBC between the beautiful surroundings and amenities that Vancouver and the Coastal Mountains offer, as well as for sharing influential ideas and approaches that shape the field of remote sensing of the vegetated environment and not the least for the motivation to conduct this research and for funding. I would also like to thank my advising committee members Dr. Robert Guy, Dr. Andrew Black, Dr. Thomas Hilker and Dr. Michael Wulder for sharing their expertise and guidance throughout the research, and for questioning some of the research goals and formulations that have shaped this thesis. I am also grateful to members of the Integrated Remote Sensing Studio (UBC), the Commonwealth Scientific and Industrial Research Organisation, and the Biometeorology and Soil Physics Group (UBC) for their assistance and expertise during field work, and to my family and friends for their mental support and motivation, and last but not least to Jeanne for her support and understanding in busy times and sharing with me a sense of victory and company along a winding academic path of *search* and sometimes little *bargaining*.

1. Introduction

Information about forest productivity is useful to optimize yield, and map the distribution and quality of timber resources (Van Leeuwen et al. 2011a). Forest productivity is also an important indicator of biodiversity (Coops et al. 2008), and is significant for the valuation of ecosystem services (De Groot et al. 2012; Gamfeldt et al. 2012, 2013) such as carbon sequestration (Gibbs et al. 2007), and the provision of clean air, water and food (De Groot et al. 2000).

Remote sensing provides proven techniques for estimating forest productivity over large scales (Hall et al. 2012) in a consistent and reproducible manner (Herold & Johns 2007) by measuring the state and change of emitted and reflected electromagnetic radiation from the Earth surface using airborne and spaceborne instrumentation, typically in the visible, near infrared and thermal domains (i.e. 400 to 100,000 nm). Remote sensing is a useful tool for monitoring forested environments based on the ability to observe land-use change and disturbance (Hilker et al. 2009), but also changes in nutrient status, pigment concentrations and structural attributes of the canopy from features in the reflectance signal. Such features may be extracted by, for example, computing vegetation indices from specific spectral bands (Gitelson et al. 2006; Tucker & Sellers 1986), by considering a full spectrum of bands for analysis using wavelet decomposition and neural networks (Blackburn & Ferwerda 2008; Blackburn 2007; Weiss et al. 2001), through spectral mixture analysis (Ustin et al. 2004) or by using canopy radiative transfer modeling (RTM) that aims to describe the relation between biophysics, the sun-sensor-target geometry, and reflectance observed at the sensor (Jacquemoud et al. 2009; Schaepman et al. 2009; Verhoef 1984). While most methods in remote sensing rely on empirical calibration, RTM is the only physically-based method and permits direct coupling with physiological models (Choudhury 2001; Van der Tol et al. 2009; Wang & Jarvis 1990a).

Radiative transfer models describe the radiation field in a canopy as a balance between incoming and outgoing radiation resulting from absorption, emission and scattering (Gerstl & Borel 1992; Liang 2004). Radiative transfer can be computed for the one-dimensional (homogeneous) and three-dimensional (heterogeneous) case. One-dimensional models may consider turbid media of isotropic scattering particles of infinitesimal size or may consider anisotropic scattering due to specular reflectance or the casting of shadows from stacked layers of reflective bodies (Liang 2004; Roujean et al. 1992). Three-dimensional cases of radiative transfer consider lateral transport of radiation in addition to

vertical transport. Lateral transport is due to the heterogeneity of the scene and modeling requires geometrically explicit descriptions of the scene, often simply as geometric solids. Estimates derived from RTMs are averaged over these turbid media or geometric solids and significant deviations from these averages may arise due to the discrete nature of forest canopies (Gerstl & Borel 1992). To avoid scaling issues, the parameterization and validation of an RTM requires data that are collected at scales that are similar to the scales of turbid media or geometric solids. However, the availability of data is a key limiting factor and scales that are more commonly used for acquiring physiological data range from the shoot to tree level (e.g. Black & Moran 2006; Ethier et al. 2006; Passioura 1979; Sharkey 1985).

To bridge the gap between remote sensing and physiological mensuration and forest inventories, novel models of canopy radiation are needed at finer scales. The eminent challenges to compute radiation transfer at such fine scales include 1) computational tractability, 2) design of methods that efficiently capture the fine canopy structure in virtual models, and 3) coupling physiological responses to the simulated radiation regime. Recent advances in computing power and remote sensing have significantly improved processing capabilities that support the widespread digitization and animation of 3D real-world information at increasingly fine resolutions (Beraldin et al. 2000; Koch 2010). Such advances invite research that explores whether geometrically explicit models of real-world canopy structure can be used for the simulation of canopy radiation. This requires knowledge about the state-of-the-art in 3D remote sensing, modeling and rendering techniques, as well as knowledge about key physiological functions and environmental drivers affecting photosynthesis. The remaining parts of this chapter therefore provide a literature review on photosynthesis at the cell, leaf and canopy levels, and provide a synthesis of studies and techniques used to model canopy structure at scales ranging from the shoot to canopy level.

1.1. Scales of photosynthesis

An understanding of photosynthetic assimilation in trees involves knowledge about physiological functioning at the cell, leaf and canopy level. This knowledge is gained through a combined use of theory, measurement and simulation.

1.1.1. Cell level photosynthesis

Photosynthesis is the process of converting solar radiation in the range 400-700 nm into chemical energy in sugars for growth and maintenance respiration. Cell-level photosynthesis focusses on the light-dependent and light-independent reactions inside chloroplasts and the processes involved have been documented in many text books (Raven et al. 2005; Sharkey 1985), in summary: chlorophylls are the major pigments responsible for absorption of light for photosynthesis and reside in the thylakoid membrane inside the chloroplasts. Chlorophyll is distributed over two photosystems and light captured through the respective photosystems I and II excites electrons that are carried onto the electron transport chain to form nicotinamide adenine dinucleotide phosphate (NADPH). Electrons needed to replace those carried onto the electron transport chain are extracted from water through photolysis. This reaction establishes a proton gradient across the thylakoid membrane that is used to create adenosine triphosphate (ATP). The metabolites, NADPH and ATP are then used to sequester CO_2 and create glucose in the light-independent reactions through the Calvin cycle and this takes place outside the thylakoids. This cyclic reaction revolves around the enzyme Rubisco and the substrate Ribulose-1,5-bisphosphate (RuBP). Using the gained metabolites and CO_2 from the atmosphere, RuBP is continuously regenerated as sugars are formed.

Limitation in either RuBP regeneration or electron transport rate arise from limitations in environmental drivers such as the ambient CO_2 concentration, temperature, soil nutrient status and water availability (Monteith 1972, 1977). When photosynthesis is limited and cells are exposed to increasing or prolonged high light levels, a build-up of active oxygen and protons occurs and damage may arise (Demmig-Adams & Adams 2006). To avoid damage of the photosystems at high light levels regulating processes are in place that act at the cell level as well as at the tissue and the canopy levels. The predominant mechanism acting at the cell level is the xanthophyll cycle (Ahn et al. 2008), a group of carotenoid pigments residing in the thylakoid membrane, which involves a series of epoxidation and de-

epoxidation reactions establishing the conversion of violaxanthin to antheraxanthin and zeaxanthin. As the pool sizes of these pigments change, and zeaxanthin becomes more abundant, excess amounts of incident light are dissipated safely as heat (Demmig-Adams & Adams 2006). The mechanisms underlying the non-photochemical dissipation are still poorly understood (Farquhar et al. 2001; Holt et al. 2004; Ahn et al. 2008).

1.1.2. Leaf level photosynthesis

At the leaf level, cells are arranged into layers. The epidermis cells constitute the surface layers, while chloroplasts reside in cells of the mesophyll tissue (Sharkey 1985). Key photosynthetic regulators at the leaf level are the stomata that regulate transpiration and the exchange of CO_2 and O_2 with the atmosphere and prevent leaves from wilting. Closing of the stomata affects the partial pressure of CO_2 inside the leaf, and may induce photorespiration: a process initiated when a molecule of O_2 is taken up in the Calvin cycle instead of a molecule of CO_2 which results in a lowering of the assimilation rate. The mechanism of stomatal closure is governed by guard cells that regulate their internal cell pressure (turgor) through osmosis. Regulation of photosynthetic rate and light use efficiency may also be adjusted through chloroplast movement (Wada et al. 2003) and diurnal leaf movement in certain plants (Kao & Forseth 1991; Liu et al. 2007). These movements may either increase the amount of light incident on the leaf by moving the leaf so that it is perpendicular to the sun (diaheliotrophism) or decrease the incident light by turning the leaf away from the solar beam (paraheliotropism).

Figure 1.1 shows the dependency of photosynthesis on light. The curve shows an asymptotic increase that indicates a diminishing efficiency in fixing CO_2 at higher light levels. Semi-empirical approaches have modeled this relationship using hyperbolic functions constrained by two or three parameters (Cannell & Thornley 1998; Middleton et al. 2009). A mechanistic model at the cell level was proposed by (Farquhar et al. 1980) that describes photosynthesis as a limitation of either RuBP regeneration or Rubisco, so that the overall assimilation of photosynthate is the minimum of these two potentials. Dependencies of both RuBP regeneration and electron transport rate on temperature are treated in the model as well as CO_2 and O_2 concentrations. The model has found wide use in plant research and has been used to examine the effects of temperature changes (Medlyn et al. 2002) and elevated CO_2 concentrations on productivity (McMurtrie & Wang 1993). The Farquhar model describes

photosynthetic response under steady-state conditions when the photosynthetic rate is at equilibrium with incident radiation.

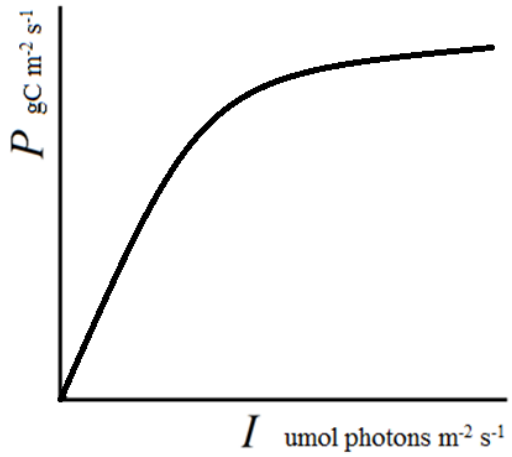

Figure 1.1: General shape of the photosynthetic light-response curve. Shown on the y-axis is the photosynthetic assimilation (i.e. gross or net uptake of CO_2) and on the x-axis is incident radiation.

Methods of measuring plant productivity at the level of individual leaves include gas exchange, chlorophyll fluorescence, and spectroscopy. Gas exchange measurements are made using either steady-state or non-steady-state approaches. The former typically requires a constant flow of air through a chamber in which the leaf or shoot is secured and illuminated with a constant radiation source. Exchange of CO_2 and H_2O are then calculated as the product of the flow rate and the difference between the CO_2 concentration of the air entering and leaving the chamber (Ethier & Livingston 2004; Sharkey 1985). In the non-steady-state approach the rate of change in CO_2 concentration in the chamber enclosing the leaf is used to calculate CO_2 or O_2 exchange (Field et al. 1989). Fluorescence is the phenomenon in which photons are emitted after electrons relax to their ground state, after they are excited to a higher energy level by light. When the reaction centres transfer energy onto the electron carriers, the oxidation state of the reaction centre needs to be reduced and the reaction centre is 'closed' and unavailable for electron transport. As a result, absorbed light energy can either be dissipated as heat (known as non-photochemical quenching, NPQ) or emitted as fluorescence. Since these two mechanisms have separate reaction times to changes in irradiance, portions of emitted and

dissipated radiation can quite easily be determined. Moreover, maximum photosynthetic potential (i.e. when all reaction centres are open) can easily be measured when the leaf is acclimated to dark conditions and all reaction centres are open, by emitting a pulse of light onto the leaf and measuring fluorescence. The energy released through fluorescence peaks around 680 nm and amounts to approximately 1 or 2% of the total absorbed light (Maxwell & Johnson 2000). In field conditions, this can be measured with relative simplicity using a modulated light source (Porcar-Castell et al. 2008). Finally, an important contribution to the observation of photosynthetic down-regulation was made by Gamon et al. (1992) who demonstrated the use of the photochemical reflectance index (PRI) that isolates absorption features of anteraxanthin and zeaxanthin from other leaf pigments and that is indicative of changes in the state of the xanthophyll cycle, and relates to NPQ. This index is derived using spectrometers (Gamon et al. 1992) or narrow-waveband sensors (Filella et al. 1996) and is computed as the normalized difference between leaf reflectance (ρ) at 531 and 570 nm, as:
$(\rho_{531} - \rho_{570})/(\rho_{531} + \rho_{570})$.

1.1.3. Canopy level photosynthesis

Canopy structure affects internal shading and exposure of leaves to downwelling hemispherical irradiance. The fractal, or self-similar geometry of canopy architecture, establishes a formation of foliage clumps and canopy gaps that improves the penetration of radiation towards deeper canopy strata (Oker-Blom 1986). In addition, the small size of needles and leaves in relation to the solid angle of the solar disc leads to the formation of penumbra or half-shadows that further improve the penetration and spread of incident light (Stenberg 1995a). Over large spatial scales, the attenuation of visible or photosynthetically active light (400-700 nm) follows an exponential decay with canopy depth. This rate of decay increases with leaf area and decreases with clumping and is different for direct and diffuse illumination (Black et al. 1991; Chen & Black 1992; Nilson 1971); However, using data representing much finer spatial scales such as acquired from vertical tram lines or balloons, a profound deviation from this exponential relation or even abrupt changes (lumiclines) in canopy radiation can be observed (Parker et al. 2001).

The complex relationship between leaf incident radiation and canopy structure has important implications for photosynthesis. For example, the movement of the sun in combination with wind creates a constant movement of sunflecks and under such transient changes in leaf-level light intensity,

assimilation rates deviate from steady-state conditions (Pearcy 1990). At the time scale of weeks, the predominant canopy radiation conditions change due to trends in meteorology, and nitrogen may be reallocated to accommodate higher photosynthetic capacities of highly exposed leaves (De Pury & Farquhar 1997). Such reallocations of minerals and changes in photosynthetic capacities have also been observed with the aging of the canopy, and older leaves and tree crowns have been associated with lower photosynthetic capacities resulting from lower mesophyll- and stomatal conductance (Ethier et al. 2006) and hydraulic conductance (Gamon and Bond 2013). Important impacts on productivity at the canopy scale also arise from competition between trees and species and leads to a rather different physiological behaviour at the canopy level than what is observed under conditions when a plant is isolated and not in competition (Poorter et al. 2013).

A wide range of canopy-level productivity models exists (see Table 1.1 for a selection of models). It is evident that for modeling forest productivity at operational scales, only some of the most significant physiological controls on photosynthesis can be considered (Landsberg 2003). At the broadest scales, models typically do not consider canopy structure and assume the forest to behave as if it were a single big leaf (Monteith 1972, 1977) or consider a different extinction coefficient for diffuse radiation (Cai et al. 2009). So-called two-leaf models consider sun and shade acclimated leaves (De Pury & Farquhar 1997). The latter approach is preferable since it considers the higher photosynthetic capacity of sun acclimated leaves compared to shade acclimated leaves. Both approaches do not consider vertical profiles in environmental parameters, however, so that they inevitably fail to address an important function of the canopy, namely that of creating homeostasis of environmental conditions that is known to have a profound effect on photosynthesis (Jarvis 1976). Instead, the models use *effective* parameters that relate to the entire canopy and, as a result, model estimates can only be derived at an aggregate level (i.e. the canopy). This leads to two key problems. The first problem arises when these models are used in conjunction with data sources that represent scales that are different from the models. For example, passive optical remote sensing methods are used to monitor forest productivity globally; however, these data are limited to observations of top-of-the-canopy reflectance and are unable to discriminate physiological dynamics in the reflectance signal that occur deeper in the canopy. Combining observations and models thus leads to the problem of parameterizing the entire canopy productivity using data from only the top of the canopy. The second limitation relates to availability of ground-truth data. Currently, two common methods of validation at the canopy scale exist. These are destructive sampling and the eddy-covariance technique. The latter technique estimates productivity from fluxes of CO_2 and O_2 that are inferred from high-frequency measurements of wind vector components and gas

mixing ratios (Baldocchi et al. 2001). Both techniques, however, are costly and the eddy-covariance technique is limited to homogeneous and relatively flat terrain, so that data availability for model validation is greatly limited.

Researchers have developed process-based models that operate at the scale of individual trees that are reconstructed using geometrical primitives such as spheroids and cones (McMurtrie et al. 1990; Wang & Jarvis 1990a) or layered canopy models (Norman 1979). Such models provide for integration of *in situ* sensors for validation and parameterization; however, these models are limited to explaining forest productivity for homogeneous and simple heterogeneous scenes only and fine canopy structural details cause some significant differences between *in situ* sensor readings and model estimates (Wang & Jarvis 1990b). A preferable, but hard-to-reach solution would be to model canopy structure at an arbitrary fine resolution, e.g. shoot level (Disney et al. 2000). Recent contributions from remote sensing and computer graphics make the capture of 3D real-world data and the modeling of realistic tree architectures increasingly possible, and create opportunities for further investigating the potential of this fine-scale modeling approach (Disney et al. 2000; Godin et al. 1999). At increasingly fine resolutions, such models become virtual plant environments that help to close the gap between remote sensing observations and shoot or tree-level measurements (Disney et al. 2000; Godin et al. 1999; Pradal et al. 2009; Prusinkiewicz & Lindenmayer 2004) and provide a means to control for environmental variables through simulation that otherwise cannot be controlled for in open-air field experiments. These fine scale models do not only provide improvements for fusing shoot-level and canopy-level data, but can also be used to calibrate and validate the layered process-based models, for example, by enabling computer simulations to estimate extinction coefficients and averaged vertical variation in the canopy light regime.

Table 1.1: Selected canopy radiation models and productivity models covering a wide range of scales, and physiological functions. (D = dimensionality; LC = light competition; PC = pigment concentration; SC = stomatal conductance; XC = xanthophyll cycle; LAC = light acclimation; TP = branching topology)

reference	name	structural representation	Scope	D	LC	PC	SC	XC	LAC	TP
Wang and Jarvis (1990a)	MAESTRO	tree	productivity	3D	✓		✓			
McMurtrie et al. (1990)	BIOMASS	tree, layered	productivity	3D	✓		✓			
Norman (1979)	CUPID	layered	productivity	1D			✓			
Verhoef and Bach (1984)	SAIL	layered	scattering	1D		✓				
Strahler and Jupp (1991)	GORT	tree	scattering	3D	✓					
Godin et al. (1999)	AMAPmod	branch	productivity	3D	✓					✓
Barton & North (2001)	FLIGHT	leaves	LUE	1D				✓		
De Pury & Farquhar (1997)		two-leaf model	productivity	1D	✓				✓	
Monteith (1972)		big-leaf model	productivity	1D						

1.2. Measuring forest structure

Early methods used for capturing detailed and accurate information about canopy structure have been laborious and are often destructive (Norman and Campbell 1989). Some methods are based on allometric relationships between the distribution of foliage area or mass and more easily measurable attributes such as branch diameters to generate statistical models of foliage distribution at the tree or plot level (Seidel et al. 2011). Representations of tree structure that include both geometrically explicit as well as topological information have also been obtained. Information about branch topology has been found useful to identify branches through time, e.g. for growth modeling (Godin et al. 1999). Such fine geometric measurements have been derived with the use of an electromagnetic digitizer (Polhemus 1993) that includes a hand-held pointer that is used to measure the 3D position of branching nodes and foliage within a local coordinate frame. A tree is digitized by sampling its branching nodes in topological order (Godin et al. 1999) and by manually processing each measurement. Due to this laborious process, a full digitization of a single small tree (e.g. 600 leaves) may require several days of field labour (Godin et al. 1999; Sinoquet et al. 1998). Some suggestions for automation have been made, including voice recognition so that an operator could work alone by dictating the observed topology and related measurements into a microphone (Room et al. 1994, in Godin et al. 1999).

It was not until the invention of laser scanning that the direct retrieval of 3D information has gained real potential. Using this technology, a beam of laser light is used to measure distance as the time that a pulse of light takes to travel from the scanner to the target and back to the scanner. Laser scanning devices can be operated from ground-based or airborne platforms. For airborne scanners, 3D point cloud information is obtained by integrating laser scanners with global positioning systems (GPS) and inertial measuring units that measure attitude and position of the scanning instrument (Wehr & Lohr 1999). The resulting data represents the 3D coordinates of reflecting targets and is often stored as point cloud data. Alternatively, the reflected beam may be digitized at a nanosecond bandwidth providing for the full recording of returned energy against time, in which case the data is referred to as full-waveform data (Strahler et al. 2008). Airborne LiDAR provides a cost-effective means to map topological information and forest structure across the landscape. Static, ground-based laser scanners are simpler in design and allow for an unprecedented level of detail in acquiring forest structural attributes. Figure 1.2 shows two merged data sets and demonstrates the co-location of forest structural features in airborne LiDAR and ground-based laser scanning data. The clear differences in data representation result from the distinct viewing perspectives of the scanning instruments and indicate the complementarity of the information contents of the two technologies. While airborne LiDAR has a downward looking perspective, ground-based instruments have a hemispherical upward perspective.

A comprehensive review of methods used for the processing of LiDAR and laser scanning data is not provided in this thesis, but can be found in literature (e.g. van Leeuwen & Nieuwenhuis 2010). In general, methods for processing airborne LiDAR data advanced more quickly than techniques for ground-based laser scanning. Early applications for ground-based laser scanning in forestry focused on simple metrics such as diameter at breast height (DBH) and tree height (Aschoff & Spiecker 2004; Bienert et al. 2007; Liang et al. 2012; Maas et al. 2008; Pfeifer & Winterhalder 2004; Pueschel et al. 2013; Van Leeuwen et al. 2011b), while more recent studies include estimates of leaf area (Jupp et al. 2008), woody-to-total plant area (Clawges et al. 2007), leaf angle distributions and chlorophyll concentrations (Eitel et al. 2010), and crown shape (Moorthy et al. 2011). The utilization of the full breadth of information contained in ground based laser scanning data remains challenging to date, however. Airborne approaches are typically based on empirical relations between forest inventory attributes and statistics derived from point cloud data (Wulder et al. 2012) such as percentile distributions of return heights, or the coefficient of variation to infer e.g. plot-level biomass (Breidenbach et al. 2010; Drake et al. 2002; Næsset & Gobakken 2008), or tree height (Andersen et al. 2005; Coops et al. 2007; Næsset et al. 2005). Airborne data can also be used to delineate individual tree

crowns and estimate individual tree and crown attributes (Heurich 2008; Popescu et al. 2003; Van Leeuwen et al. 2010). Ground-based scanning seeks to automate feature extraction and segmentation approaches and often involves algorithms of graph theory (Côté et al. 2009; Livny et al. 2010) and image processing (Pueschel 2013; Pueschel et al. 2013; Van Leeuwen et al. 2013; Van Leeuwen et al. 2011b).

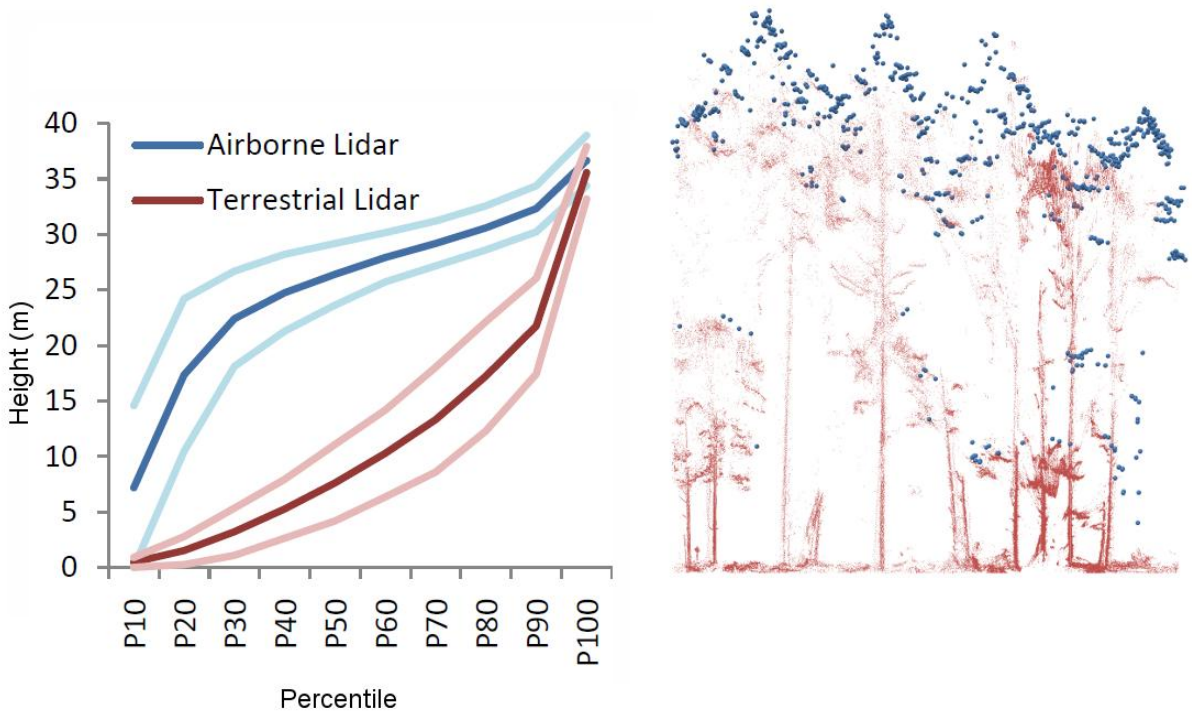

Figure 1.2: Shown are the individual returns of co-registered airborne LiDAR and ground-based laser scanning data of the study area (see Chapter 1.5). On the left side are shown the differences in the shapes of percentile distributions that were obtained from these data.

Some approaches convert the recorded laser returns to voxel spaces (Seidel et al. 2012; Yang et al. 2013) that are discretized and rasterized representations of a 3D continuous space; however, unlike computed tomography (CT), for example, that uses X-rays to obtain data related to the internals of a body and voxel spaces to store these data, laser scanning only sees the surface of objects and is affected by data occlusion effects. These effects may result in cavities or holes along the object surfaces that would alter their appearance and reflective (transmissive) properties. To avoid such effects, multi-

scanning approaches have been proposed; However, the rigorous assessment of data coverage from multi-scanner-installation set-ups has yet to be incorporated (Yang et al. 2013). A number of studies have demonstrated the derivation of 3D vector models from point cloud data of individual trees or forest inventory plots and have focused on the credible reconstruction of unseen parts of the canopy (Raumonen et al. 2013). Modeling approaches have primarily focused on using point cloud information and generally require various assumptions on growth patterns and foliage characteristics. These methods typically start with the segmentation of returns into woody material and foliage, e.g. based on return intensities (Côté et al. 2009) or spectral information (Douglas et al. 2012; Gaulton et al. 2013) after which geometries of tree trunks and branching can be obtained. To address effects of data obscuration and roughness of object surfaces, least squares optimization (Maas et al. 2008) and hypothesis testing and generating techniques such as Hough transform (Fleck et al. 2004) have been adopted. Coarse topological graphs of branching structures may be created using skeletonization algorithms (Bucksch et al. 2010; Verroust & Lazarus 2000). More recent developments in modeling tree structure have combined laser scanner data with tree architectural software (Côté et al. 2011; Mech & Prusinkiewicz 1996; Runions 2007; Weber & Penn 1995) to represent levels of detail beyond the shoot. This is achieved by simulating the growth of fine woody structures that follow the spatial distribution of foliage returns or that adapt to simulations of the internal canopy radiation regime (Côté et al. 2011, 2009; Runions et al. 2007) or by fitting template tree crowns to growing-spaces that are derived from stem and crown information (Van Leeuwen et al. 2013). Reconstruction of tree structure has also been attained using cheaper digital cameras combined with advanced photogrammetric processing techniques to obtain 3D information and realistic tree representations (Neubert 2007; Tan et al. 2006).

1.3. Modeling canopy radiation and photosynthesis

The attenuation of light in turbid media, such as a pigment solution, follows an exponential decrease and is described by Beer's law. In forestry, a modification of Beer's law has been used that is based on leaf area index (LAI), a solar angle dependent extinction coefficient $G(\theta_{sun})$ and the clumping factor Ω (Chen 1996; Nilson 1971) to correct for the organization of foliage into shoots, around branches and into crowns. This clumping factor has a value of 1 under random placement of foliage material and decreases with clumping so that the probability of radiation penetration to deeper canopy layers increases. The application of Beer's law can be used to estimate the fraction of absorbed photosynthetic active

radiation (fAPAR) that is used in a variety of models to compute canopy photosynthesis (Hall et al. 2012; Hilker et al. 2012a; Monteith 1972, 1977) for example as gross primary productivity (GPP), or as net primary productivity (NPP) that takes respiration into account. More complex radiation transfer models may consider stand heterogeneity or the stratification of foliage material with canopy depth. In the case of increasingly fine structural models, simulations of the radiation regime are based on iterative computations of lines of sight between canopy elements and between canopy elements and radiation sources. Although a wide variety of model implementations exist, two methods, ray tracing and radiosity, hold promise. Ray tracing provides for the derivation of a large variety of measures related to the canopy radiation regime at a very high accuracy (Widlowski et al. 2007). However, as the processing involves numerous computations of intersections of rays with the scene (Govaerts & Verstraete 1998; Suffern 2007), ray tracing is also the most computationally intensive technique available to compute such information and applications in remote sensing have often been limited to providing validation data sets (Côté et al. 2012; Disney et al. 2000; Widlowski et al. 2007). Moreover, due to their stochastic nature, ray-tracing simulations are not suited for dynamic lighting conditions. Radiosity models, on the other hand, compute view factors that represent the visibility from one scene element to another, and from scene elements to light sources. These view factors facilitate that surface absorptance and reflectance for all scene elements can be computed rapidly for any distribution of emittance across the light sources (Cohen & Wallace 1993); see Figure 1.3 for a pictorial demonstration of the differences between radiosity and ray tracing. The computation of view factors is challenging (Liang 2004), however, and approximate methods have been proposed instead. These approximate methods typically assume that radiation leaving a single differential area (i.e. point) on one surface element that reaches another surface element is representative of all differential areas (i.e. points) on that surface element. Examples of methods include the Nusselt analog or hemicube approximation for which the interested reader is referred to Cohen and Wallace (1993). Demonstrations of the potential of radiosity models in remote sensing have been made by, for example, Gerstl and Borel (1992) and more recently by Huang et al. (2013).

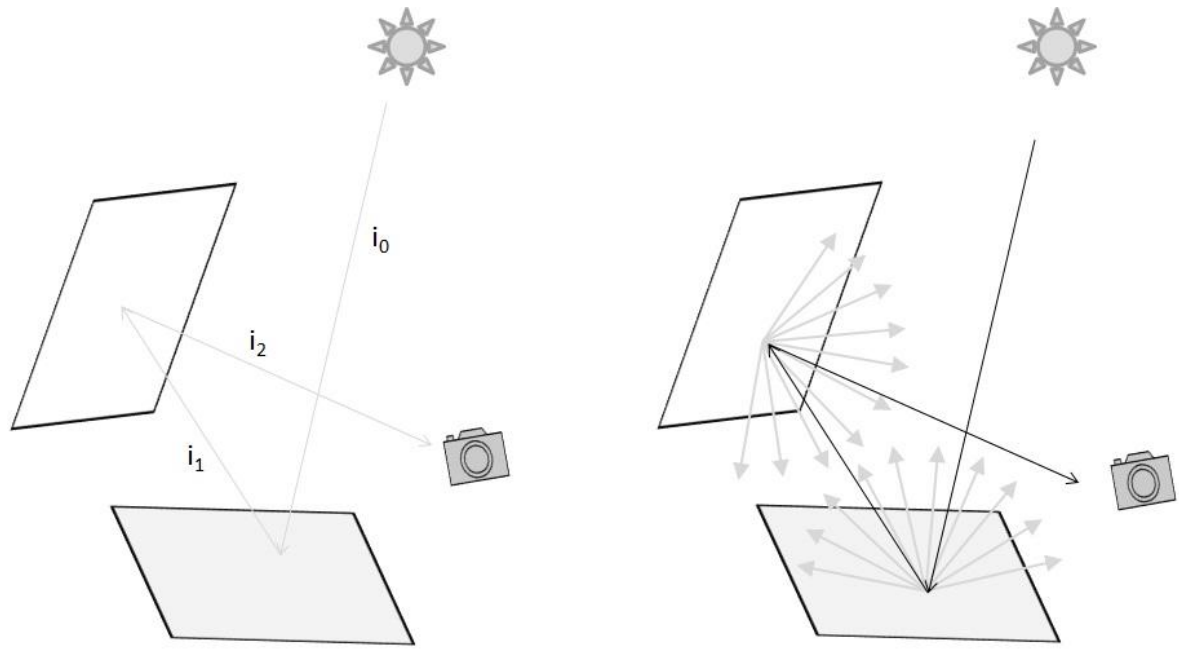

Figure 1.3: A pictorial demonstration of forward ray tracing (left) and radiosity (right). In forward ray tracing, individual photons or rays are followed until intersection with one of the scene elements and its fate (i.e. absorption or scattering) is determined stochastically. If the fate is to scatter, a new direction is computed and a new intersection is sought. This process continues until the photon is absorbed, reaches the camera or bounces outside the scene. If the light source or the camera is moved, the ray tracing simulation needs to start again. Radiosity modeling starts with the computation of view factors for all scene elements that store the degree of exposure of element j to radiation leaving element i, so that all radiation leaving i sums to unity. Once these view factors are computed, the solution to the radiosity model can be computed more quickly when the illumination conditions or camera perspective changes (see also SIGGRAPH's educational material for an overview of the radiosity algorithm: http://www.siggraph.org/education/materials/HyperGraph/radiosity/overview_1.htm, last accessed on December 31, 2013).

1.4. Research objective and research questions

The objective of this thesis is to develop automated methodology for modeling canopy structure at an arbitrarily fine resolution that provides for the estimation of shoot-level to canopy-level radiation and photosynthesis-related information. The research in this thesis focusses on the use of the high information content of ground-based laser-scanning data combined with tree-regeneration techniques to obtain realistic reconstruction of selected inventory plots. The explicit modeling of canopy elements within these inventory plots enables the simulation of incident canopy radiation at the leaf level. This is used to evaluate a leaf-level photosynthesis model that responds to temporal dynamics in the environmental variables: temperature, relative humidity and photosynthetic active radiation. Using a single-leaf photosynthesis model, GPP estimates are obtained through integration over individual canopy elements. The leaf-level photosynthesis parameters are optimized by minimizing differences between the simulated and eddy-covariance GPP estimates.

The research in this thesis is arranged to answer the following research questions and to explore opportunities to improve the integration of field mensuration data at the shoot and tree level with models of canopy radiation transfer.

1. Can LiDAR remote sensing parameterize 3D light transport models at scales ranging from shoot level to plot level?
2. Can leaf-level IPAR be simulated over a growing season at a sub-hourly time step from arbitrarily complex canopy light transport models?
3. Can leaf-level physiological parameters be inferred from simulated canopy radiation and stand-level productivity estimates?

1.5. Study area

The study area is located on Vancouver Island, BC, Canada, near the city of Campbell River, in the Oyster River area about 16 km from the east coast of the island (UTM Zone 10, NAD83: 331150E, 5529900N to 336150E, 5524900N). The area (Figure 1.4) is a plantation forest consisting of 80% Douglas-fir [*Pseudotsuga menziesii* spp. *menziesii* (Mirb.) Franco], 17% western redcedar [*Thuja plicata* Donn. ex D. Don], and 3% western hemlock [*Tsuga heterophylla* (Raf.) Sarg] (Coops et al. 2007; Krishnan et al. 2009; Morgenstern et al. 2004) with main understorey species, salal (*Gaultheria shallon* Pursh.), dull Oregon grape (*Mahonia nervosa* (Pursh.) Nutt.), vanilla-leaf deer foot (*Achlys triphylla* (Smith) DC), and various ferns and mosses. The site is located on a northeast facing 5-10° slope and the stand density is 1100 stems ha^{-1} with tree heights ranging between 30 and 35 m (Hilker et al. 2010a). The predominant age of the trees was 60 years old in 2009. The region belongs to the dry maritime Coastal Western Hemlock biogeoclimatic subzone (CWHxm) and has a mean annual precipitation and temperature of 1,500 mm and 9.1 °C, respectively (Meidinger & Pojar 1991). A total of four 30 x 30 m plots were established based on representativeness of the stand of which one (plot 7) was nitrogen enriched (Hilker et al. 2012b). Airborne LiDAR data and ground-based laser scanning data covering all four plots were acquired in 2008, whereas eddy-covariance and meteorological records used for computer simulation and validation were selected for the year 2009.

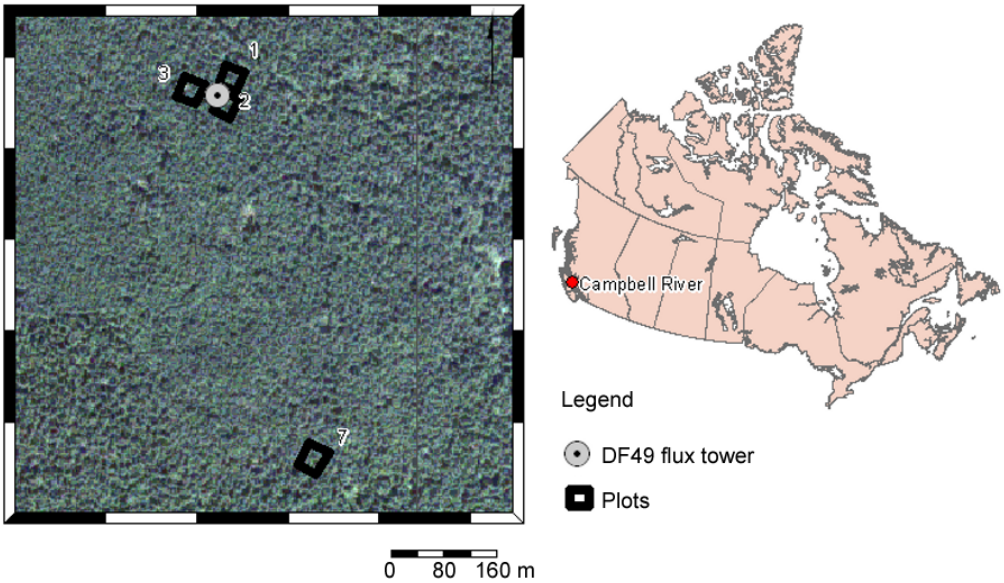

Figure 1.4: Study area showing the inventory plots and the eddy-covariance flux tower.

1.6. Outline

Chapters 2 and 3 describe methods for the reconstruction of forest plots from airborne LiDAR and ground-based laser scanner data respectively. In Chapter 2, airborne LiDAR data are used to characterize crown dimensions and to efficiently parameterize a coniferous forest canopy as a series of cones with varying radii and heights. The intersection of these cones provides for the delineation of individual crowns. In Chapter 3, a novel and computationally-efficient method for the detection of tree stems and stem attributes from ground-based laser scanning is presented. These derived stem and crown attributes are then used to parameterize three-dimensional forest plots of which the structural quality is assessed based on simulated and measured contact frequencies of light rays with the canopy.

Chapter 4 combines the virtual forest scenes reconstructed through the methodology explained in Chapters 2 and 3 with light transport modeling to simulate the propagation of photochemically active radiation throughout the canopy. Estimates of incident photochemically active radiation at the level of individual canopy elements are combined with environmental data about temperature and relative humidity to drive a leaf-level photosynthesis model that has 10 parameters. Canopy-level gross primary productivity is then estimated over the 2009 growing season by integrating leaf-level photosynthesis over the individual canopy elements. The results indicate the efficiency of the light transport model for complex scenes and the potential to estimate leaf-level photosynthesis parameters using a model inversion technique and eddy-covariance stand-level estimates of gross primary productivity.

Chapter 5 provides a discussion of the significance of the study and the potential for airborne LiDAR and ground-based laser scanning to create geometrically explicit forest structural models and integrate shoot-level physiological measurements with remote sensing data.

2. Canopy surface reconstruction from a LiDAR point cloud using the Hough transform

2.1. Introduction

The measurement and mapping of individual tree attributes, including tree height, crown shape and volume are of significant importance in forestry, where such information is used to predict, for example, growth, yield, and standing biomass (Lim et al. 2003). These measurements are typically stored as two-dimensional stem maps or as three-dimensional models that represent rough outlines of individual tree crowns (Kato et al. 2009). Such maps and models may be used to estimate stand density or to derive reflective and absorptive properties of a stand using geometric optical radiative transfer (Strahler & Jupp 1991) or simulation models (Wang & Jarvis 1990a) from which valuable information is derived for the estimation of gross and net primary productivity (Hilker et al. 2012a; Wang & Jarvis 1990a).

For large areas, airborne LiDAR remote sensing can be used to obtain measurements of individual tree attributes rapidly and cost-efficiently. Typically, canopy height models (CHMs) are derived from these LiDAR data and are used to detect and delineate individual tree crowns. These CHMs are created by interpolating first-return LiDAR data after normalizing the return heights to a digital terrain model (Ben-Arie et al. 2009). Individual tree locations are derived as the local maxima in CHMs and the crown delineations are derived using template matching (Popescu et al. 2003) or watershed algorithms (Chen et al. 2006). These delineations can then be used to subset the LiDAR data and to extract individual tree attributes.

However, a number of problems have been identified that limit CHMs to accurately retrieve individual tree and crown attributes (Ben-Arie et al. 2009; Brandtberg et al. 2003; Nelson et al. 2000). First, crown delineation from CHMs can result in inappropriate crown shapes, and crown boundaries can overlap with other trees or cover canopy gaps (Mei & Durrieu 2004; Rahman & Gorte 2009; Weinacker et al. 2004). Second, underestimation of tree height is commonly reported (Holmgren & Nilsson 2003; Næsset 1997; Nilsson 1996) and results from LiDAR acquisition whereby tree apexes may be missed (Morsdorf et al. 2004), and the permeability of tree crowns to laser light (Gaveau & Hill 2003). Third, CHMs typically contain surface irregularities that require correction (Ben-Arie et al. 2009) and smoothing techniques used to correct surface irregularities can have adverse impacts on individual tree detection,

crown delineation, and the retrieval of crown parameters (Leckie et al. 2003; Popescu & Wynne 2004). Fourth, as a result of rasterizing, tree top locations in the CHM may have moved from their location in the raw point cloud (Pitkanen et al. 2004).

Improvements in the delineation of tree crowns may be sought in the use of algorithms that are less sensitive to noise or irregularities in the CHM as well as algorithms that fit three-dimensional shapes to the LiDAR data as opposed to two-dimensional templates or watersheds. Once three-dimensional shapes are fitted, delineations between shapes are easily obtained by computing geometric intersections. Hypothesis testing and generating procedures such as the Hough transform (Hough 1962; Duda et al. 2001) have been frequently used for fitting template shapes to noisy images or three-dimensional data sets. In such procedures, image pixels or three-dimensional data points vote over a set of object parameterizations (i.e. shapes) from which the parameterization that fits best is determined based on consensus. The goal of this research is to develop a tree-level object-based canopy model, called the parametric height model (PHM) that is based on the Hough transform. The proposed algorithm describes the forest canopy as a series of cones fitted to the raw LiDAR point cloud, from which tree-crown delineations can be extracted through simple geometric operations. It is further anticipated that by fitting cones to the raw LiDAR point cloud, the negative height bias can be corrected.

2.2. Methodology

2.2.1. Study area

A full study area description is available in section 1.5.

2.2.2. Data processing

Ground versus non-ground hits in the LiDAR data were separated and a gridded digital terrain model was created. The non-ground point cloud was normalized to obtain LiDAR return heights relative to digital terrain model height, and from this normalized point cloud a CHM was created following Ferster et al. (2009), and using a grid cell size of 40 cm.

Local maxima were detected in the CHM using the level-set method (Ying et al. 2004). Using this method, a set of equally spaced height-thresholds is used and for each pixel in the CHM a Boolean is stored to indicate whether the pixel is above or below the threshold. This results in a stack of Boolean

images where true values are assigned to those pixels with heights greater than the threshold. These stacks of images enable one to follow the outline of an individual crown across a range of heights. The local maxima of individual tree crowns were then obtained as follows: if, for any layer *i* in the image stack, there is a contiguous set (a.k.a. 'blob') of 'true' pixels that overlaps with a contiguous set of 'true' pixels in the next layer (i.e. *i+1*) then the top of the crown is not yet found. However, if any contiguous set of pixels in layer *i* does not overlap with a set of layer *i*+1 then a local maximum is computed as the geometric centre of pixels contained in the contiguous set of 'true' pixels in layer *i*. The thus found local maxima relate to the CHM and local maxima in the raw LiDAR point cloud were subsequently found within vertically aligned cylinders centered at the CHM local maxima. Based on point spacing and the cell-size of the CHM, the cylinder radii were set to 50 cm.

At the position of the local maxima, cone shaped objects were fitted to the raw LiDAR data using an implementation of the Hough transform (Hough 1962). The Hough transform has been extensively used in image processing, for example, for the detection of lines and circles in photographs. For 2D imagery, the Hough transform is typically preceded by an edge-detection algorithm that identifies a potentially sparse set of pixels along object contours displayed in the image. A so-called parameter space is created to define the range of parameter values that constitute the set of potential object shapes and orientations. For every contour pixel, a set of potentially fitting shapes (e.g. circles, lines) is determined and its parameters denote the coordinates of a vote that is registered in a so-called accumulator space. As votes accrue, the accumulator space updates the number of votes per unique parameter combination. Consensus around the best fit is then obtained from the accumulator space as the combination of parameters with the most popular vote. The Hough transform has also been used for 3D applications, for example, for reconstruction modeling of buildings from LiDAR data (Vosselman & Dijkman 2001). In our implementation, cones were fitted to the raw LiDAR point cloud data using two free parameters to constrain the cone shape: apex angle (α_c) and cone height, and the locations of the cones in the x,y-plane was fixed to the local maxima of the CHM. The apex angle of a cone relates to coordinates of points along the cone surface as:

$$sin(\alpha_c) = \sqrt{\frac{b}{l}} \tag{2.1}$$

where

$$b = \begin{pmatrix} x - x_T \\ y - y_T \end{pmatrix}^2 \tag{2.2}$$

and

$$l = \begin{pmatrix} x - x_T \\ y - y_T \\ z - z_T \end{pmatrix}^2 \tag{2.3}$$

In equation 2.2 and 2.3, x_T, y_T, and z_T are the coordinates of the cone top (i.e. with x_T and y_T obtained from the local maxima in the raw LiDAR point cloud) and *x, y, z* are the coordinates of points along the cone surface. Apex angle, α_c, expressed as the angle between the cone axis and a line on the cone surface was limited to the range 10 – 24°. The cone height, z_T, had no absolute bounds but was restricted to a range of 0 to 2 m above the local maximum (CHM) of the tree crown that a particular cone instance was fitted to. LiDAR returns voting over a cone shape, where selected using a vertically aligned cylindrical subset of returns within 2.5 meter distance from the tree top (x_T, y_T)-locations. In order to assess the accuracy of the method, statistical analysis was conducted to assess the correlation between tree heights obtained from the raw point clouds (i.e. from the local maxima) and those heights obtained from the PHM and the CHM, and any bias introduced in creating the surface models.

Additionally, crown delineations were derived based on computed intersections between lines and triangles. For each cone, a set of lines was constructed from the cone apex to its base as well as a set of isosceles triangles that have one edge at the cone apex. Using the intersections between lines and triangles the crown delineations were established. Line-with-triangle intersections were computed,

rather than line-with-cone, or cone-with-cone intersections for the generality of the method and sole demonstration purpose of this study.

2.3. Results

Figure 2.1a and b show the original CHM and the created PHM, respectively. In Figures 2.1a and b, the CHM are offset vertically and displayed along a second height axis for comparison. The CHM shows clear smoothing of tree tops and ambiguous crown boundaries, whereas the PHM shows clear crown boundaries and distinct tops. Figure 2.2 demonstrates the delineation of individual tree crowns from the parametric height model.

Linear regression indicates that both the PHM and CHM were highly correlated with the heights of local maxima in the raw LiDAR point cloud ($r = 0.99$, and $r = 0.98$, respectively, Table 2.1). However, CHM heights are negatively biased with the raw local maxima, whereas PHM heights are positively biased. A dependent samples t-test reveals that these offsets are significantly greater than zero ($P < 0.01$). For the PHM, the offset is 1.3 m (se = 0.6 m), and for the CHM the offset is -1.2 m (se = 0.7 m) (Table 2.1). By describing the forest canopy height as a model that comprises a series of cones, a significant reduction of data size is achieved, in this case by a factor 80.

Table 2.1: Statistics obtained from linear regression and a dependent samples t-test.

Model	Equation	r	bias	se	N
PHM	$h_{PHM} = 0.87 + 1.01h_{raw}$	0.99	1.3	0.6	157
CHM	$h_{CHM} = -0.71 + 0.99h_{raw}$	0.98	-1.2	0.7	157

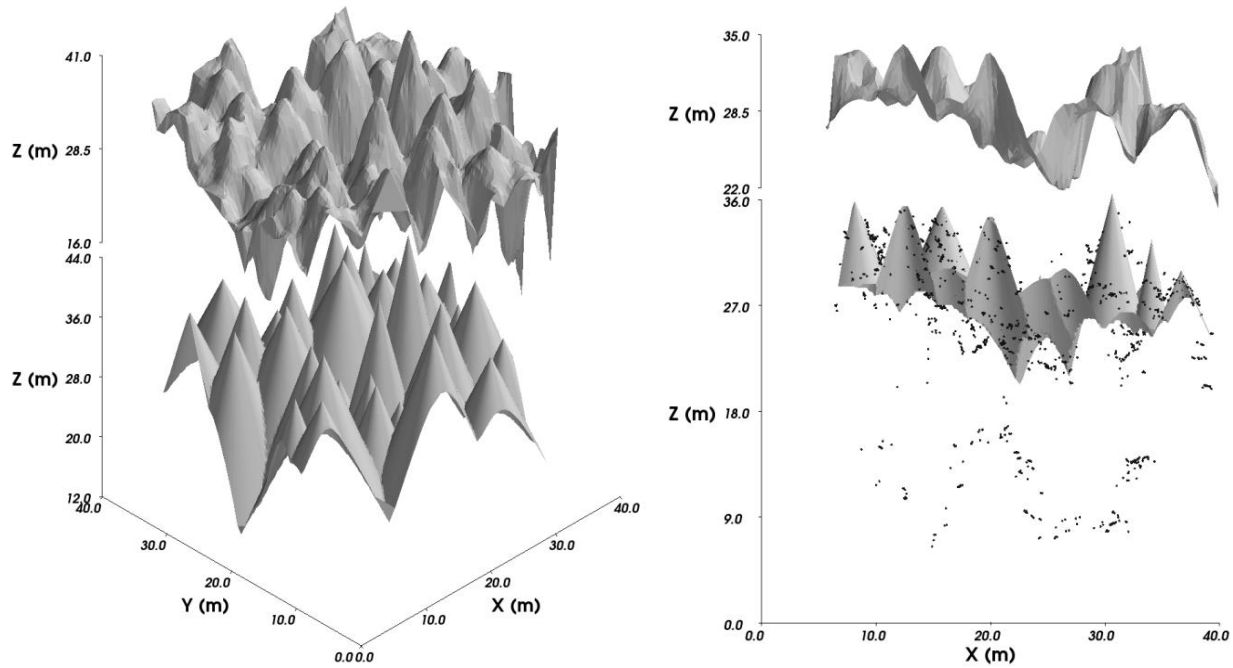

Figure 2.1a (left): Presentation of the PHM (bottom) and CHM (top) generated for plot 1. Figure 2.1b (right): PHM sliced and overlaid with the raw LiDAR point cloud. (Notice the stacked z-axes; The CHM is vertically offset and scaled along the top-most z-axis.)

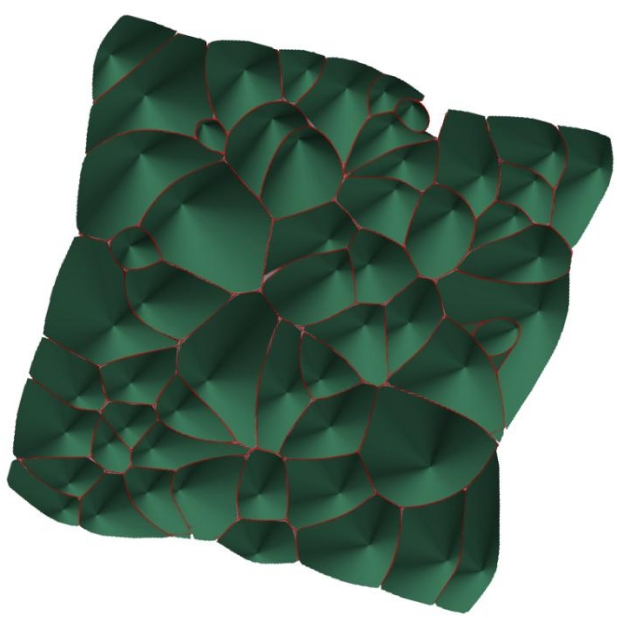

Figure 2.2: Demonstration of the delineation of individual tree crowns (red) based on geometric intersections of the individual tree crowns.

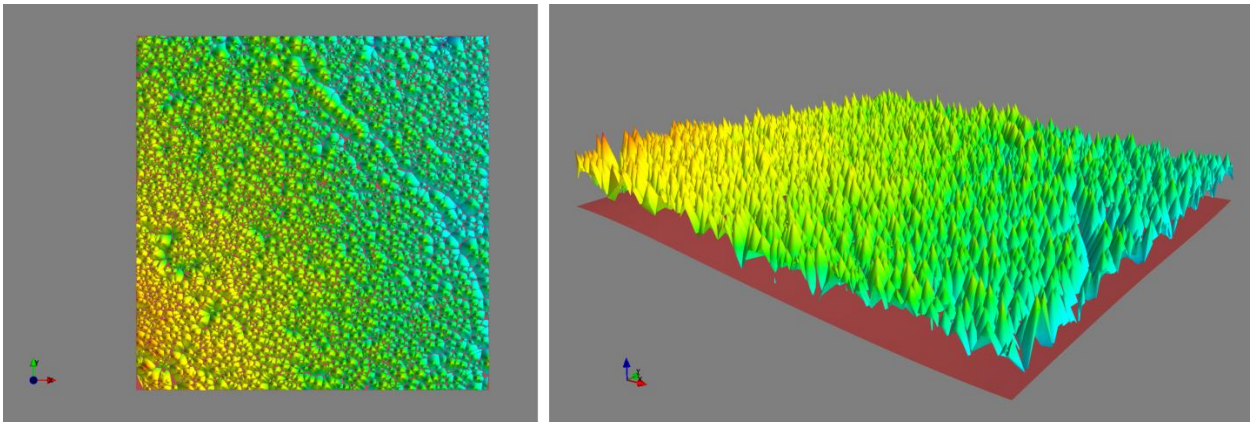

Figure 2.3: Illustration of the method covering a larger region of the airborne LiDAR data set (300 x 300m).

2.4. Discussion

LiDAR derived CHMs have been used to generate forest attributes to meet a wide-range of forest monitoring and inventory information needs (Wulder et al. 2008). However, the retrieval of tree level crown characteristics from CHMs remains challenging. This study demonstrates the effectiveness of the Hough transform to fit a basic primitive shape, here a cone, to individual tree crowns present in the LiDAR point cloud. After fitting the cones to the data, tree crown delineations can be trivially obtained as the geometric intersections between cones. The derived delineations and rough crown outlines provide a principal step towards the extraction of individual tree attributes and modeling at the tree level. While the current study focusses on the application and validation of the method at plot level, the method can equally be applied over larger areas of airborne LiDAR (Figure 2.3).

An additional benefit of the method, investigated in this study is the representation of tree height – that in CHMs and LiDAR data sets is often underrepresented due to porosity of the canopy to laser light and missing and smoothing of tree apexes. The bias found between PHM and raw LiDAR tree heights found in this study is consistent with the inherent bias in LiDAR data (Holmgren & Nilsson 2003; Næsset 1997; Nilsson 1996), and indicates potential for development of an automated correction procedure. Ongoing research will focus on this technique for retrieving inter-crown gap distributions and for use within simulation models such as ray tracing to model the radiation regime within tree crowns.

3. Automated reconstruction of tree and canopy structure for modeling the internal canopy radiation regime

3.1. Introduction

Canopy structure encompasses the spatial distribution of foliage as well as the architecture of the supporting woody components such as stems and fine branches. For coniferous canopies, the distribution of foliage elements is typically described around three levels of organization (Oker-Blom 1986): 1) the clumping of needles into shoots, 2) the clumping of shoots around branches, and 3) the clumping of the canopy into crowns. This complex arrangement of foliage elements increases radiation penetration to lower canopy strata (Oker-Blom 1985, 1986; Stenberg et al. 1995a) and affects the physiological adaptation of foliage elements to their immediate radiation environment, which has important implications for forest growth and productivity (Field 1983; Givnish 1988). Over large spatial scales, an exponential decay in radiation with canopy depth is observed. This rate of decay increases with leaf area and decreases with clumping; However, profound deviations from an exponential relation or even abrupt changes (lumiclines) in canopy radiation can be observed over finer spatial scales or along vertical canopy transects (Parker et al. 2001).

Canopy radiation can be computed using radiative transfer models that relate the absorption, reflection, and transmission of radiation to the biophysical characteristics of foliage elements and their spatial arrangement within the canopy. Radiative transfer models range from high spectral resolutions (Jacquemoud et al. 2009) to fine spatially explicit models of canopy structure (Ross & Marshak 1991; Welles & Norman 1991). These finer levels of geometric detail enable the comparison of simulated radiation budgets against *in situ* measurements (Mariscal et al. 2004), facilitate coupling with leaf or shoot-level functional models (Van der Tol et al. 2009; Wang & Jarvis 1990), and provide for a benchmark that can be used to evaluate model performances that operate at wider scales (Widlowski et al. 2006). The parameterization of the latter models is challenging and costly, due to the large number of structural parameters.

Ground-based laser scanning is a recent technology that has significant potential for direct and cost-efficient measurement of forest structure at very high resolutions. Canopy structure is digitized by emitting laser pulses across a wide field of view and by measuring the time of flight between each

emission, reflection off any scanned targets, and return at the instrument (Aschoff & Spiecker 2004). The recorded laser returns may be digitized as full waveform data, where the full return of laser energy is recorded at a nanosecond bandwidth, or as discrete returns, where data is represented as point clouds. In forestry, these data have been used for the modeling of stem volume and taper (Maas et al. 2008), branching structures (Bucksch et al. 2010), and - in combination with tree modeling techniques such as L-systems (Prusinkiewicz & Lindenmayer 2004) - the reconstruction of individual trees at levels of detail beyond the shoot scale (Côté et al. 2011, 2009).

The high level of structural detail of these data provides an important opportunity to parameterize geometrically explicit radiative transfer models. Modeling approaches have primarily focused on using point cloud information and generally require various assumptions on growth patterns and foliage characteristics. Methods typically start with the segmentation of returns into woody material and foliage, e.g. based on return intensities (Côté et al. 2009) after which geometries of tree trunks and branching can be obtained. To address effects of data obscuration and roughness of object surfaces (Côté et al. 2011; Liang et al. 2012) least squares optimization (Maas et al. 2008) and hypothesis testing and generating techniques such as Hough transform (Fleck et al. 2004) have been adopted. Coarse topological graphs of branching structures may be created using skeletonization algorithms such as provided by Verroust & Lazarus (2000) and Bucksch et al. (2010). More recent developments in modeling tree structure have combined laser scanner data with tree architectural software to represent levels of detail beyond the shoot. This is achieved by simulating the growth of fine woody structures that follow the spatial distribution of foliage returns or that adapt to simulations of the internal canopy radiation regime (Côté et al. 2009; Runions et al. 2007; Van der Zande et al. 2011).

A number of challenges remain in modeling of canopy structure at scales ranging from individual shoots to the crown level. Data obscuration makes the automation of the modeling pipeline challenging (Côté et al. 2011) and the level of detail of crown and canopy reconstructions needs to be balanced with computational tractability while remaining able to simulate canopy radiation profiles.

In this paper we present a methodology for the automated reconstruction of canopy structure from ground-based laser scanning data into three-dimensional mesh models that provide for modeling radiation transmission with canopy depth. The data used in the reconstruction pipeline are discrete but the point clouds are derived from full waveform data. We then compare and evaluate this method of reconstruction against an established method for deriving canopy radiation transmission from the full-waveform data and evaluate the radiative consistency between these two approaches. We conclude the

paper with a discussion on the use of these modeling techniques and opportunities for analysis of shoot level functioning.

3.2. Methods

3.2.1 Study area

A full study area description is available in section 1.5.

3.2.2. Data

Field data was collected in August 2008 at all four plots including diameter at breast height (DBH), tree height, and stem locations. Stem locations and heights were measured using a vertex (Haglöf, Sweden) hypsometer and compass bearing and DBH was measured using a diameter tape measure. Laser scanning data was acquired concurrently using the Echidna™ Validation Instrument (EVI) (Strahler et al. 2008). This laser scanner features a 1064 nm laser light source and digitizes the full-waveform of returned light energy at 2 Giga samples per second (Gs/s) and covers a field of view of 360° azimuth and 130° zenith. Data was collected using an angular sampling interval of 4 mrad and beam divergence of 5 mrad and range measurements were cut off if values exceeded 100 m. Five scans per plot were acquired comprising the four plot corners and the centre. North was marked in the scans using a reflective marker that was placed using a compass and coordinates of scan locations were recorded using GPS.

3.2.3. Data processing

3.2.3.1. Preprocessing

The full-waveform digitization from the EVI instrument is beneficial for analyzing surface scattering where the size of the scatterers is fine compared to the instrument footprint, as this leads to a degree of porosity of the medium to the laser beam that can be used for modeling the transmission of radiation through the canopy (Jupp et al. 2009; Yang et al. 2010). In this study, the full-waveform data was used to derive foliage profiles and canopy gap fraction, the latter is used as a measure of radiation transmission.

Single and last returns were used for creating virtual geometric models of the forest plots. These returns were obtained from the full-waveform information using methods described by Yang et al. (2013). The single and last returns were projected using the recorded azimuth and zenith angles of the respective laser shots into the 2D image domain (Andrieu et al. 1994). The same projection was then used to produce a suite of additional EVI outputs including return intensity, range, Cartesian coordinates and radial distance that was defined as the horizontal component of range.

All scans were aligned to north using the reflective target, then six-degree-of-freedom offsets between corner scans and the centre scan were determined manually by interactively shifting and rotating the point clouds, acknowledging that automated routines for coregistration already exist (Gruen & Akca 2005). A digital elevation model (DEM) and canopy height model (CHM) were created using co-registered data of five scans per plot and using a grid-cell size *G* (40 cm) and smoothing using a 1.5m Gaussian kernel (σ_K=1m) in accordance with values previously used in similar forest types (Ferster et al. 2009). Additionally, local maxima were derived from the CHM using the level-set method (Kato et al. 2009) and a Parametric Height Model (PHM) was created using these local maxima and the CHM (Chapter 2). The PHM model outlines individual crowns by fitting cones to a CHM or to raw LiDAR data so that the number of returns within threshold distance *m* (10cm) from the cone surface is maximized. Transmittance of the DEM was set to zero.

Subsequent processing addresses the detection of stem locations and the retrieval of stem diameters (§3.2.3.2.), and the derivation of geometric models of the forest plots (§3.2.3.3.). The virtual plots are then used to simulate canopy radiation transmission (§3.2.3.4.).

3.2.3.2. Stem detection and reconstruction

Tree stems were segmented from single scans. The segmentation was implemented using the medial axis transformation (MAT) and regression analysis of object boundaries. The medial axis of a polygonal or polyhedral shape is a thin curve or curved plane centred within the boundaries of that shape (Das et al. 2011; Martinez-Perez et al. 1999; Yuan et al. 2011). A large number of methods exist for the derivation of the MAT (Siddiqi & Pizer 2008). In this study, the MAT was derived from a distance transformation. First, using radial distance, solid objects such as stems, branches, and ground hits were crudely separated from permeable targets (foliage) by identifying pixels whose range did not deviate

from all 8-connected neighbouring pixels by more than a tolerance, δ (Figure 3.1, step 1). In this binary image, apparent edges in the range image are zero while surfaces in the range image are non-zero. Second, from this binary image the distance transformation (DT) was computed (Figure 3.1, step 2) that represents the distance from any surface pixel to their nearest edge pixel, e.g. (Shih & Pu 1995). Segments of surface pixels in the DT show an elevation in values towards the segment centres, resulting in the appearance of ridge-lines along the long axis of tree stems. Third, the MAT was derived from the distance transformed image using the sign-change of the image derivative that was computed along image lines (Siddiqi & Pizer 2008) (Figure 3.1, step 3). Association of surface pixels to their nearest edge pixels allows for the conversion from a medial representation (MR) to a boundary representation (BR) (Siddiqi & Pizer 2008) (Figure 3.1, step 4). A set of boundary pixels was obtained and classified into P_{left}, and P_{right} relative to the medial axis (P_{MAT}). An illustration of the method for stem detection is provided in Figure 3.3.

Tree stems were detected using the MR and BR based on three filtering criteria: 1) a measure of normalized cross-correlation, *r*, between the paired boundary lines, 2) change in local orientation along the medial axes, ξ, and 3) the number of pixels contained in the medial axis, n_{MR} (Figure 3.1, step 5). The normalized cross-correlation, *r*, was computed between corresponding pixel y-coordinates of the paired boundary lines:

$$\sum_{j}^{k} \frac{\left(P_{left,y,j}-\overline{P_{left,y}}\right)\left(P_{right,y,j}-\overline{P_{right,y}}\right)}{\sigma_{P_{left,y}} \cdot \sigma_{P_{right,y}} \cdot k} \qquad \text{(eq. 3.1)}$$

where *k* is the number of paired boundary pixels associated with the medial axis and $\sigma_{P_{left,y}}, \sigma_{P_{right,y}}$ the standard deviations of y-coordinates. The normalized cross correlation is frequently used in image processing and computer vision, for example, to match stereo pairs (Fua 1993). The local orientation was computed for every medial axis pixel as the slope, in the image coordinate frame, of the line through the associated, paired boundary pixels ($P_{left,j}$, $P_{right,j}$). The parameter ξ was computed as the change of orientation between two adjacent medial axis pixels ($P_{MAT,j}$, $P_{MAT,j+1}$) and medial axis pixels for which the local orientation changed by more than a user-specified threshold were removed. After filtering for ξ, the parameter n_{MR} was used to filter any small objects that were considered too short to

reliably compute a normalized cross-correlation. Filtering for *r*, ξ, and n_{MR}, detects tree stems. A sensitivity analysis around stem detection parameters was conducted by varying one parameter at a time over specified ranges (Appendix A.1.1.). Stem diameters were computed along unobscured, detected stems following (Strahler et al. 2008):

$$t = \sin\left(\alpha_{span}/2\right) = \frac{D/2}{R+\frac{D}{2}} \qquad \text{(eq. 3.2)}$$

$$D = 2R\frac{t}{1-t} \qquad \text{(eq. 3.3)}$$

where *R* is the range, *D* the stem diameter, and α_{span} is the angular width spanned by the tree trunk. Stem centres were computed from the original radial distance that relate to the stem surface (i.e. bark), and derived stem diameters.

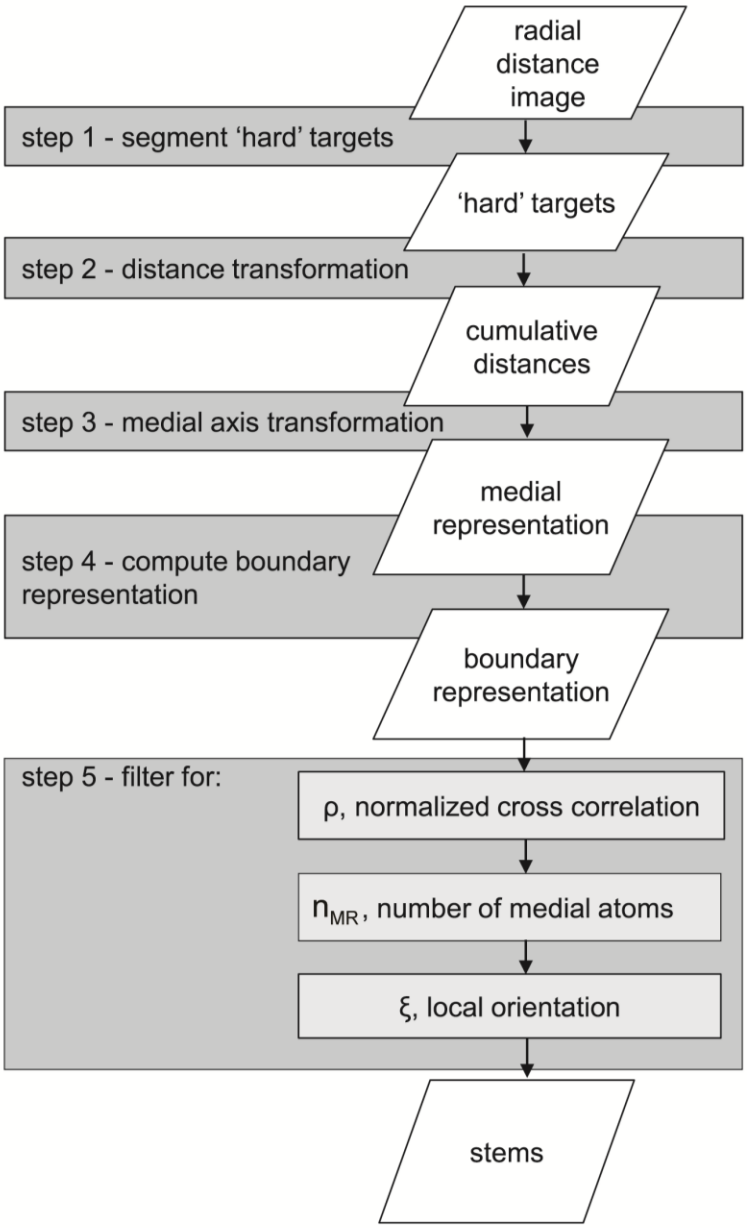

Figure 3.1: Schematic representation of the stem detection algorithm showing the individual steps of processing. See text for explanations about the individual processing steps.

3.2.3.3. Mesh modeling

Stem segments detected in the single scans, that overlapped in co-registration were merged into a single stem object. To reduce impacts of co-registration errors as well as errors in diameter attribution between scans, the merged data were smoothed by averaging stem attributes along 0.5 m height intervals. Gaps in stem representation may occur, however, due to the effects of occlusion in ground-based laser-scanning data. To bridge these gaps, B-splines were fitted through all stem segments and tangent vectors were computed at every spline node. For every possible pair of segments, a connecting spline was fitted using the same nodes as contained in the individual splines combined, and from the paired nodes the angles (s) between tangent vectors (connecting spline vs. the two separate splines) were computed, except for a number of six nodes centred around the joint of the two segments, due to sensitivity of splines towards the extremes (Daniels II et al. 2008). If a pair of segments was shorter than six nodes in length, the pair was skipped. If these angles or the z-component of the gap length (L_Z) exceeded user specified values s_{MAX}, $L_{Z,MAX}$, respectively, the two segments were interpreted as not belonging to the same tree. Alternatively, any two segments were assessed to belong to the same tree stem if segment w_j was the smoothest connecting segment for w_i and if w_i was the smoothest connecting segment for w_j too; this is analogous to stereo matching criteria used by Fua (1993).

After this step, data occlusion near the trunk base and tree top may remain. To recover these final missing parts, an approach was developed where the trunks were extended towards the ground and the tree tops. Liu et al. (2005) describe an approach that reconstructs curves from point cloud information based on the tangential flow. Their algorithm produces a B-spline that grows along its two end-points using a cylinder that is aligned with the spline's tangent and that is used to follow apparent curves in the point cloud. Given that tangential vectors of trees are generally vertical, a solution of reduced complexity was sought in this study. The point cloud was compressed along the z-axis (i.e. height-axis) by a factor 20 and a cylinder with radius 2.5 m was placed around the top of the detected stem segment. Iteratively, the nearest return within 30 cm above the stem top and within the cylinder was added to the sequence of spline nodes and using the new top additional returns were added until no additional returns were found. The same procedure was used to extend the stem segments towards the ground.

The set of cones derived from the PHM, each representing an individual, dominant tree crown, was matched with the tree stems by locating, for every cone tip, the nearest stem top and for every

stem top the nearest cone tip. If matches were mutual, a connection was registered (Fua 1993). Stem diameters were then assigned using linear extrapolation towards the stem tops, while diameters were kept constant towards the DEM. The transmittance of the stems and the forest floor was set to zero.

Tree crowns were modeled using a combination of laser-derived crown dimensions and Arbaro, an open source tree modeling software (Weber & Penn 1995; http://arbaro.sourceforge.net/, last accessed on December 31, 2013) that provides for the modeling of deciduous, coniferous, as well as herbaceous vegetation. Plants modeled in Arbaro behave as if they were solitary, and do not exhibit competition for light with neighboring vegetation. Arbaro uses an extensive list of parameters including branch lengths in relation to parent branches, the number and curvature of branches, as well as random variations around each parameter. To reduce the number of modeling parameters, no random variation was considered and a template coniferous tree crown was created whose dimensions and shape could be adapted to fit the stem shapes and crown outlines derived from the point clouds. The template tree was defined with a crown depth of 60% of tree height and a constant internode distance (0.25 cm), and a distribution of branch insertion angles and branch curvature that resemble the plagiotropic and heliotropic distribution of branches in the lower and top canopy strata, respectively (Halle et al. 1978). Crown depth was estimated from field observations of dominant trees and was computed as the height of first living branch to the total tree height. Internode distance was chosen to balance the frequency of first order branching with computing resources, while ensuring that canopy layering was abundantly sampled. Heights and opening angles of cones in the PHM were used to define tree height and lengths of first order branches and the crowns were draped over the laser-reconstructed stems to account for sweep and lean. To avoid crowns intersecting one another and to ensure they resemble natural competition in stands, branches were scaled to individual tree growing spaces that were computed by tessellating the plot space to the nearest tree stem based on the rationale that locations within the plot are likely to be populated by foliage from the nearest stem, rather than a stem located further away. To simplify canopy representation without comprising the radiative consistency, planar polygons were fitted to clusters of first and second order branches. The use of planar surfaces builds on traditional concepts used in layered crown and canopy models (Oker-Blom et al. 1991; Ross & Marshak 1991). In contrast to the use of uniform canopy layers in one-dimensional radiative transfer models, the current use of planar polygons provides for radiative transport between crowns and whorls. After reconstruction of the plots, the mesh models were decimated to 50,000 triangles to reduce computing costs of radiative transmission simulations (§3.2.3.4.).

Uncollided transmission of radiation through the planar polygons was expressed as the gap fraction, $g(\vartheta_i)$, a measure similar to the foliage silhouette-to-total-area ratio used in modeling shoot-level albedos (Stenberg et al. 1995b). This gap fraction is a function of illumination geometry relative to the normal angles of the branch facets. For incoming rays under a 0° normal angle, the gap fraction was set to 15% based on photographical measurements perpendicular to the predominant shoot direction that generally ranged between 10 to 20%, and the value of gap fraction decreased linearly with the cosine of the ray-normal-angle. The sensitivity of this parameter was assessed by changing $g(\vartheta_0)$ from 5 to 30% in steps of 5% (Appendix A.1.3.).

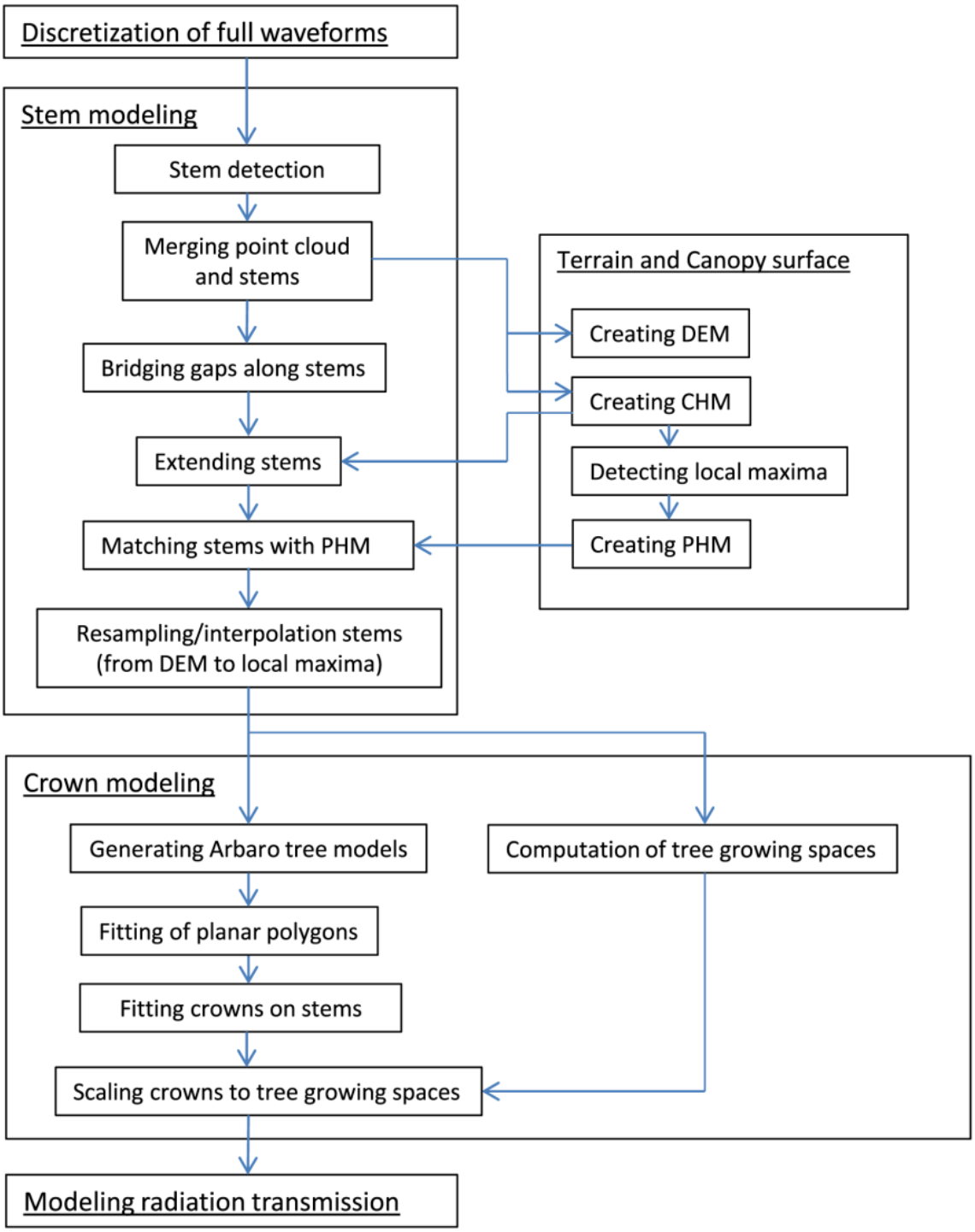

Figure 3.2: A schematic of the complete processing pipeline used for reconstructing plots.

3.2.3.4. Modeling the internal canopy radiation regime

The radiative consistency of the produced mesh model was validated against EVI-derived measurements of gap probability (Jupp et al. 2009). Gap probability, $P_{gap}(\theta, R)$, is the probability of having no scattering material (e.g. foliage, woody material) between the laser scanner and a point at a specified range (R) under a specified zenith angle (θ) and is derived as:

$$P_{gap}(\theta, R) = 1 - \frac{1}{\rho_a} \int \rho_{app}(\theta, R) \cdot dR \qquad \text{(eq. 3.4)}$$

where ρ_a is the normal reflectance of a face and ρ_{app} is the apparent reflectance that is determined from the recorded waveform of returned light energy as:

$$\rho_{app}(\theta, R) = \frac{I(R,\theta) \cdot R^2}{K(R) \cdot \Phi_0} \qquad \text{(eq. 3.5)}$$

where $I(R, \theta)$ is the measured intensity at the range R, and angle θ. K(R) is a telescope efficiency factor and Φ_0 is the outgoing energy (Jupp et al. 2009). P_{gap} is computed in zenith angle bands that are typically between 5 to 20° in width. A vertical profile of P_{gap} was computed from eq. 3.4 for each plot using the center scans.

P_{gap} provides for the derivation of foliage profiles as:

$$L'(z) \approx -\log\left({P_{gap}}'(z)\right) \qquad \text{(eq. 3.6)}$$

Foliage profiles were computed for zenith angles ranging from 55 to 60 degrees (Lovell et al. 2003) and were compared against the vertical distribution of facet areas of the mesh models.

Vertical profiles of gap probability were derived from the mesh models by forward ray tracing (Appendix A.2). Hemispherical irradiance was simulated using 5000 light sources that each emitted a single beam of collimated light directed towards the plot origin. The number of light sources was to balance the resolution of directional variation in hemispherical illumination such as caused by direct sun and cloud cover with computational cost of the model simulations. These light sources where distributed about a vertical axis, so that the distance to that axis decreased exponentially with the sample's rank and the angular distance between samples was approximately constant (i.e. one light source corresponds to 1.26 milli-steradians; for details on methods see e.g. Piccini et al. 2011 and Vogel, 1979). In this study, a 100% diffuse sky was simulated by assigning equal intensities to all light sources, and this relates to the condition of a complete overcast. At every ray-mesh intersection, the probability of uncollided transmission, τ, through the facet (i.e. ground, stem, foliage) was determined from the directional gap fraction, $g(\vartheta_i)$, (§3.2.3.3) using the angle between the ray and the normal angle of the intersected facet. At every intersection, P_{hit} was computed as $(1-\tau)$ and the propagated, uncollided irradiance as $\tau \cdot E_i$. Vertical hit distributions were derived as the fraction of hits within 10 cm height bins and were compared with the EVI P_{gap} profiles derived from a below-canopy perspective. As indication of correspondence, 50 samples at heights ranging between 0 – 30 m were randomly drawn from the simulated and full-waveform derived P_{gap} profiles centered at 57.5° and Pearson correlation coefficients were computed for each plot. The processing pipeline is summarized in figure 3.2.

3.3. Results

3.3.1. Stem detection

Figure 3.3 shows the detection of stems for plot 1. On average, stem detection was calculated within 3 to 5 seconds per scan, making the technique extremely computationally efficient. The threshold parameters used for stem detection were δ=0.30 m, r=0.95, ξ=15°, and n_{MR}=24. Detection was limited to stems covering a minimum cross section of 3 to 4 pixels. Figure 3.4 shows the detection rate by radial distance measured over all 20 scans, from which cumulative detection rates can be obtained through integration. For distances up to 10 m, 93% of trees were detected. In general, trees not detected within 10 meters showed excessive branching, or were snags. At distances up to 15 m, 85% of trees were detected, while at distances up to 20 and 25 m only 67% and 56% of the trees were detected, respectively. This rapid reduction in detection rate with distance is a result of decreasing spatial point

density with distance and effects of occlusion. Using the co-registered data, an average of 9.25 trees per plot totaling 9.8 % of trees detected in the field inventory were not located in the EVI-derived stem map as a result of occlusion or decreasing resolving power with range. The method was insensitive against returns obtained from branches, albeit trees around this geographical location generally have sparse branch densities along the lower bole sections. The method was unable to detect some younger trees with heavy branching structure and foliage along the entire visible stem, and distant trees. Errors of commission were few and limited to objects close to the scanner and were eliminated later in the modeling pipeline as stems need to have a certain length.

DBH estimates were found to correlate well with field observations (R^2 = 0.82; Figure 3.5); However, a decrease in accuracy was observed, as expected, with distance from the scanner. Field measured DBH was underestimated ($p < 0.05$) by EVI ($\overline{EVI_{DBH}}$ = 22.5 cm vs. $\overline{Field_{DBH}}$ = 27.3 cm), consistent with findings of Strahler et al. (2008) and Yao et al. (2011). Figure 3.6 shows field detected and EVI detected tree stems for plot 1, with the size of the markers representing DBH. Mis-registration between compass (vertex) determined tree locations and EVI derived stem locations may be attributed to individual scanner setups as well as to distance from the plot centre.

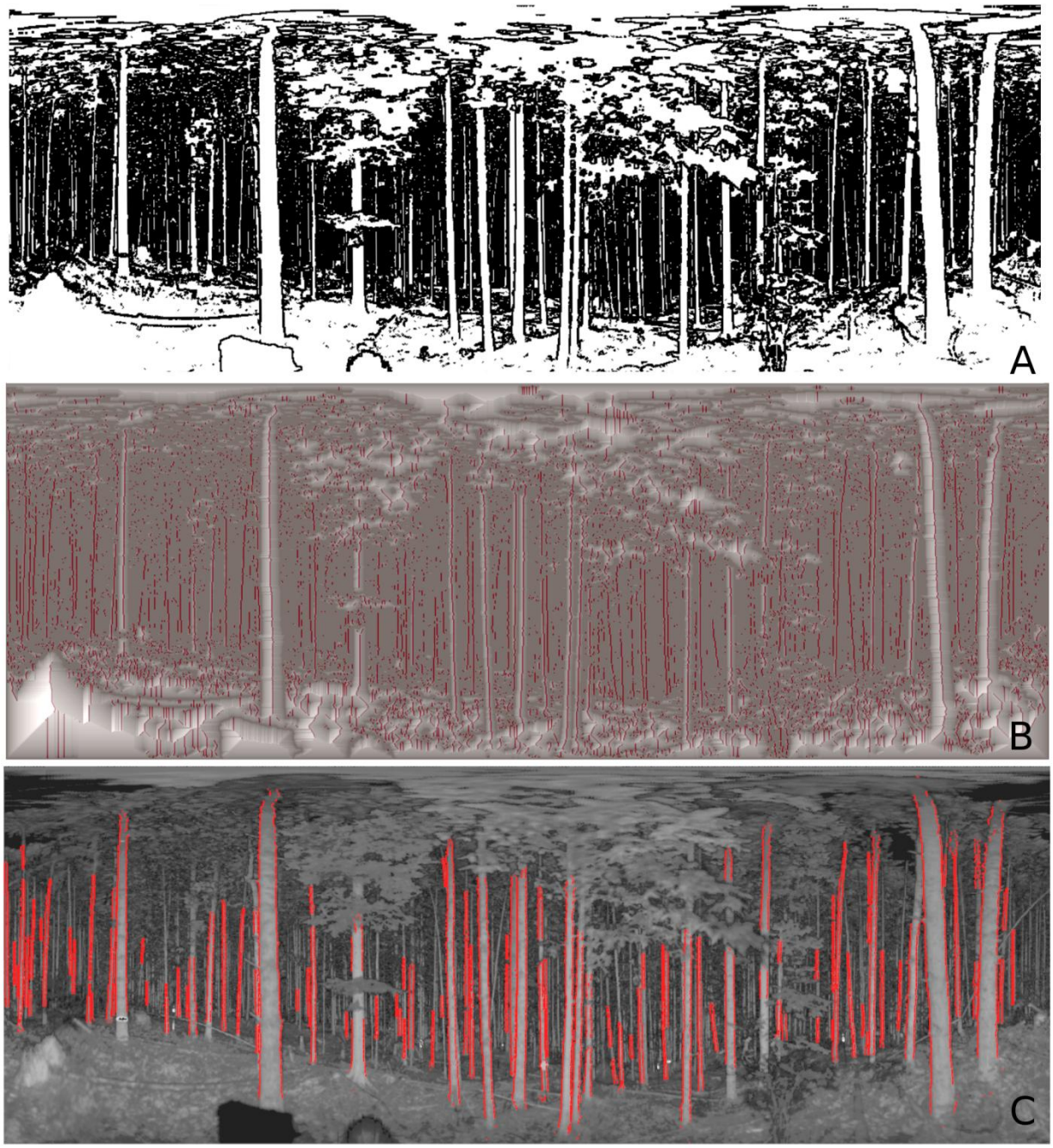

Figure 3.3: Binary image showing clusters of pixels in white that have all 8-connected neighbors within range δ (a). Distance transformation and projection of the Medial Axis Transformation overlaid in red (b). Stem detection overlaid on laser intensity image (c). Pixels along the horizontal axis represent equal steps along azimuthal directions, while pixels along the vertical represent equal steps in zenith angles.

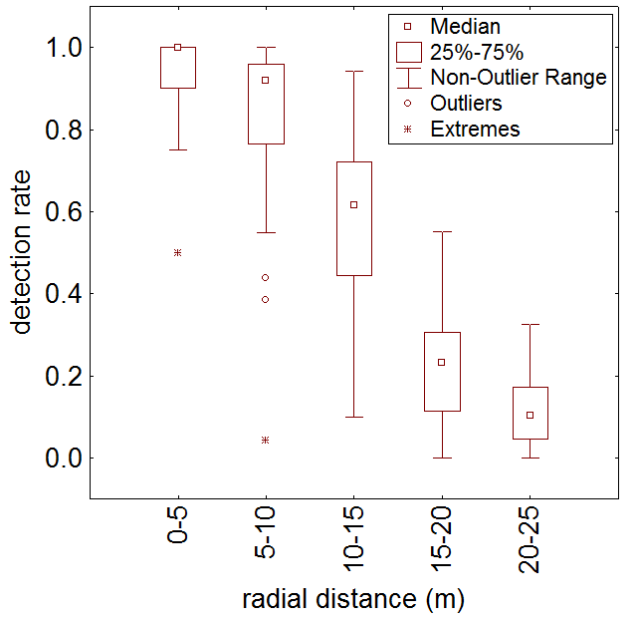

Figure 3.4: Detection rate as a function of radial distance from the scanner's location.

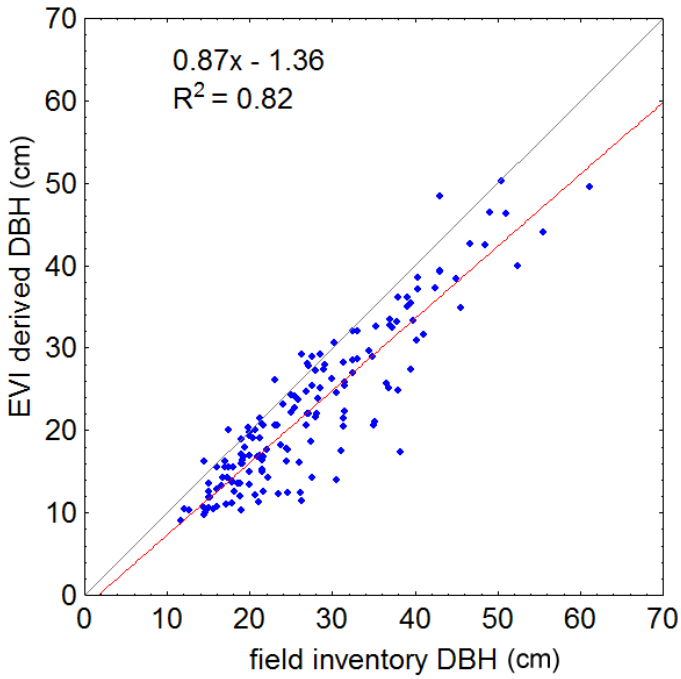

Figure 3.5: Linear regression of EVI-derived, and tape-measured diameter at breast height indicates a negative bias among diameters derived from EVI data.

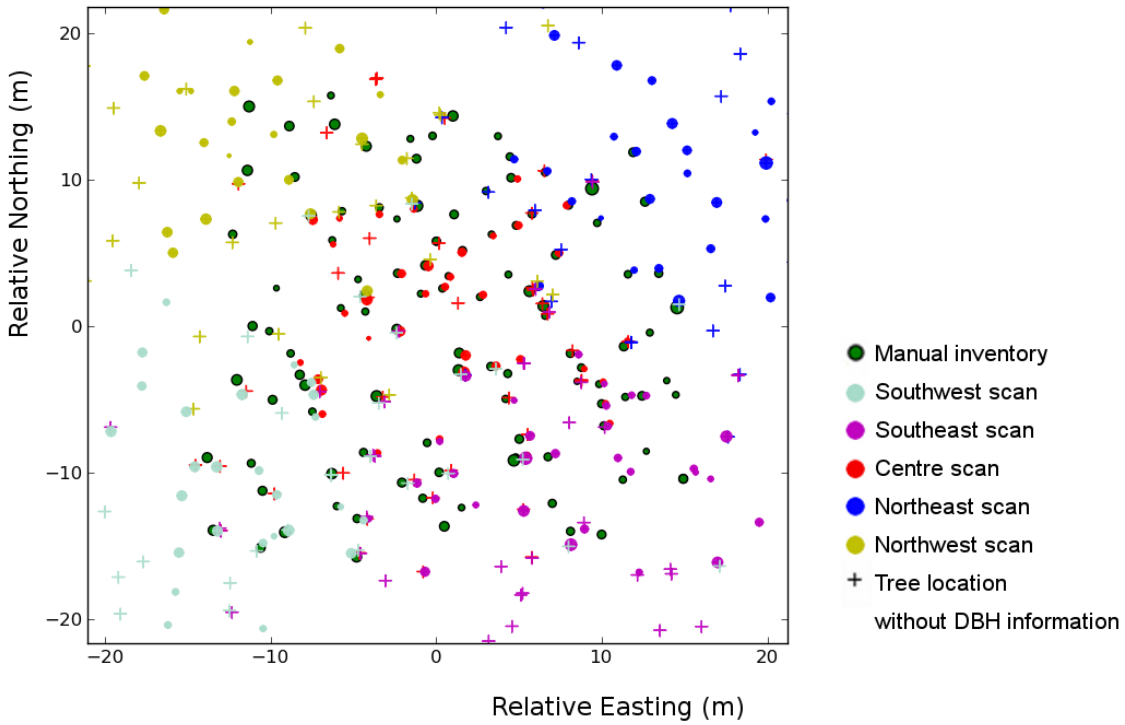

Figure 3.6: Co-registration of TLS stem locations for the north-east (blue), south-east (magenta), north-west (yellow), south-west (cyan) and centre (red) locations within the plot, against field-measured stem locations (green) for plot 2. Diameter estimates are indicated by the size of the markers. Trees that were detected in the TLS scans and for which no DBH information was derived as a result of partially occluded stem-edge data are shown in their respective scan colours as plus-signs (+).

3.3.2. Mesh modeling

Accuracy of the stem modeling was assessed by interpreting the co-registered point clouds, and showed that the merging of individually detected tree stems and stem parts overcame many of the major issues associated with occlusion. Figure 3.7 provides an illustration of the stem reconstructions and shows that stems were modelled well into the higher strata of the canopy allowing consistent matching with the individual crown tops. In some cases, however, coregistration-errors caused that individual trees could not be correctly merged for the final mesh model, and these cases resulted in the reconstruction of two stems, instead of one. The implications of this on the formation of tree growing spaces seemed minimal as the combined set of growing spaces for these trees and their reconstructed crowns would act in the

same manner as that it for a single tree would (Morsdorf et al. 2004). The creation of tree growing spaces was effective in delineating both dominant as well as suppressed trees (data not shown). The method does not guarantee that individual branches always get assigned to their true parent stem. In all cases, however, the foliage gets assigned to their nearest stems. In figure 3.8, a demonstration is provided of the fitting of planar polygons to the crowns of the Arbaro tree models, the fitting the modelled crowns to the reconstructed tree stems, and scaling of the crowns to the growing spaces. Figures 3.9 and 3.10 show the reconstructed virtual forest plots using the Arbaro tree models parameterized with tree height, and crown taper, that were derived from the EVI data set. Individual tree crowns did not intersect one another in the mesh models, as a result of scaling the crowns to the tree growing spaces. The Arbaro tree model output coarsely resembled the clumping of foliage around branches and into crowns, typical for conifers (Oker-Blom 1986), although the exact placement of foliage material could not be validated at tree level against the current data set.

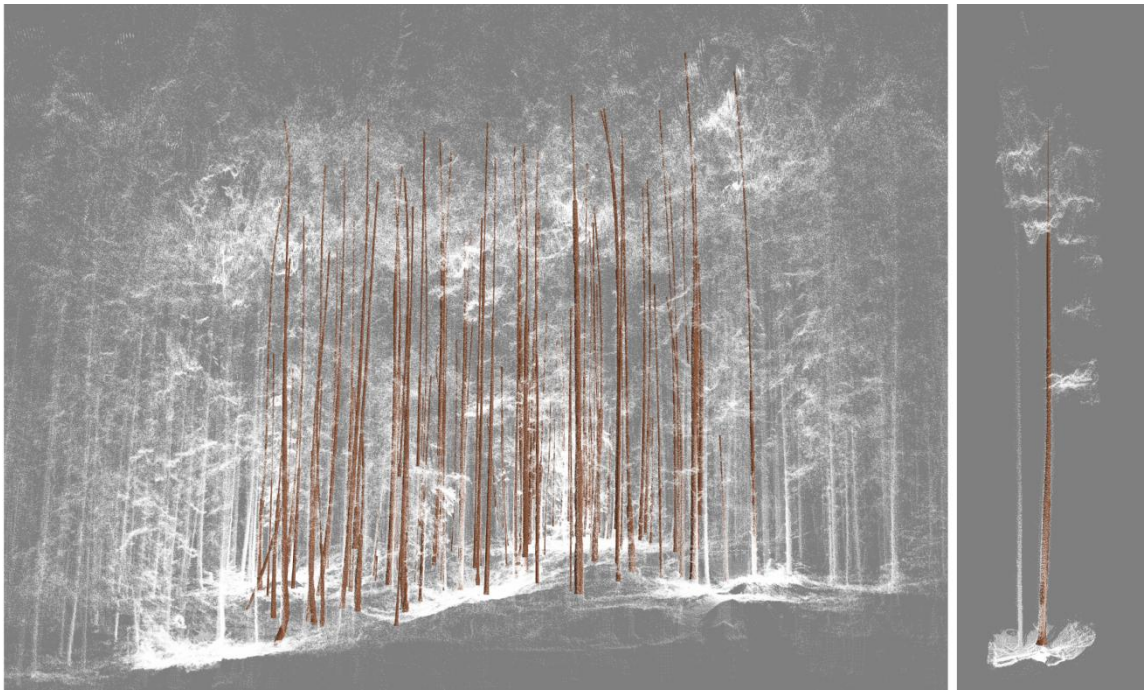

Figure 3.7: 3D map of stem reconstructions for DF49 plot 1 (a). Detail of one reconstructed tree and its neighboring point cloud (b). (The neighboring tree visible in the point cloud was also detected.)

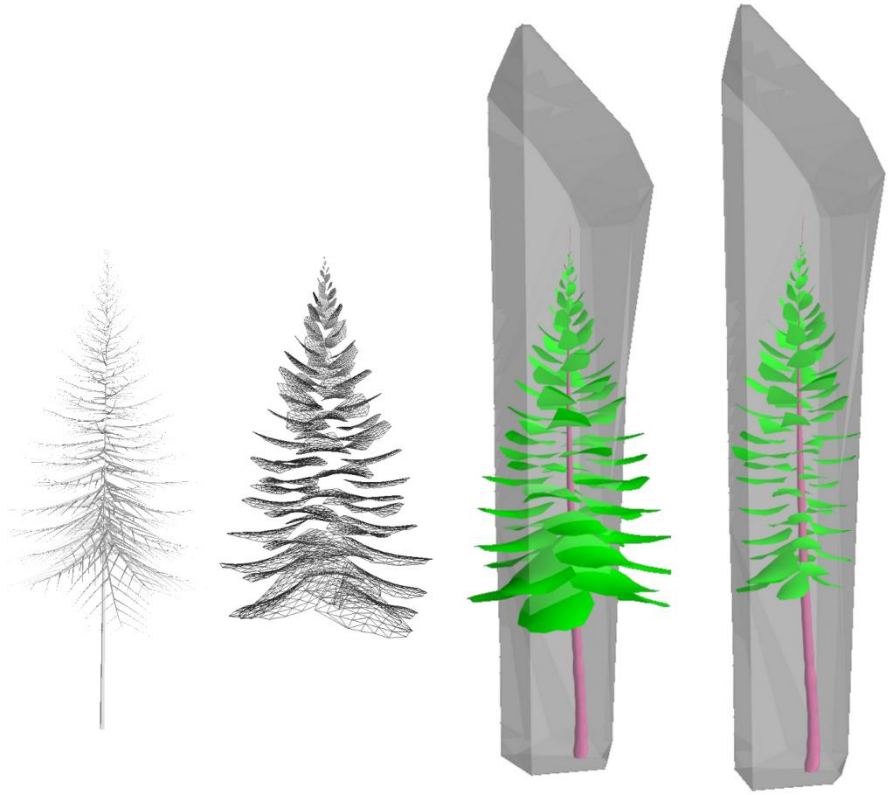

Figure 3.8: Fitting of planar polygons to Arbaro branch models and scaling of crowns to the tree growing spaces.

It was found across all plots that tree heights in the mesh model were considerably shorter than field measured heights; this is also reflected in Figure 3.11 showing facet area profiles of the mesh models against height vs. EVI-derived leaf area profiles against height. Some of this underestimation may be explained from a decreasing ability to detect discrete returns with increasing path length through the canopy, while additional contributions were associated with the creation of the CHM, and PHM, and decimation of the Arbaro tree crown models that resulted in the removal of fine branches located at the tree tops. In contrast to the EVI foliage profiles, the facet area profiles include a profound ground peak that is due to the inclusion of the ground terrain in the mesh models. Significant differences between foliage profiles and facet area profiles remain for the mid-canopy (around 15m) that can be explained from differences in definition that may be resolved by foliage density attribution to the individual facets.

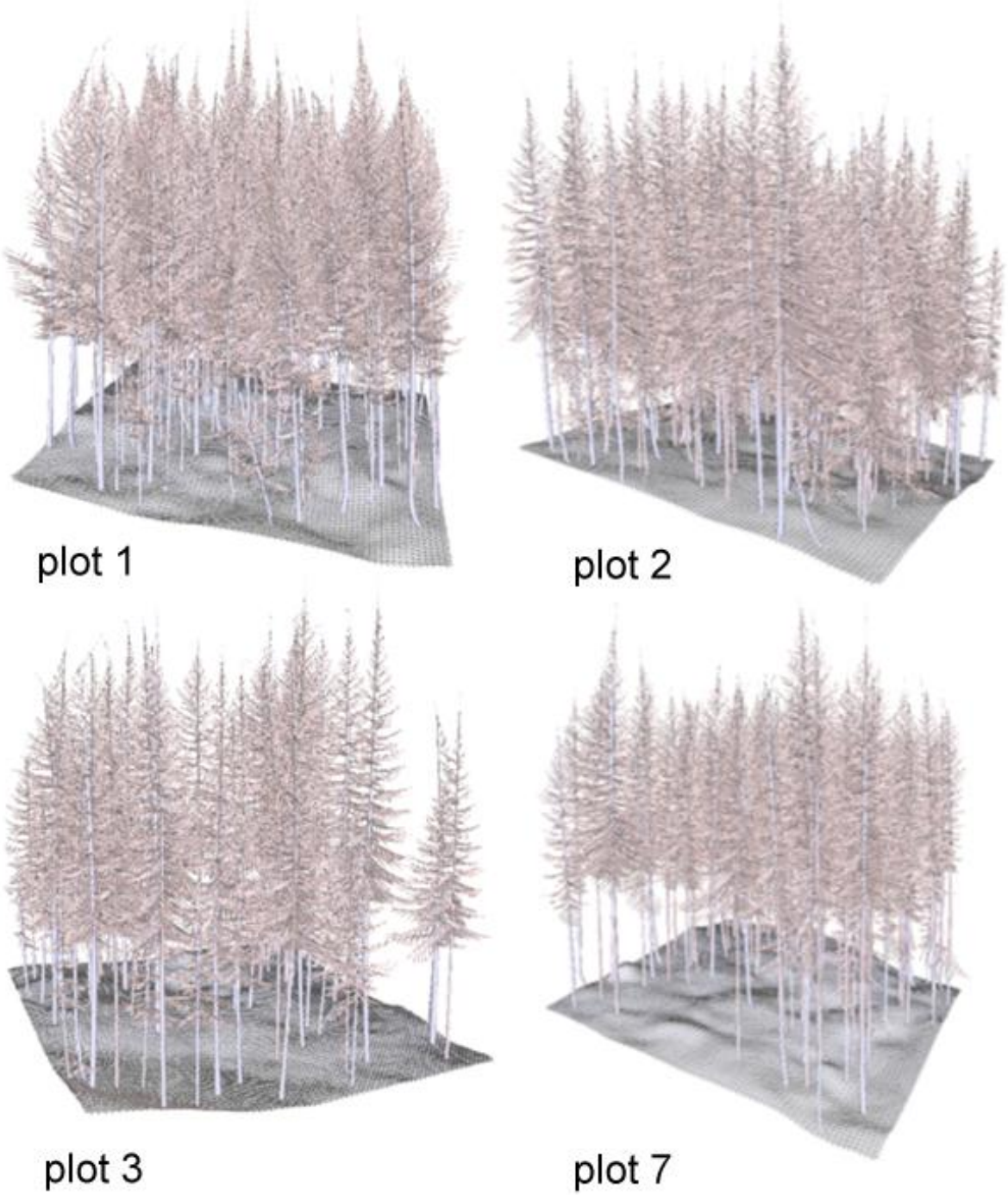

Figure 3.9: Illustration of reconstructions for all four plots. Shown are the woody skeletons produced by Arbaro software and fitted to the tree growing spaces.

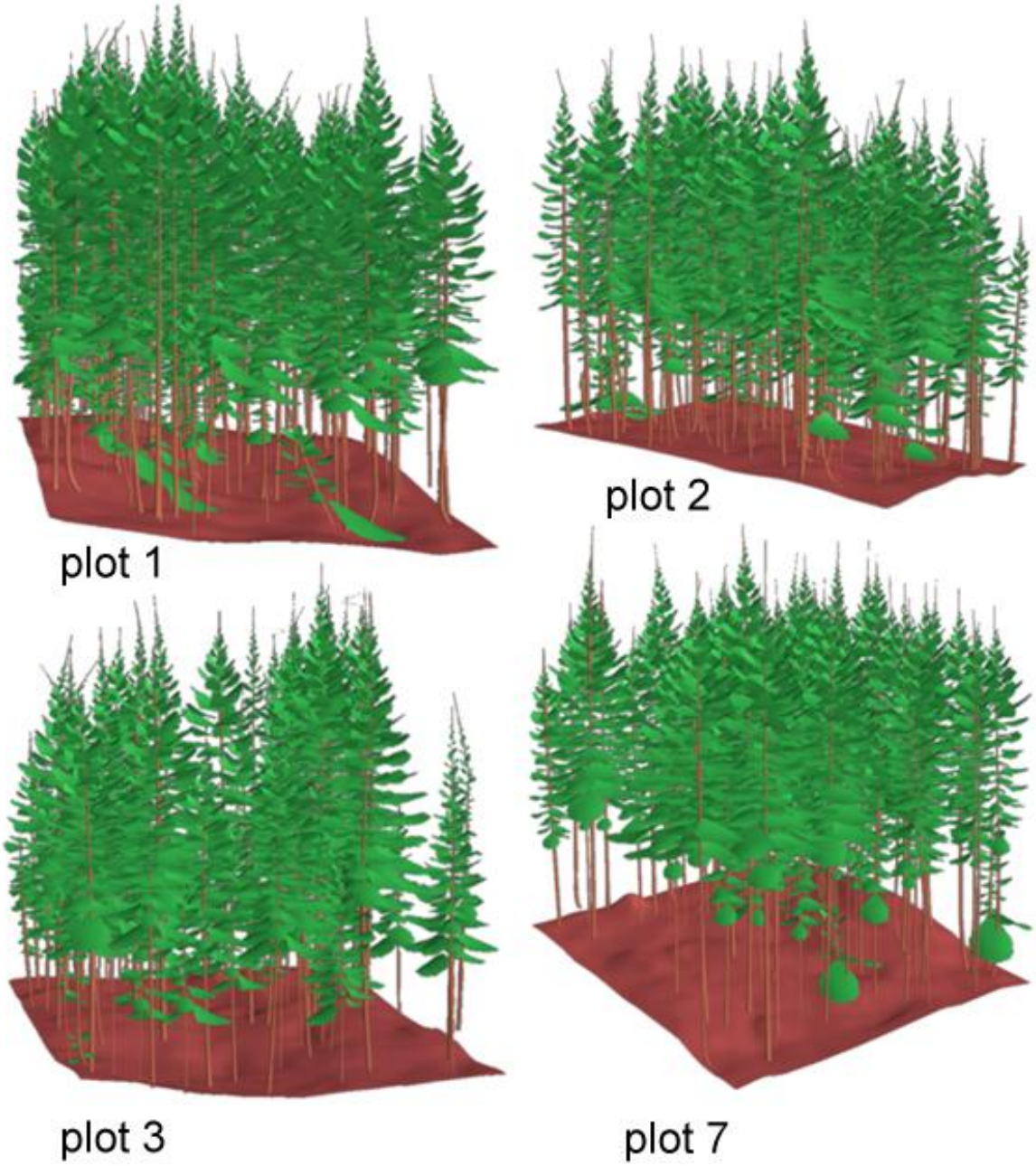

Figure 3.10: Illustration of reconstructions for all four plots. Shown in this illustration are the planar polygons to simulate the layering of foliage elements in coniferous canopies.

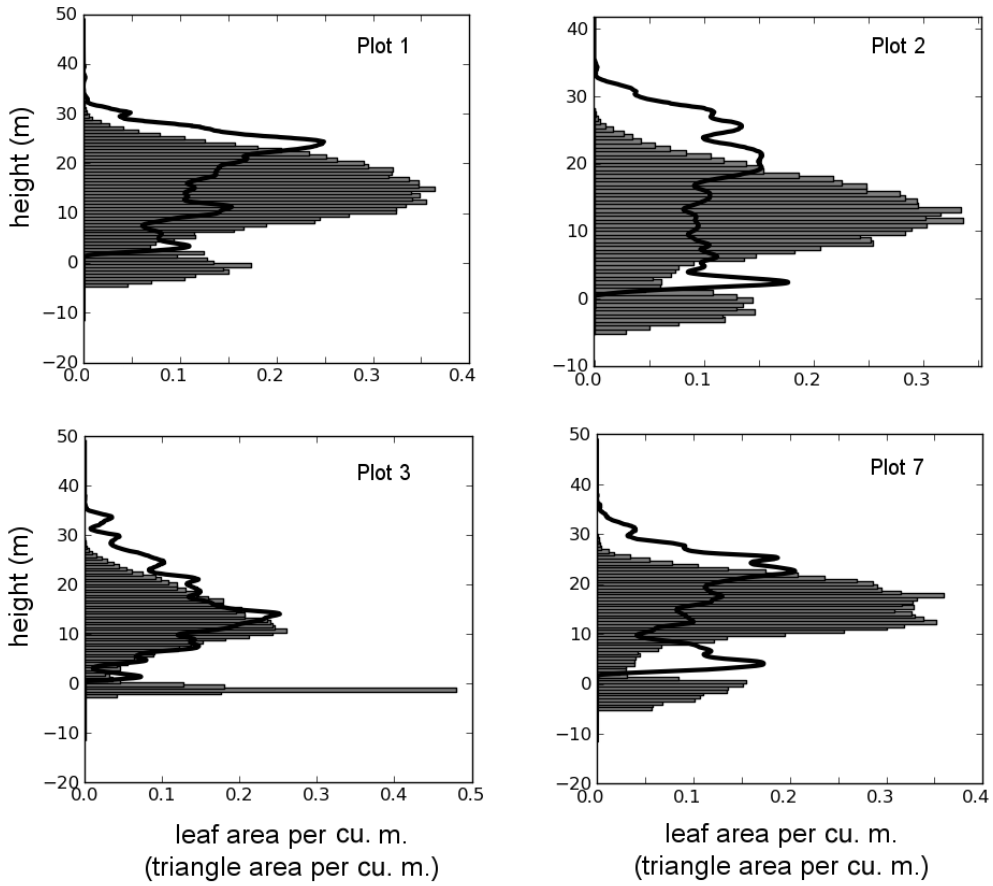

Figure 3.11: Facet area profiles (bars) derived from mesh reconstructions and point cloud information and full-waveform EVI derived leaf area profiles (solid black line) per cubic meter for the four plot reconstructions. Heights [m] are relative to plot origin.

3.3.3. Modeling radiative transmission properties

Figure 3.12 shows the modeled hit distribution against height. Individual data points represent fractions of hits within 10 cm height bins, while the fitted lines show a polynomial fit and moving median (1 m window size) through these data points. A sixth-order polynomial fit was chosen to capture peaks in absorption by the canopy volume as well as ground vegetation. Simulated hit distributions showed an increase around the mid-canopy where foliage and facet area densities are highest and also showed increasing variation in light interception with canopy depth (figure 3.12). The highest probability P_{hit} for single facets was observed near the tree tops and around canopy gaps.

Vertical profiles of P_{gap} were computed using zenith angles centered around 17.5°, 27.5°, 37.5°, 47.5°, and 57.5° using a 5° bandwidth (figure 3.13). A strong dependence of the P_{gap} profiles on the zenith angle was observed. For larger zenith angles, values of P_{gap} were considerably smaller than corresponding values at smaller angles as a result of path length through the canopy. Figure 3.13 also shows the simulated hit distribution profile as a function of height (thicker black line) and shows consistent behavior with trends in the full-waveform derived profiles. The Pearson correlation coefficient computed between 50 random samples taken from the simulated hit distribution and full waveform P_{gap} distribution centered at 57.5° was 0.97, 0.95, 0.97 and 0.91 for plot 1, 2, 3, and 7, respectively ($P << 0.01$). A noticeable difference is observed at heights over 20-25 m that can be addressed to the difference in illumination geometries between the real and simulated results. While the EVI has a below-canopy perspective, the simulated results are obtained from an overhead perspective and resemble the down-welling radiation from the sky.

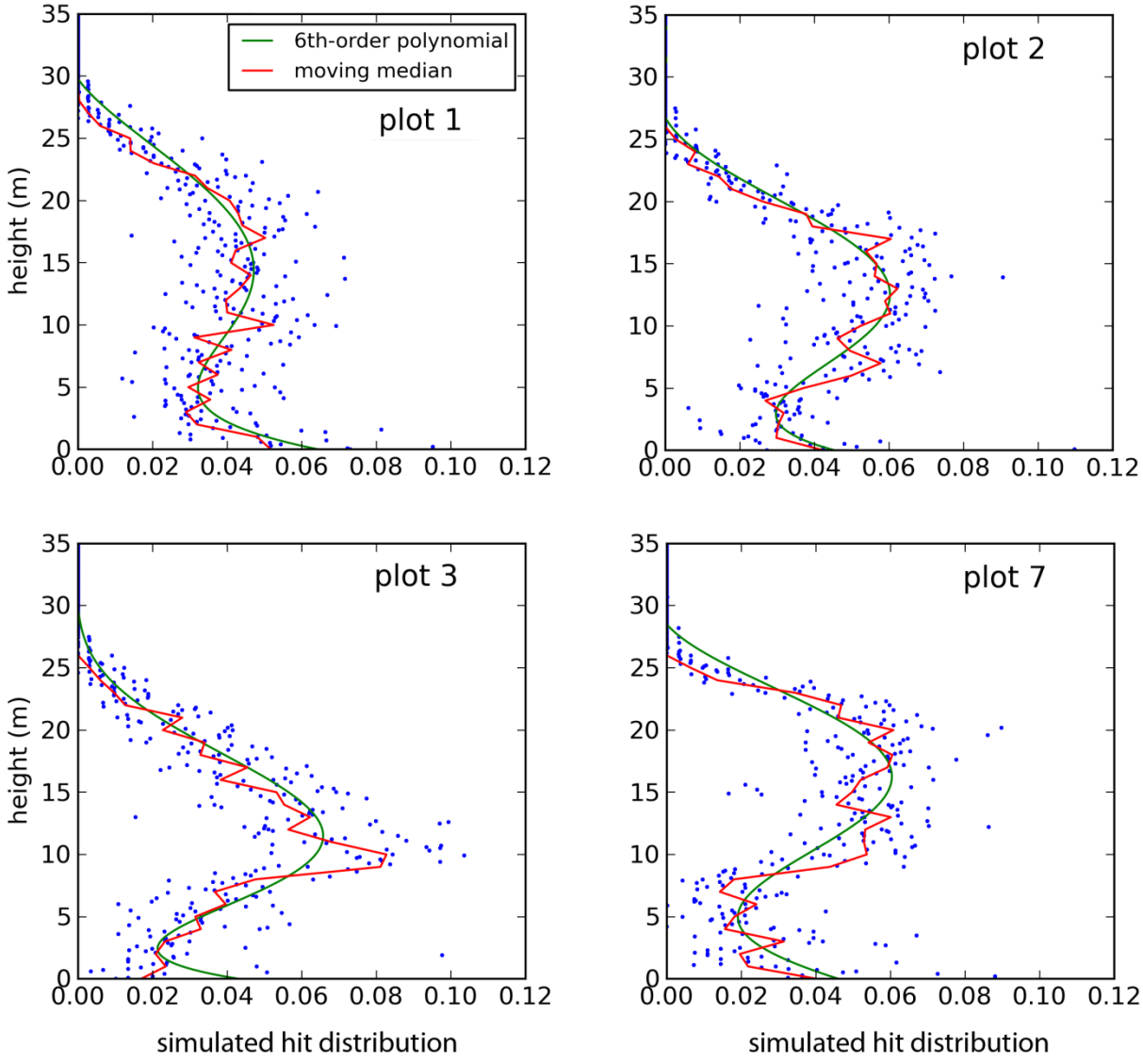

Figure 3.12: Hit distributions for the four plot reconstructions and fitted trend lines. The profiles show an increase in the mid canopy and an increase near the forest floor, and considerable variation in absorption around the trend lines.

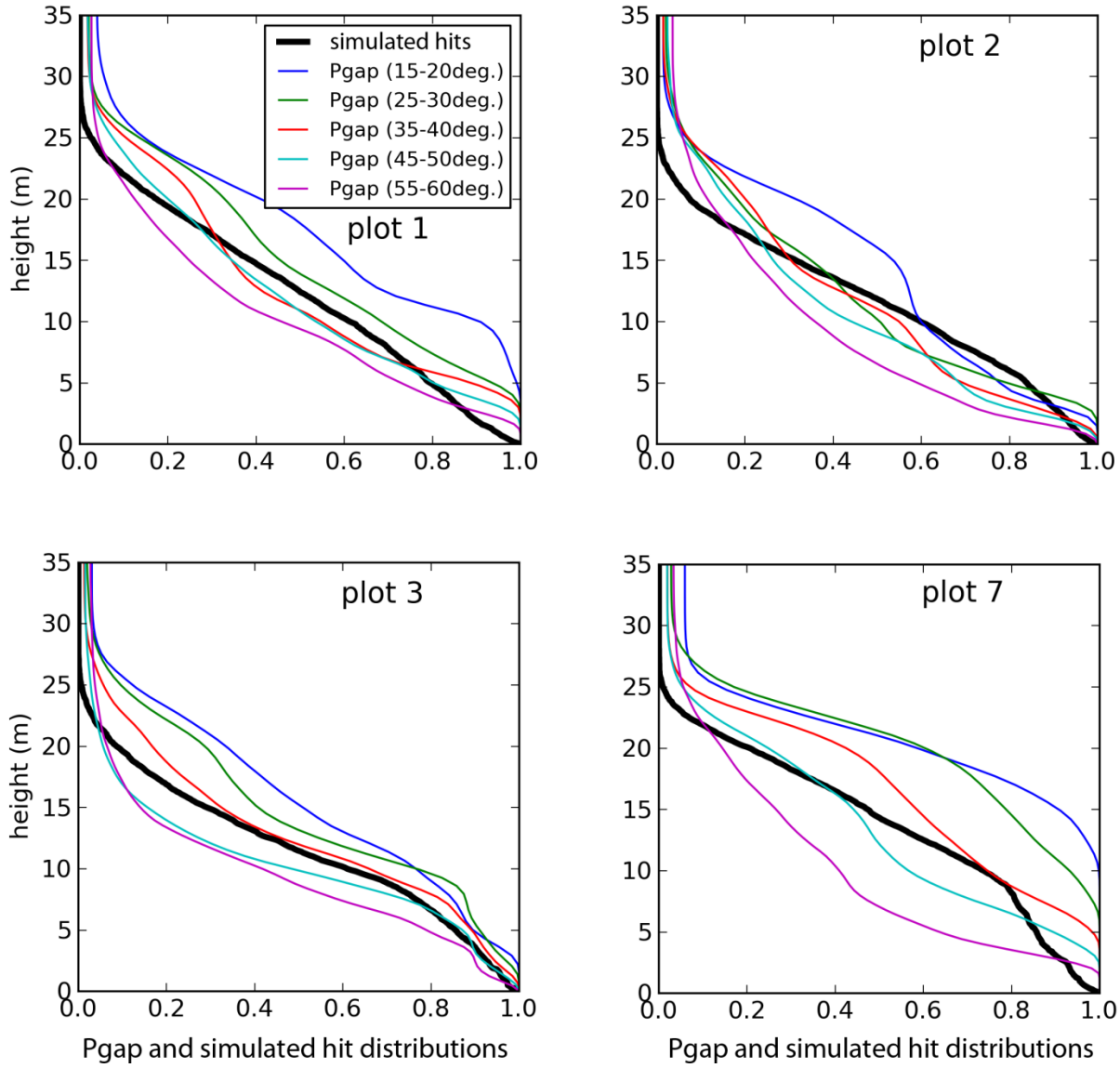

Figure 3.13: Cumulative hit distribution against EVI P_{gap} measured around different zenith angles.

3.4. Discussion and conclusions

3.4.1. Stem detection

The presented method for stem detection provided accurate results in a highly computationally efficient approach and provides an alternative solution to circle-fitting approaches (Maas et al. 2008) with a comparative advantage for lower resolution data sets (e.g. 0.25° angular resolution) or the detection of thinner stems from high resolution data (see figure 3.15 for a demonstration of how the filtering criteria for stem detection are applied to more recently acquired ground-based laser scanning data from a high-resolution Leica C10 data set comprising nearly 10 million first returns of a Eucalypt stand, provided by Dr. Glenn Newnham, CSIRO, 2012). Future research will also apply stem detection to deciduous species with more complex branching structures. A current concern is that the 3x3 kernel test effectively erodes the width of the trunk that has important impacts on diameter retrieval, which may be mitigated through incorporating other algorithms such as connected component labeling that preserved contours in the segmented image. Stem detection was insensitive to the parameter ξ for a large number of scans, hence reproduction over a range of forest types may reveal if this parameter could be omitted. In addition, the currently used univariate normalized correlation coefficient, r, may be substituted for a bivariate correlation coefficient to evaluate the correlation between stem edges along the image x and y axes.

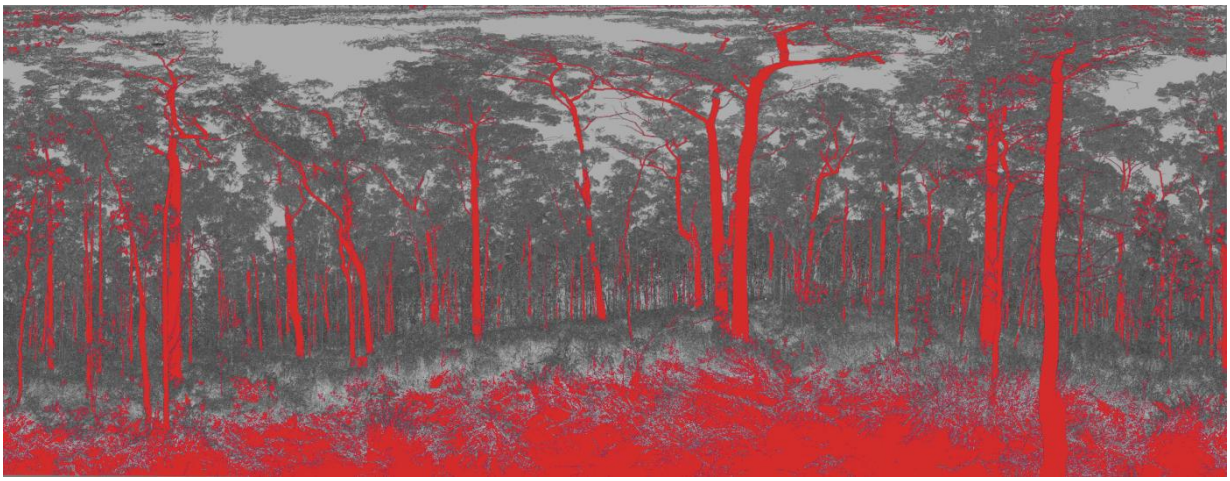

Figure 3.14: Illustration of the application of stem detection (red) methods on high-resolution Leica C10 data (greys) of a Eucalypt stand, Australia (data provided by Dr. Glenn Newnham).

3.4.2. Mesh modeling

Architectural tree modeling software has predominantly been used within the fields of computer graphics and visualization and only more recently in remote sensing and image processing (Côté et al. 2009; Widlowski et al. 2007). Challenges in adopting these models in remote sensing largely relate to the parameterization that is geared towards graphical display rather than physiological functioning (see also table 3.1 for a comparison). Arbaro provides for the modeling of a large variety of tree species from coniferous to broadleaved trees and grasses through a common set of variables. A modification of Abraro was used in this study with an emphasis on physiological functioning and radiation transfer by modeling branches as planar polygons that possess the average radiation attributes derived from field observations. The model parameterizations required default settings that were considered species-specific, and effects of stocking density and age on the radiative characteristics of the foliage needs to be further investigated. The current implementation is of a modular form that allows substitution of field observations with laser derived geometrical attributes. For example, shoot-level structure acquired through laser scanning of shoot samples can be included in the canopy representation as attribute data or can be used to substitute the planar polygons entirely, for example for establishing benchmark scenes for model inter-comparison (Widlowski et al. 2008).

Table 3.1: Comparison of terminology and variables typically used in forest mensuration and ecology vs. related parameters used in architectural tree models.

forest mensuration/ecology	architectural tree models
clumping factor	distributions of 1st, 2nd and 3rd order branches
leaf area	number of leaves per branch
foliage profile	crown shape
diameter derived from pipe model	ratio branch width to length or branch order

The abstraction of crown architecture to meet computation power and functional representation is a key challenge that needs to be addressed in forming radiative transfer models that need to be operated over considerable spatial scales or where extensive analysis of parameter sensitivity is required using conventional computer hardware. The current choice of using planar polygons closely resembles the organization of foliage into layers that has been frequently used for modeling radiative transfer (Ross & Marshak 1991); however, other abstractions such as shoot cylinders (Oker-Blom et al. 1991) or convex volumes of foliage (Strahler & Jupp 1991) could be applied to pine or a broad variety of deciduous species. Abstracting the actual crown morphology introduces, however, model parameters that are effective in describing canopy radiation (e.g. Asrar & Myneni 1991), yet their actual real-life meaning is lost. An example of such a parameter is the effective LAI that provides for the application of Beer's Law to clumped canopies, but its value does not equal the real canopy LAI. The current processing pipeline attempts to address concerns around the use of effective parameters by avoiding them where possible and adopting easy-to-measure forest inventory parameters relating to stem and crown dimensions and architecture.

While of less importance in radiative transfer modeling, stem locations form a significant aspect in the current automation pipeline (Côté et al. 2009) as stems are used to segment the plot into individual tree growing spaces and constrain the distribution of foliage elements. It is anticipated that the presented modeling pipeline works equally for other species that have a monopodial trunk. For species with trunks that split into different directions, a similar processing pipeline can be envisioned where growing spaces are derived around the individual stems and branches and scaling of the tree regenerations revolves around these individual growing spaces. For these cases, a similar ordering of parameter sensitivities as listed in Figure A.1. (Appendix A.1.2.) may be expected in that lower order stems have greater influence on the radiation profile, yet further research is needed to confirm these assumptions. Future studies may also investigate the use of tree (stem) vigor and dominance as weighing criteria in defining growing spaces, as well as adaptation of foliage densities and biophysical properties to the modeled radiation regime (Côté et al. 2011).

3.4.3. Radiative transmission

This Chapter presents a reconstruction method with which 3D-explicit models were derived from a point cloud of a coastal Douglas fir forest. From these models, the range to first hit for a given irradiation geometry can be studied and compared with full waveform derived P_{gap} measurements (Jupp et al. 2009). A widely accepted theory on radiation transmission in forest canopies is based on Beer's law that prescribes the exponential decrease in radiation with canopy depth and assumes a random distribution of foliage material and a homogeneous layering of foliage. Under these assumptions, P_{gap} profiles show an exponential decrease with the optical depth of the canopy and this principle is also observed in our model simulations. At spatially finer scales large deviations from Beer's law are expected (e.g. De Pury & Farquhar 1997) which is also observed in our model. Yet, how well the current model represents the fine spatial radiation patterns of the real forest canopy could not be assessed with the current data set.

The EVI P_{gap} profiles corresponding to larger zenith angles show a convex shape owing to the increase in path length and reflect that information about canopy structure enclosed in the EVI data is biased towards lower canopy strata (Hilker et al. 2010b). Too small a zenith angle is prohibitive, however, as the occurrence of canopy gaps is biased towards the zenith (Yang et al. 2010). It is thus assumed that the range of zenith angles used in this study provides a level of confidence around the true plot-level P_{gap}. Figure 3.12 shows that P_{gap} approaches values close to zero towards the canopy top. This is due to the stand reaching canopy closure and for more open canopies the values of P_{gap} may be much larger (Yang et al. 2010). All plots show a strong similarity in P_{gap} profiles which indicates the homogeneity of the stand. A maximum in the hit distribution can be observed for heights around 15 m, as well as a ground peak that contributes to around 5 to 10% of total incident radiation. Plot 7 shows the fastest increase in hit distribution with canopy depth, albeit subtle, which may be explained from its nitrogen enrichment.

Validation of our mesh reconstruction was achieved against the EVI P_{gap} profiles and results indicate strong correlations between the hit distributions derived from the mesh reconstructions and full-waveform P_{gap} profiles. For a correct interpretation of these results, the differences between the P_{gap} and hit distributions should be considered, however. The main difference between our simulation and EVI P_{gap} is the geometry of illumination; while the ray tracing simulations illuminate from the top of the canopy downward, the EVI data is collected from a below-canopy perspective. Although simulations could use the identical illumination geometry as the EVI, this was not done for two reasons: 1) The

current processing pipeline is limited in modeling the bottom of forest canopies, and for simulations with a below-canopy perspective the parts of the canopy closer to the instrument set-up would have a greater influence on the modeling results. 2) Moreover, from a physiological perspective it is more interesting to simulate irradiance from the top of canopy downwards as the largest contribution to forest productivity is provided by higher canopy strata. The difference in illumination geometry may be resolved through the use of tower-based scanning instruments (Eitel et al. 2013).

Future research should primarily address the tuning of parameter values to a range of forest types, species and age compositions, as well as resolving scaling issues and transfer of the presented method to other instruments. The limited size of the current research plot introduces edge affects that impact the hit distributions in that larger portions of radiation are received at lower heights compared to what would have been absorbed if the plot was not isolated from its environment. These edge effects need to be addressed through acquisition of laser-scanning data over larger areas (e.g. 100 x 100 m) or by using subsamples of extensive wall-to-wall airborne LiDAR data sets. In addition, results of the current study are simulated at plot level, although computations include approximations at a much finer scale. Future work will examine the three-dimensional consistency of radiative transfer at around a $1m^3$ scale against an *in situ* sensor network that captures diurnal as well as seasonal changes in canopy radiation and narrow-waveband data that relate to the efficiency of solar energy capture (Garrity et al. 2010). Future research is also needed to investigate the influence of stocking density, crown dimensions and foliage distributions, including clumping, on the evolution of the canopy radiation regime with stand development and its implications for forest growth and management.

4. Estimating the distribution of photosynthetic assimilation within the canopy volume through inversion of a geometrically explicit canopy model

4.1. Introduction

Forest productivity plays a key role in forest functioning and is a key driver in calculations of sources and sinks of CO_2. Monitoring global changes in forest productivity is also important as it is indicative of biodiversity (Coops et al. 2008) and can be used to explain how anthropogenic influences and climatic changes affect ecosystem functioning (Coops et al. 2009). Monitoring productivity is challenging, however, due to the broad extent of global forest resources, the multitude of environmental drivers, including temperature, humidity, soil moisture and nutrient status, and the lack of control over these drivers in field experiments. As a result, a wide range of forest productivity models exist that range from simple to complex, and empirical to physical, to suit a wide range of scales of operation (Hilker et al. 2008).

An empirical and widely used model is the Monteith model (Monteith 1972, 1977) that describes gross primary productivity (GPP; also referred to as gross ecosystem photosynthesis, GEP) as a function of incident or absorbed photosynthetic active radiation (IPAR and APAR, respectively) and the efficiency with which this light energy can be converted into photosynthate, known as the light use efficiency (LUE). When water and nutrient resources are abundant, and photosynthesis is limited by light, LUE reaches a maximum and GPP increases first linearly with increasing light levels. When resources other than light are limiting photosynthesis, LUE decreases so that GPP forms a hyperbolic relationship with PAR (i.e. incident or absorbed). While being a simple concept, LUE describes the net effect of a wide range of physiological mechanisms and much research has been conducted on the determination of its value for a range of environmental conditions (Hall et al. 2012; Heinsch et al. 2003; Hilker et al. 2012b; Mäkelä et al. 2008). At the stand level, the use of the model has heavily relied on the eddy-covariance (EC) method that estimates GPP from CO_2 fluxes, derived from high-frequency measurements of wind vector components and CO_2 and H_2O mixing ratios (Baldocchi et al. 2001). To estimate GPP at regional to global scales, studies combined remote sensing data with estimates of temperature and vapour pressure deficit to model the down-regulation of optimal, biome-specific LUE values (Heinsch et al. 2003). More recent research has focused on the remote observation of changes to

the physiological mechanisms underlying LUE directly, such as the ability of xanthophyll pigments to dissipate excess light when photosynthetic capacities are reached (Demmig-Adams & Adams 2006; Gamon et al. 1992; Hall et al. 2012; Hilker et al. 2012a). Over the last two decades, the integration of LUE models with remote sensing data has provided for scaling productivity estimates to regional and global scales cost efficiently and rapidly, however, airborne and spaceborne data primarily capture the state of photosynthesis along the top of canopy (TOC) and it remains uncertain how variations in LUE with canopy depth affect the overall GPP. While proximal sensing techniques provide for measurements of down-regulation for arbitrary locations within the canopy (Gamon & Bond 2013), scaling these measurements across the landscape is challenging (Gerstl & Borel 1992; Timmermans et al. 2013).

Radiative transfer models describe scattering of light inside the canopy to derive a distribution of PAR and temperature at the leaf-level. These radiative transfer models can be coupled with a leaf-level photosynthesis model from which forest productivity is computed by integrating leaf-level assimilation over canopy depth. Examples include some fine-scale models such as MAESTRO and MAESPA (Medlyn et al. 2002; Wang & Jarvis 1990) and BIOMASS (McMurtrie et al. 1990). In these models, individual tree crowns are represented using simple geometric primitives such as cones and spheroids with spatial distributions of leaf densities and orientation angles assigned and derived from field observations. These physical models provide an important means to integrate physiological mensuration data at the leaf or shoot level as well as stand level with data assimilation (Luo et al. 2001). However, these models require a large number of physiological parameters that are often not available across larger areas. To be used at landscape levels, radiative transfer models need to be sufficiently simple to provide for model inversion given a set of reflectance data (Jacquemoud et al. 1995) and, as a results, the potential to include physiological mechanisms in those models is largely unexplored (Widlowski 2010).

Semi-empirical models provide a compromise between the complexity of physical models and the simplicity of empirical models and provide a means to include plant physiology in radiative transfer models that are relevant to remote sensing. Barton & North (2001) demonstrated the use of a semi-empirical model to derive vertical profiles of LUE based on a 1D radiative transfer model and a single, hyperbolic leaf photosynthesis model. The down-regulation of photosynthesis by the xanthophyll cycle was then simulated using incident, leaf-level PAR and this was used to compute a TOC PRI signal. However, novel models are needed that encompass scales ranging from the shoot to stand level that inevitably need to be 3D in nature to resemble the discrete and heterogeneous nature of canopies.

Laser scanning is a recent technology that provides for the remote measure of three-dimensional structure and intensity information of surface geometries. These scanners record the time difference between emission and detection of laser pulses. The data may be represented as point cloud data that comprise a sampling of target surface coordinates or as full-waveform data that comprise a recording of returned light energy over time (e.g. at a nanosecond time step). Earlier work has demonstrated the use of point cloud data from ground-based scanners for constructing geometrically explicit forest models (Bucksch et al. 2010; Côté et al. 2009; Raumonen et al. 2013; Van der Zande et al. 2011; Van Leeuwen et al. 2013) that typically involves the reconstruction of trunks and branching topology combined with tree-regeneration methods to provide for the modeling of branching structures in regions where the sensor field of view is obscured or point densities are low. Jupp et al. (2009) demonstrated the use of full-waveform laser scanning to derive hit and gap probabilities at the stand level that provide for the estimation of vertical profiles of leaf area with canopy depth and are also indicative of exposure of canopy strata to PAR (Yang et al. 2010).

The work presented herein relies on the modeling of canopy radiation transfer based on hit probability; however, rather than a derivation of hit probability at the plot or stand level, the current work uses laser scanning data to establish a 3D explicit forest scene for which shoot-level hit probabilities can be obtained using ray tracing techniques. Once established, incident shoot-level radiation is computed from meteorological records and using ambient temperature and relative humidity, photosynthetic assimilation and down-regulation are evaluated using a single, empirical leaf photosynthesis model. The parameters of the photosynthesis model are fitted using non-linear optimization against eddy-covariance estimates of GPP. Finally, potentials to augment model parameterization using proximate and airborne or spaceborne remote sensing measurements are discussed.

4.2. Methods

4.2.1. Study area

A full study area description is available in section 1.5.

4.2.2. Data

In 2008, ground-based laser scanning and airborne LiDAR data were acquired. The ground-based laser scanning data were acquired with the EVI (CSIRO) full-waveform laser scanner that emits roughly half a million laser pulses in an upward hemispherical direction and records the reflectance of this laser light at a sampling rate of 2 Gs/s so that the distance to the scattering surfaces can be determined at centimeter accuracy. By emitting pulses over a more than hemispherical field of view (i.e. 130 x 360 degrees), millions of returns are recorded per scan and a total of five scans were taken: one in the centre and one per plot corner. (This plot corresponds with plot 1 in Chapter 3.) For all analyses described in this chapter, eddy-covariance data along with meteorological records including IPAR, relative humidity and temperature were selected for the year 2009. GPP was calculated from eddy-covariance measurements of Net Ecosystem Productivity (NEP) plus respiration. Respiration estimated using nightly Net Ecosystem Exchange (NEE) measurements that were extrapolated to the daytime based on soil temperature measurements (e.g. Jassal et al. 2009).

4.2.3. Preliminary data analysis

Diffuse radiation has a lower canopy extinction coefficient in forest canopies compared to direct radiation (Norman & Jarvis 1974) hence cloudy conditions are known to lead to a distribution of radiation that is more homogeneous with canopy depth and this results in greater GPP. This difference in attenuation between diffuse and direct light causes much variation around the relationship between GPP and incident or absorbed PAR (Choudhury 2001). A preliminary investigation was conducted to examine the importance of canopy structure on the attenuation of diffuse and direct IPAR and its effect on eddy-covariance GPP. To this stage, neither canopy structure nor a vertical stratification of physiological functioning of the canopy medium was explicitly modeled. Radiation conditions were stratified by the diffuse to total PAR ratio into nine strata and for each stratum, flux tower GPP [µmol C m^{-2} s^{-1}] was plotted against total incident PAR [µmol photons m^{-2} s^{-1}]. A two-parameter rectangular hyperbolic curve of the form (Middleton et al. 2009):

$$GPP = \frac{\alpha \cdot P_{max} \cdot IPAR}{\alpha \cdot IPAR + P_{max}} \qquad \text{eq. 4.1.}$$

where α is the quantum yield and P_{max} the photosynthetic capacity of photosynthesis, was fit to the observations using the Levenberg-Marquardt (LM) technique. This optimization technique seeks to minimize a cost function that specifies the difference between modelled and expected values of a dependent variable. For this study, the cost function was: $\sum_{i=0}^{N}\left(GPP_{model,i} - GPP_{EC,i}\right)$. Given a set of initial parameter guesses, the LM technique iteratively determines the direction and magnitude of parameter adjustments needed to minimize the cost function.

4.2.4. Scene reconstruction

A 3D virtual forest scene was reconstructed using a modeling pipeline described in Chapter 3. In short, individual tree stems are detected from single scans using image segmentation and filtering criteria including the correlation in shape between segment edges and segment length. Overlapping point clouds from adjacent scans and stem segments are then co-registered and a canopy height model (CHM), a digital elevation model (DEM), and a delineation of individual crowns (Chapter 2) are obtained. Gaps due to data occlusion along the stem segments are filled using linear interpolation and the stem tips are extrapolated by tracing the local point cloud geometry (Liu et al. 2005). Using the stem information, individual tree growing spaces are derived based on Voronoi tesselation at horizontal slices of a regular interval. A template tree crown was constructed using Arbaro (Weber & Penn 1995; Chapter 3) (Figure 4.1) that models crown architecture using intuitive parameters such as branch lengths and insertion angles of child-branches in relation to their parent branches. Scaled copies of the crown template were then fitted to the virtual scenes. In contrast to skeletal tree structures produced by Arbaro, that contain a high level of structural detail (Figure 4.2a), the template tree used in this study comprised a layered series of planar polygons with specified gap fractions (15%) to represent the clumping of foliage around primary branches (Figure 4.2b). This scene was used to reduce computation cost without significantly comprising the functional representation the trees. The radiative integrity of this virtual scene was validated by comparing full-waveform-derived canopy gap probabilities (Jupp et al. 2009) and gap probabilities derived through simulation (see Chapter 3; Van Leeuwen et al. 2013).

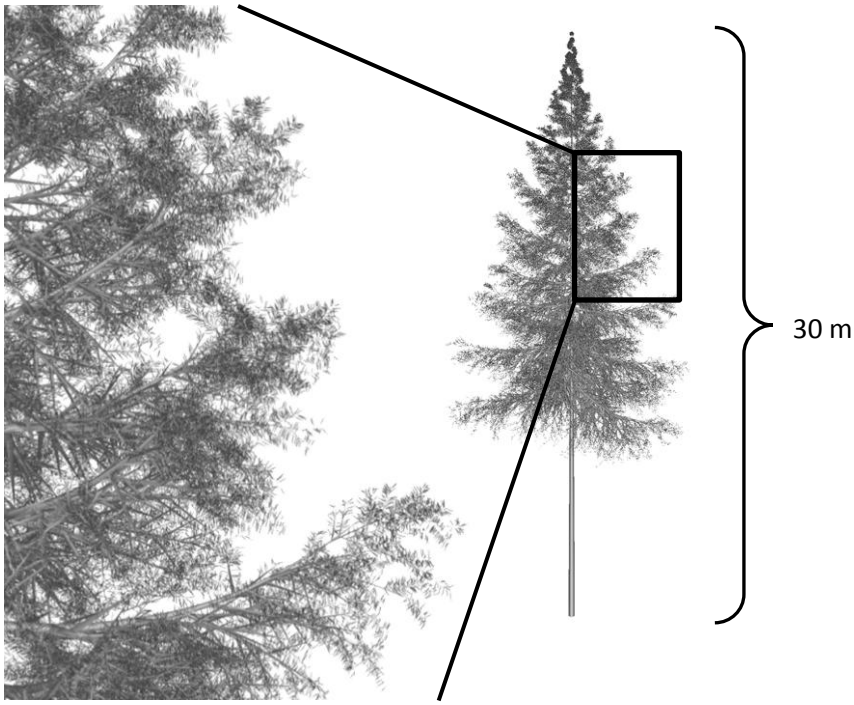

Figure 4.1: An illustration of the level of detail in Arbaro tree reconstruction methods.

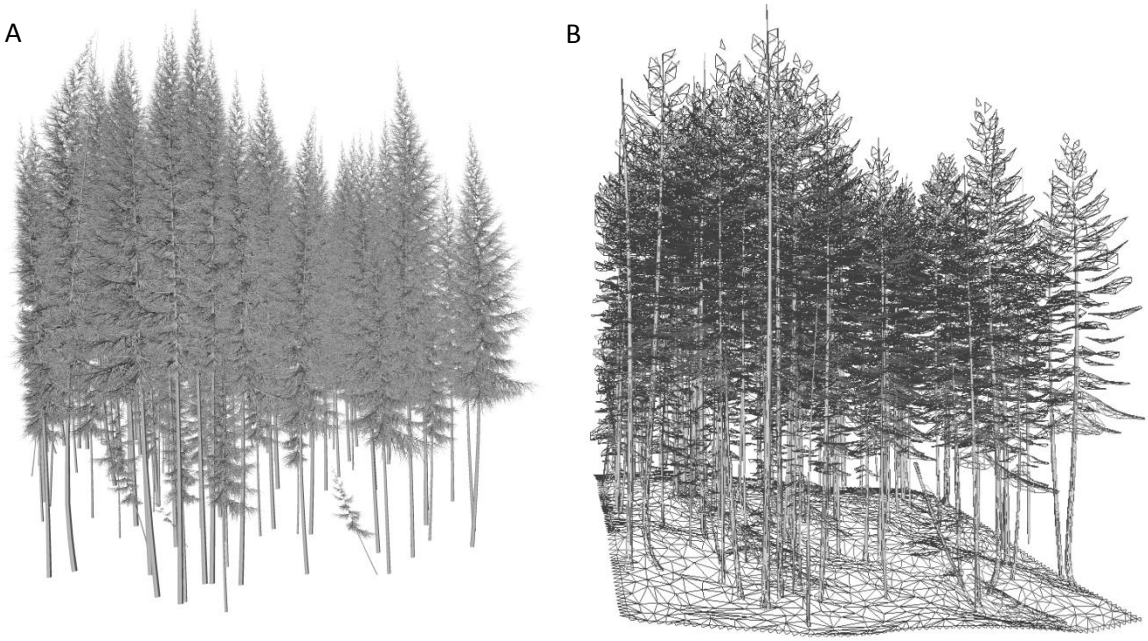

Figure 4.2: Forest plot reconstructions (DF49 plot 1) at the highest level of detail (a) and a coarser level of detail (b) where foliage clustered around branches is represented as planar polygons.

4.2.5. Canopy radiation modeling

The virtual scenes were then used to derive vertical profiles of incident PAR (IPAR) for hourly time series data. For every leaf element in the canopy the fraction of visible sky was computed using the theories of gap and hit probability that describe the probability of having a gap over a given range and from a particular location into a particular direction and the probability of a hit at a given range and direction respectively (Jupp et al. 2009). The distribution of these probabilities with canopy depth are related to the leaf area density [m^3 m^{-3}] profile and canopy radiation (Yang et al. 2010) and can be acquired from full-waveform laser scanning data (Strahler et al. 2008). Hit and gap probability are related as (Jupp et al. 2009):

$$P_{hit}(R,\theta) = -\frac{\delta P_{gap}(R,\theta)}{\delta R} \qquad \text{eq. 4.2.}$$

Earlier work (Chapter 3) demonstrated the use of a ray tracing model to obtain vertical hit distributions that were compared against full-waveform derived measures of gap probability. Every time a ray intersected with any of the scene facets, un-collided transmittance was derived from the gap fraction of the facet and the cosine of the angle between the intersecting ray and the facet normal. Ray tracers are typically used for applications where illumination and viewing conditions are fixed, however, the requirement to simulate a large number of rays to obtain a realistic distribution of canopy radiation makes the use of ray tracers challenging when illumination conditions are dynamic and updates to the radiation budgets are needed in real-time. The current study determines hit probabilities by tracing rays from the midpoints of scene facets towards upward facing hemispherical directions. This can be compared to taking a hemispherical photograph at every surface element in the scene from which portions of visible sky can be computed. This reduced form equates to:

$$IPAR(p) = \int\int P_{hit}(p,\phi,\theta) \cdot L(\phi,\theta) \cdot cos(\theta,p) \cdot sin(\theta)\, d\theta d\phi \qquad \text{eq. 4.3.}$$

where P_{hit} is the probability of receiving an un-collided ray from direction (ϕ, θ) by canopy element p (see Appendix A.4. for additional explanations), and $cos(\theta, p)$ is a notation to indicate the cosine between the normal vector of facet p and the incident ray. The model accounts for the porosity of foliage clustered around branches; however, the model only considers un-collided radiation and does not consider multiple scattering that only has a marginal effect on photosynthesis (Gobron et al. 2006).

Calculating equation 4.3 can be achieved numerically using a fixed angular step width in both azimuth and zenith directions; however, this results in a denser sampling towards the zenith. In this study, samples where distributed about a vertical axis so that the distance to that axis decreased exponentially with the sample's rank and the angular distance between samples was approximately constant (Piccini et al. 2011). To avoid edge effects for the small study plot, cyclic boundaries were applied so that a ray escaping the scene through any of the four lateral boundaries would re-enter from the opposite side of the scene.

Half hourly radiances [µmol photons m^{-2} s^{-1} sr^{-1}] were computed from diffuse and total PAR sensors mounted on the EC fluxtower (BF2 sunshine sensor, Delta-T Devices). Diffuse radiance was assumed to be homogeneous across the hemispherical samples, and direct radiance was assigned to the hemispherical sample that was closest to the sun position that was computed using a solar calculator (See Appendix A.3. for additional details). Incident radiation at the leaf level [µmol photon m^{-2} s^{-1}] was computed for every second half hour time step between 7 AM and 6 PM, for the majority of the growing season between May 1 and September 17, 2009. It was found that in simulating hit probabilities, the systematic sampling of facet midpoints resulted in some positive bias that leads to a slight overestimate of facet-level IPAR (see Appendix A.4. for details).

4.2.6. Photosynthesis modeling

A leaf-level photosynthesis model was developed based on a non-rectangular hyperbola, following Cannell and Thornley (1998). This model is parameterized by photosynthetic capacity (P_{max}) that defines the hyperbola's asymptote, the quantum yield (α) that defines the initial slope of the hyperbola when photosynthesis is electron transport limited, and the duration of the initial linear response (χ). The value for χ is generally larger for cells than for leaves and larger for leaves than for canopies (e.g. Cannell & Thornley 1998), which is caused by averaging of PAR within the canopy and the non-linear response of

photosynthesis to irradiance. The three-parameter non-rectangular hyperbola has the form (e.g. Cannell & Thornley 1998):

$$P(P_{max}, \alpha, \chi) = \frac{\alpha \cdot IPAR + P_{max} - \sqrt{(\alpha \cdot IPAR + P_{max})^2 - (4 \cdot \chi \cdot \alpha \cdot IPAR \cdot P_{max})}}{2 \cdot \chi} \qquad \text{eq. 4.4.}$$

Down-regulation of photosynthesis is expected when the leaf is light saturated and when photosynthesis is limited, for example, by water availability or when the carboxylation rate of the Calvin cycle due to temperature or nutrient supplies is suboptimal. This down-regulation was included in the photosynthesis model using modifier functions based on temperature (T in °C) and relative humidity (RH in %) for P_{max} in the form:

$$T_{mod}(T, T_{opt}, \beta_T) = e^{-\left(\frac{|T_{opt} - T|}{\beta_T}\right)^2} \qquad \text{eq. 4.5.}$$

$$RH_{mod}(RH, \beta_{RH}) = e^{-\left(\frac{100 - RH}{\beta_{RH}}\right)^2} \qquad \text{eq. 4.6.}$$

This bell-shape was chosen to ensure that the modifier functions were constrained within the range 0 to 1 and to reflect that photosynthesis has some tolerance around its optimum where changes in temperature and relative humidity have only a small effect. Further complications can be considered such as the asymmetry of down-regulation around the temperature optimum; however, to a first approximation, this was considered outside the scope of the current study. The down-regulation of P_{max} was modeled as the product of an optimal value, P_{opt}, for conditions when photosynthesis is not limited, and the two modifier functions:

$$P_{max} = P_{opt} \cdot T_{mod} \cdot RH_{mod} \qquad \text{eq. 4.7.}$$

Since down-regulation may be affected by the duration of drought or temperature stress, temporally-lagged temperature and relative humidity responses were derived following Jarvis et al. (2004) as follows:

$$T_{lag}(t) = (1 - \gamma_T) \cdot T(t) + \gamma_T \cdot T_{lag}(t-1) \qquad \text{eq. 4.8.}$$

where $T(t)$ represents the temperature at time t, T_{lag} the lagged response, and γ_T defines the lag ($\gamma_T \in \mathbb{R}$, 0≤ γ_T ≤1). A similar function was applied to relative humidity. The resulting leaf model has eight parameters (P_{opt}, α, χ, β_{RH}, β_T, T_{opt}, γ_T, γ_{RH}) and requires three input variables: IPAR, temperature (*T)*, and relative humidity (*RH*). Finally, physiological responses to changes in temperature and humidity have been observed over diurnal as well as seasonal time scales; hence an additional modifier $S_{mod}(\gamma_S, \beta_S)$ was constructed around mean daily temperatures T_{daily}. Stand-level GPP for a specific moment in time *t* was computed through integration over all canopy elements *n:*

$$GPP_{sim}(t) = \sum_{p=0}^{n} A_p \cdot P(P_{max}, \alpha, \chi) \qquad \text{eq. 4.9.}$$

where A_p is the area of the photosynthetic scene facets.

4.2.7. Model inversion

In forward mode, plot-level GPP is obtained by integrating leaf-level assimilation over the canopy. In inverse mode, the leaf model parameters are estimated using the eddy-covariance GPP estimates, T,

RH, T_{daily} and the simulated leaf-level IPAR. A series of model inversions was established comprising the cases where no down-regulation was included, where only T and RH down-regulation was modeled and a case where T, RH, and T_{daily} were used to estimate GPP. The model inversion was achieved numerically by minimizing the cost function that, depending on the number of down-regulation functions considered, has the form:

$$\mathrm{argmin}_{\Theta} \sum_t \left[GPP_{sim}\left(\Theta; IPAR, T, RH, T_{daily}, t\right) - GPP_{EC}(t) \right]^2 \qquad \text{eq. 4.10.}$$

where Θ is the vector of unknown parameters. A number of optimization techniques exist (Jacquemoud et al. 1995) and in this study, the Levenberg-Marquardt method was applied that minimizes the cost function iteratively and requires initial estimates of the parameter set Θ. To improve model conversion, χ was constrained to 0.9 throughout the study so that model inversion at most yielded estimates of P_{opt}, α, β_{RH}, β_T, β_S, T_{opt}, γ_T, γ_{RH}, and γ_S. Figure 4.3 provides an overview of the modeling design and embedded test functionality to assess the verisimilitude of the model and effects of model approximations.

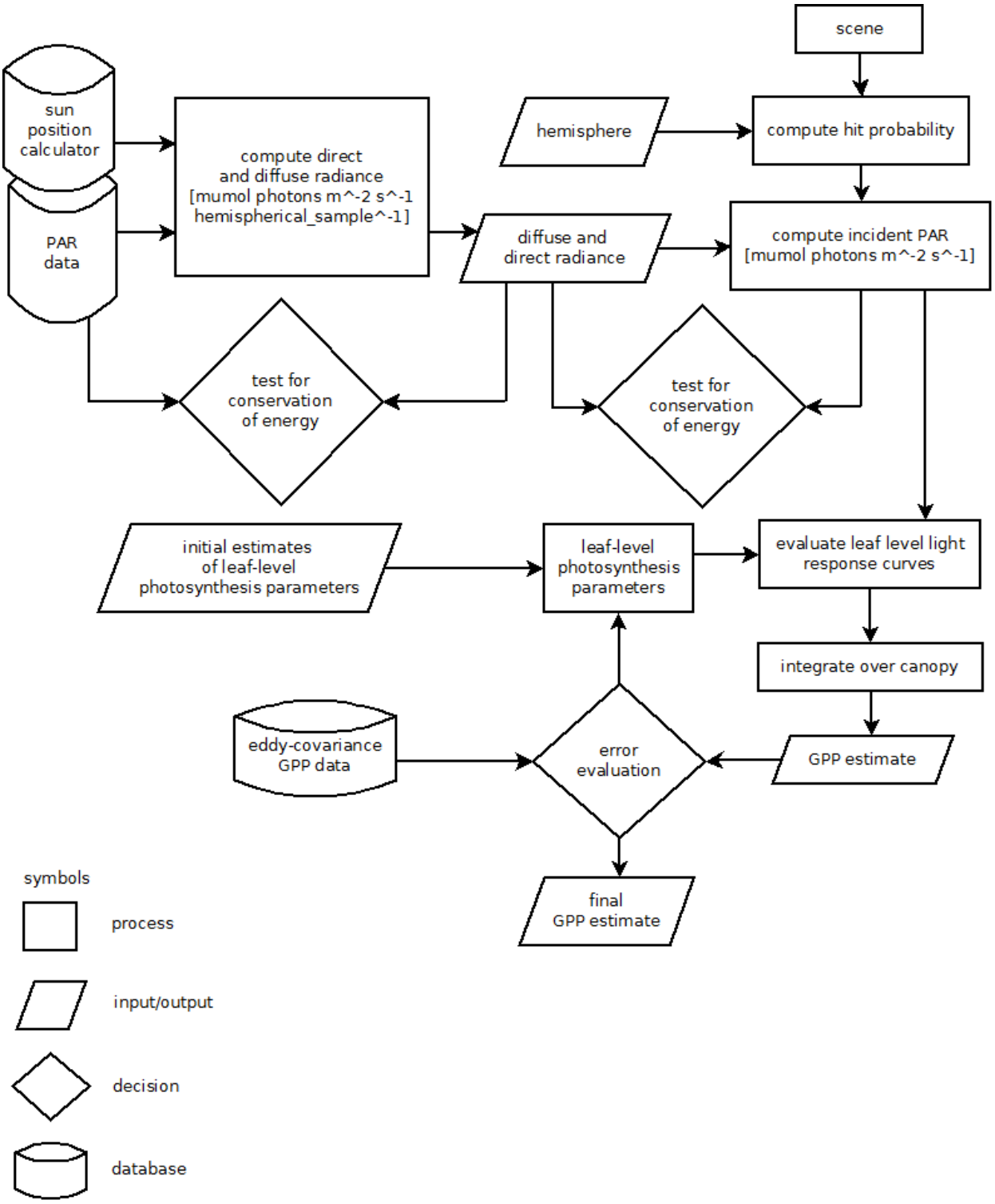

Figure 4.3: Schematic diagram of the modeling pipeline including test functions; GPP = gross primary productivity, PAR = photosynthetically active radiation, mumol is transliterated from Greek (µmol).

4.3. Results

Figure 4.4 shows the general relationship between modelled GPP and TOC IPAR for half hourly data throughout the growing season. The relationship is hyperbolic with a high degree of variation around the trend. Figure 4.5 shows the stratification of this relationship by the fraction of diffuse TOC IPAR (Q). This stratification reveals a strong linear relationship for high diffuse-fractions (bottom right panel) and weakens with increasingly direct radiation (upper left; see Table 4.1). As indicated by the large range of GPP around 1,000 µmol photons m^{-2} s^{-1}, effects of canopy structure on the internal canopy radiation regime through a differential attenuation of diffuse and direct radiation are considerable, which is consistent with observations (Norman & Jarvis 1974; Parker et al. 2004) and theory (Choudhury 2001; Norman & Jarvis 1975).

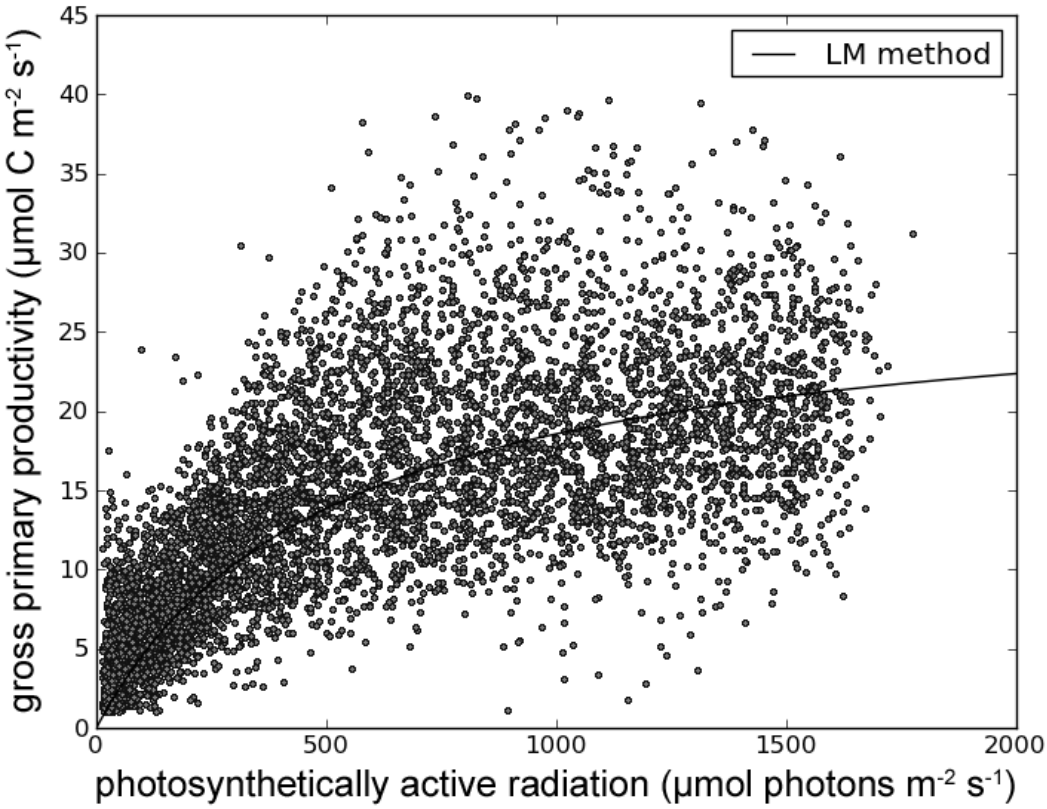

Figure 4.4: Scatter plot of eddy-covariance estimates of gross primary productivity against measured top-of-canopy incident photosynthetically active radiation at the DF49 site. The curve represents a two-parameter hyperbolic relationship that was fitted using the Levenberg-Marquardt optimization technique.

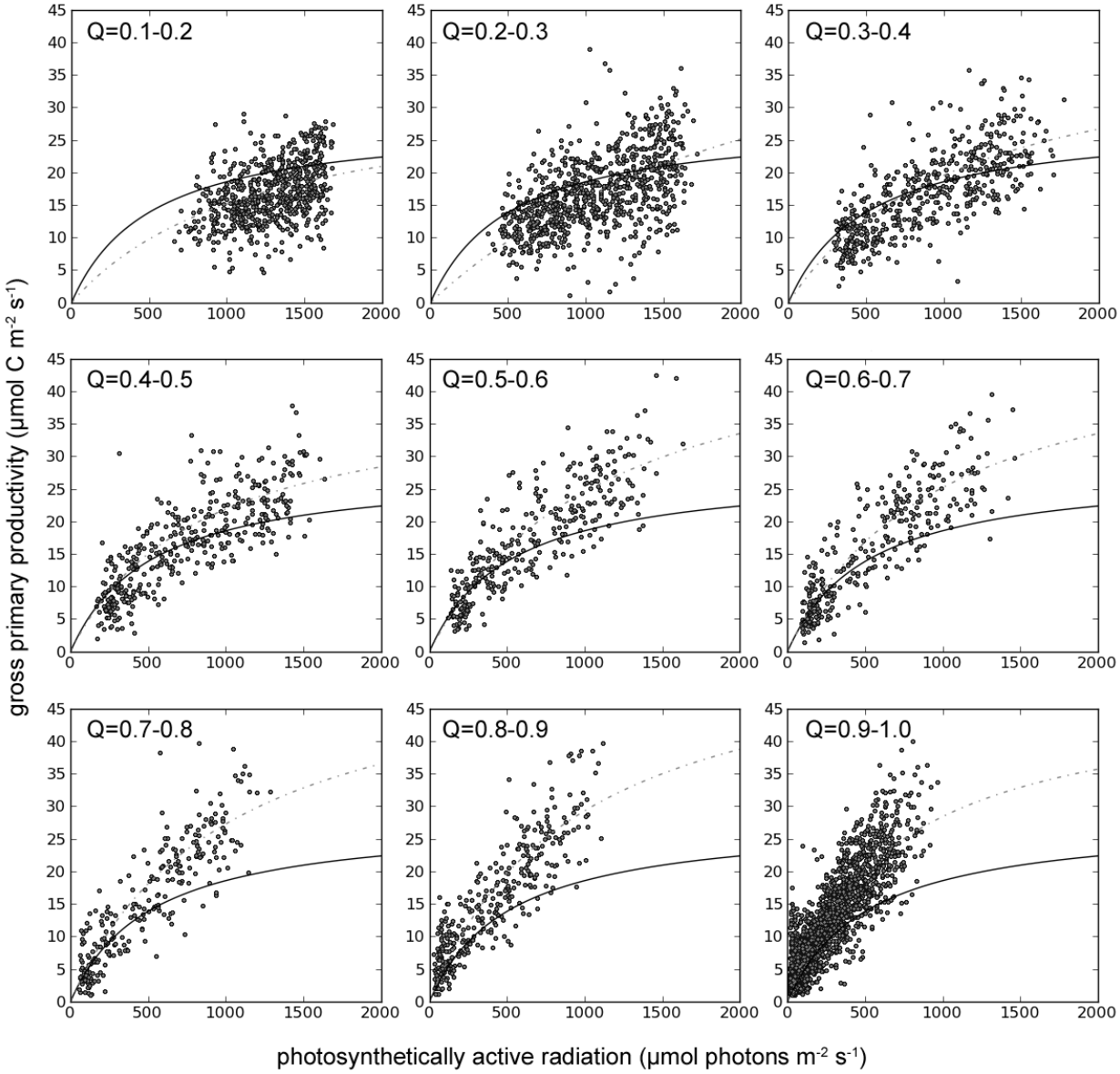

Figure 4.5: Relationships between eddy-covariance estimates of gross primary productivity, and photosynthetically active radiation incident on the top of the canopy, stratified by the fraction of diffuse to total photochemically active radiation (Q). The black lines represent the hyperbolic curve shown in Figure 4.4, while the dotted lines represent the fits to the strata. As can be observed from the graphs, under diffuse conditions the relationship between gross primary productivity and incident photosynthetically active radiation can best be described using a linear relationship.

Table 4.1: Model parameters and fit statistics for the hyperbolic relationships illustrated in Figure 4.5 (dotted lines).

Q	0.1-0.2	0.2-0.3	0.3-0.4	0.4-0.5	0.5-0.6	0.6-0.7	0.7-0.8	0.8-0.9	0.9-1.0
P_{max}	33.94	56.49	41.97	40.36	52.75	49.93	55.24	57.24	48.03
α	0.0273	0.0226	0.0365	0.0478	0.0459	0.0509	0.0538	0.06	0.0696
R^2	0.17	0.42	0.53	0.65	0.73	0.76	0.78	0.76	0.73
RMSE	4.07	2.6	4.33	4.22	4.24	4.16	4.34	4.32	3.81

The geometrically explicit model of canopy structure provided estimates of leaf-level IPAR and considers the reduced attenuation of diffuse compared to direct beam radiation by simulating radiative transfer from a large number of light sources. Figure 4.6 shows vertical profiles of within-canopy IPAR for a clear and a cloudy day in May, 2009. The graphs show a large variation in IPAR throughout the canopy and a bimodal distribution of direct and diffuse radiation. Although some bimodal distribution was anticipated, the bimodality of the simulation likely overestimates that of the real forest since the simulations did not consider multiple scattering or penumbra (Stenberg 1995a). The latter effect is caused by the size of the solar disc.

Figure 4.7a shows the Levenberg-Marquardt optimization results for the case where no downregulation due to temperature and relative humidity were considered. The figure shows a profound non-linearity and underestimate of GPP. To illustrate the behaviour of simulation results to changes in P_{max} and α, the parameters were manually adjusted (shown in Figure 4.7b). The resulting scatter has a strong linear component, however, a positive bias in GPP can also be observed, when IPAR is high under clear sky conditions. These data points correspond with higher temperature and lower relative humidity and illustrate the need for down-regulation functions. Figure 4.8 shows optimization results obtained by stratifying environmental conditions. Plots along the rows are stratified by temperature and along the columns by relative humidity. For temperature and relative humidity close to the optimum for photosynthesis, i.e. around 16 °C and relative humidity 75% to 100%, a clear linear relationship between simulated and EC-derived GPP was observed over a large range of irradiances and diffuse to direct IPAR conditions. Moving away from this environmental optimum, the relationship between simulated and measured GPP weakens and eventually becomes absent, indicated by the inability of simulations to describe the variation in EC-derived GPP for temperatures around 25 °C and relative humidity < 50%.

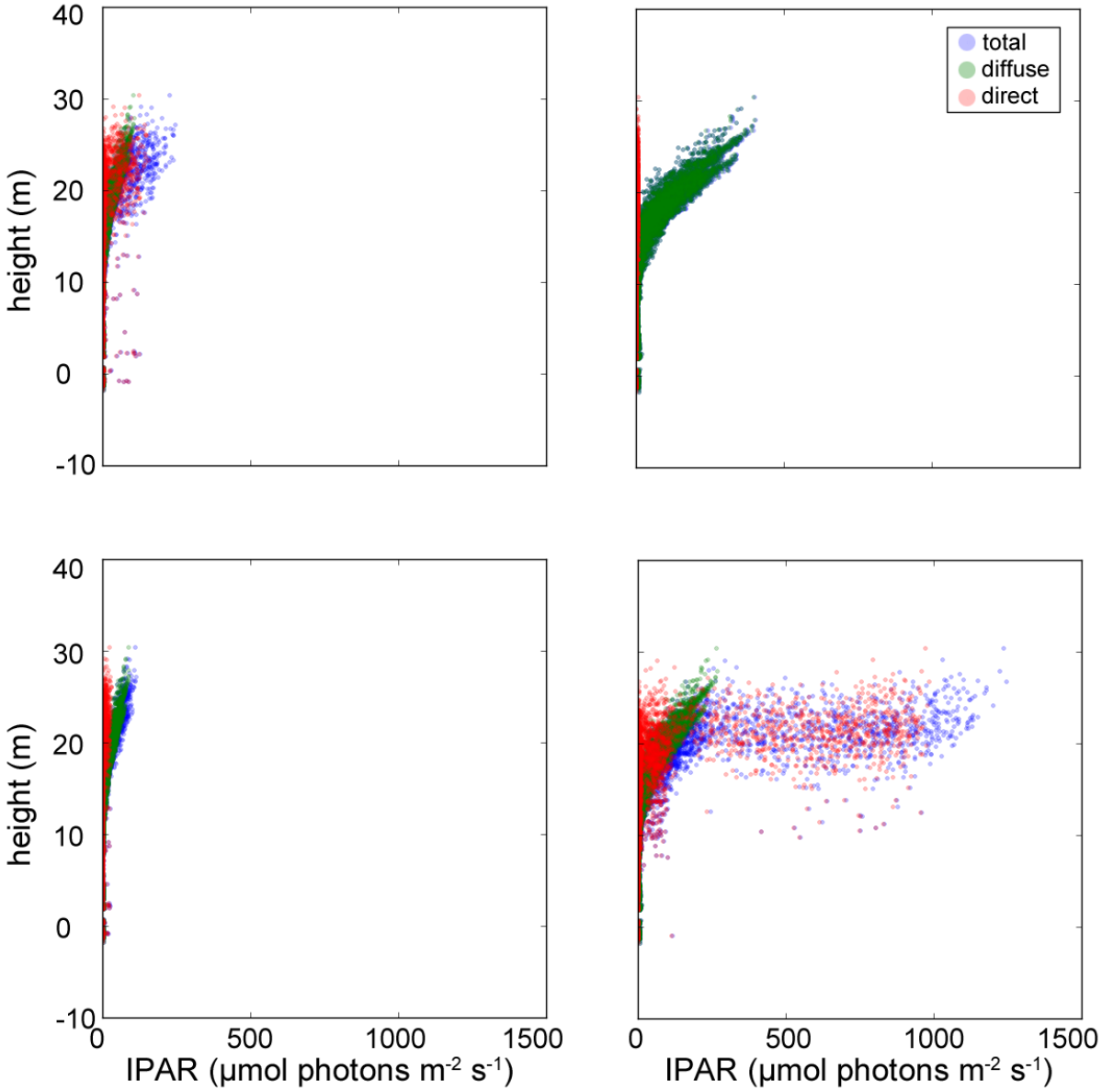

Figure 4.6: Simulation results of diffuse, direct and total IPAR for 6:00 (top left) and 13:00 (top right) on the cloudy day of May 3, 2009, and for 6:00 (bottom left) and 16:00 (bottom right) on a sunny day (May 8, 2009). Values on the x-axis show leaf-level IPAR [µmol photons m^{-2} s^{-1}] and the y-axis shows height above the scan's origin (i.e. approximately 1.3 m above ground, at the plot centre). Data points represent a subset of vegetation facets within a 3 m radius from the plot centre vertical axis.

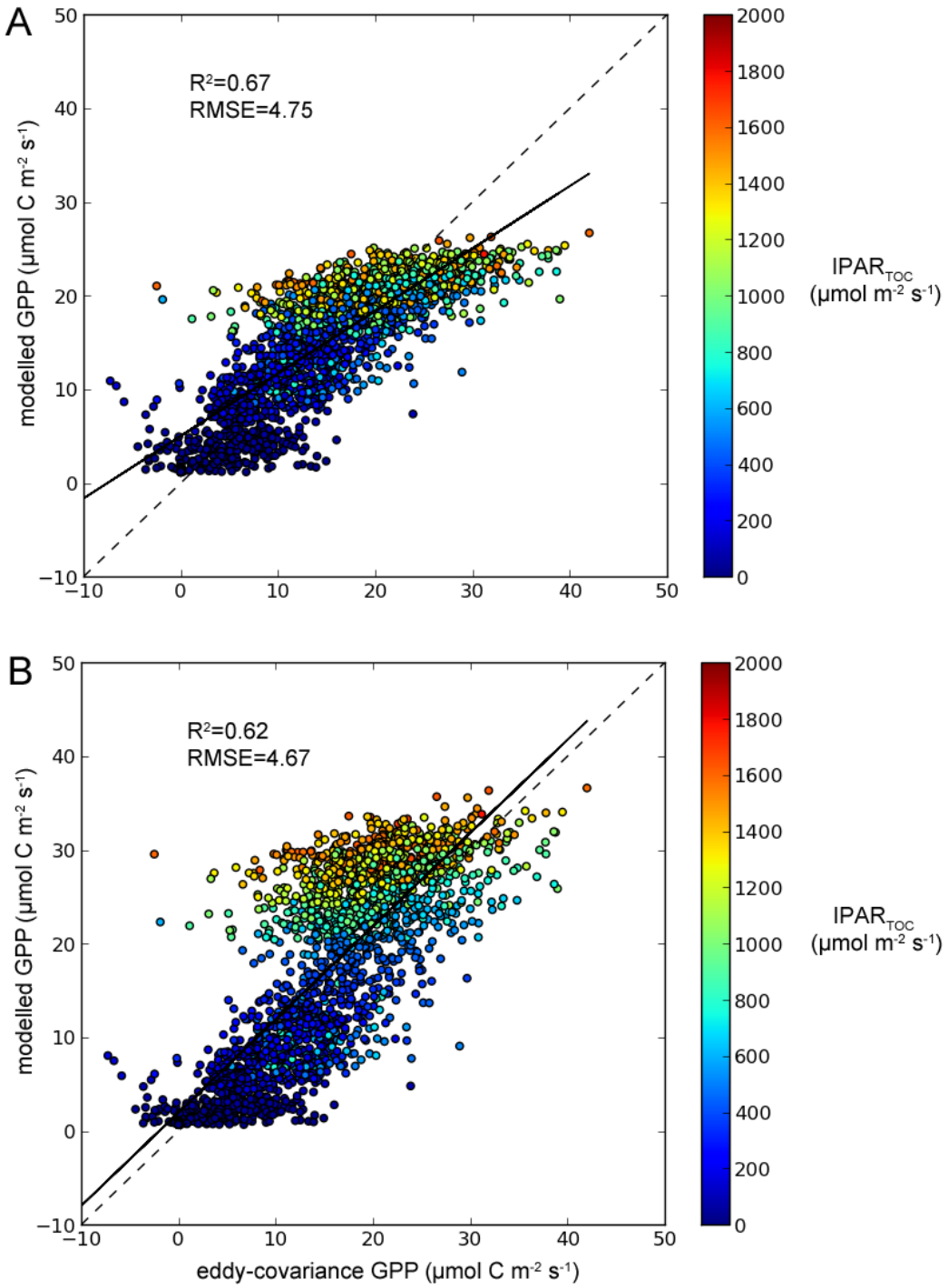

Figure 4.7: Scatter plots showing correspondence between simulated GPP and EC-derived GPP where α and P_{max} were optimized without the use of temperature and relative humidity modifiers (a; values: P_{max}= 7.31, α = 0.12); and a manual optimization of P_{max} and α demonstrating a more linear correlation among data points in low-light conditions and a large bias in high-light conditions (b; values: P_{max}= 16.0, α = 0.07).

Figure 4.9 shows the behavior of the T-modifier function as it deviates from an optimum temperature. The scaling parameter β_T controls the pace of down-regulation with distance from the optimal condition. The use of the P_{opt} modifiers based on temporally-lagged temperature and relative humidity improved the relationship between simulated and EC-derived GPP (Figure 4.10) resulting in an R^2 = 0.71 (RMSE = 4.4 µmol C m^{-2} s^{-1}); however, the Levenberg-Marquardt optimization resulted again in an apparent curvilinear relationship between simulated and EC-derived GPP.

Using the modifier functions, the photosynthetic capacity was found optimal at humid conditions (relative humidity > 75%) and at slightly higher temperatures than found for model fits without down-regulation (i.e. Figures 4.7 and 4.8). All parameters were optimized without constraining the parameters to predetermined ranges, except for χ that was fixed. While most parameters were found within realistic ranges, the quantum yield α was found outside the typical range of values reported that extends from 0.06 to 0.085 µmol C μmol^{-1} photons for IPAR and 0.09 to 0.11 µmol C μmol^{-1} photons for APAR respectively (Cannell & Thornley 1998). An additional optimization was computed where α was fixed at 0.07 µmol C μmol^{-1} photons and this resulted in a more linear relationship between simulated and measured GPP (Figure 4.11) with minor changes in the explanatory power to predict GPP.

Acclimation of the photosynthetic apparatus to seasonal patterns in temperature has been investigated in a number of studies and it has been shown that coastal Douglas-fir forests have a capacity to optimize photosynthesis over a wide range of temperatures (Hember et al. 2010). To examine the potential effect such acclimation may have on estimates of GPP, the residuals were plotted against time (Figure 4.12). This time series of residuals shows a clear pattern and indicates that GPP was underestimated for the months of June and July of 2009 (week 25 to 31). Hence, a final model run was computed where modifier functions for mean daily temperatures in addition half hourly temperatures and relative humidity were used (Figures 4.13, 4.14).

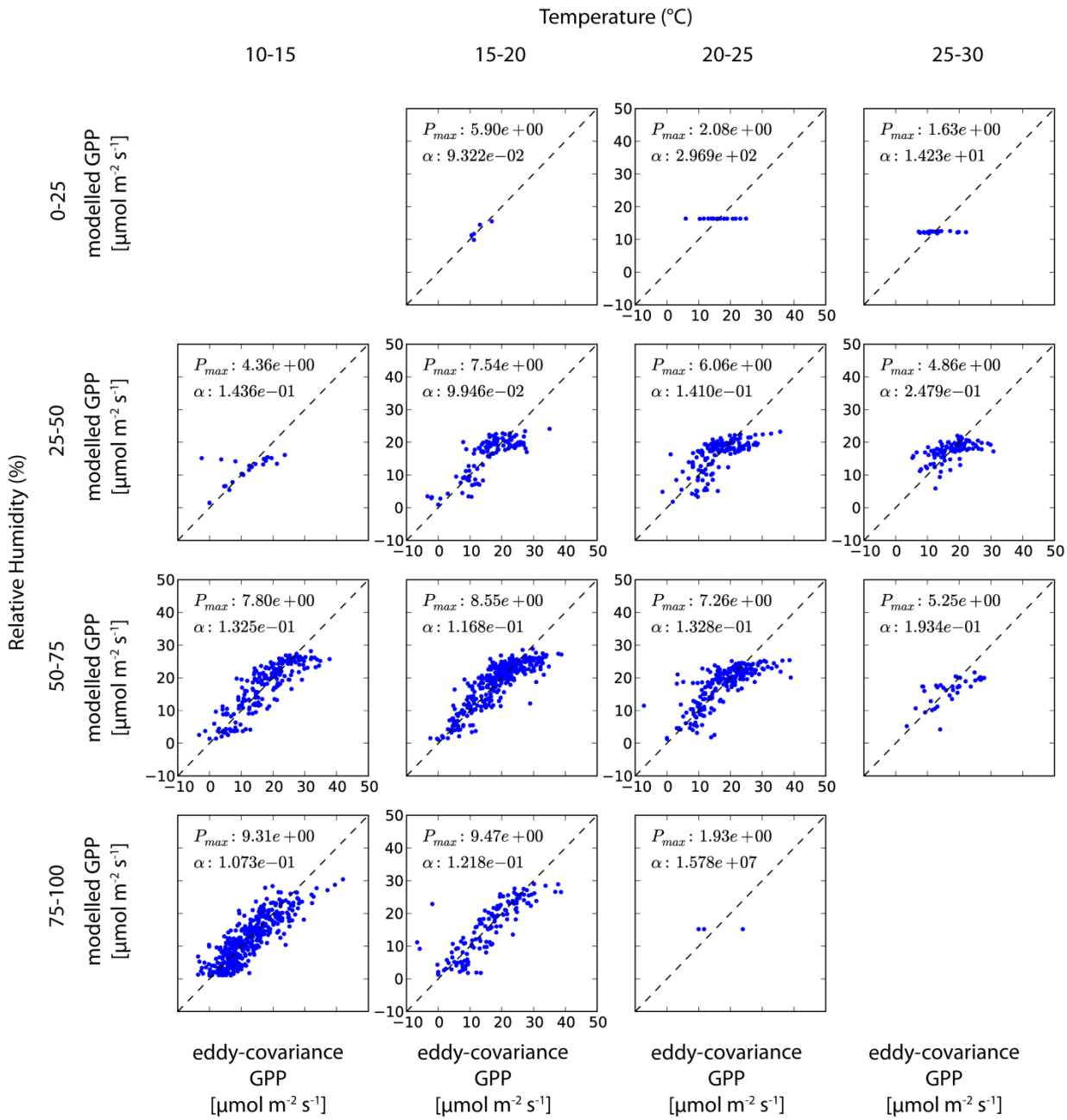

Figure 4.8: Optimization results obtained by stratifying the data set by temperature and relative humidity. The results indicate decreasing explanatory power with decreasing relative humidity and with increasing difference between T and T_{opt} (with T_{opt} within the range 10 to 20 °C).

Table 4.2: Model fit statistics for stratified meteorological data. See figure 4.8 and text for additional details.

			Temperature (°C)			
			10-15	15-20	20-25	25-30
Relative Humidty (%)	0-25	R^2		0.76	0.00	0.00
		RMSE		1.125	4.531	3.569
	25-50	R^2	0.44	0.64	0.47	0.30
		RMSE	5.384	4.205	4.688	4.629
	50-75	R^2	0.73	0.74	0.58	0.21
		RMSE	4.289	3.933	4.941	8.209
	75-100	R^2	0.73	0.71	*	
		RMSE	4.119	4.924	*	

* No statistics shown since the number of samples within stratum is N=3.

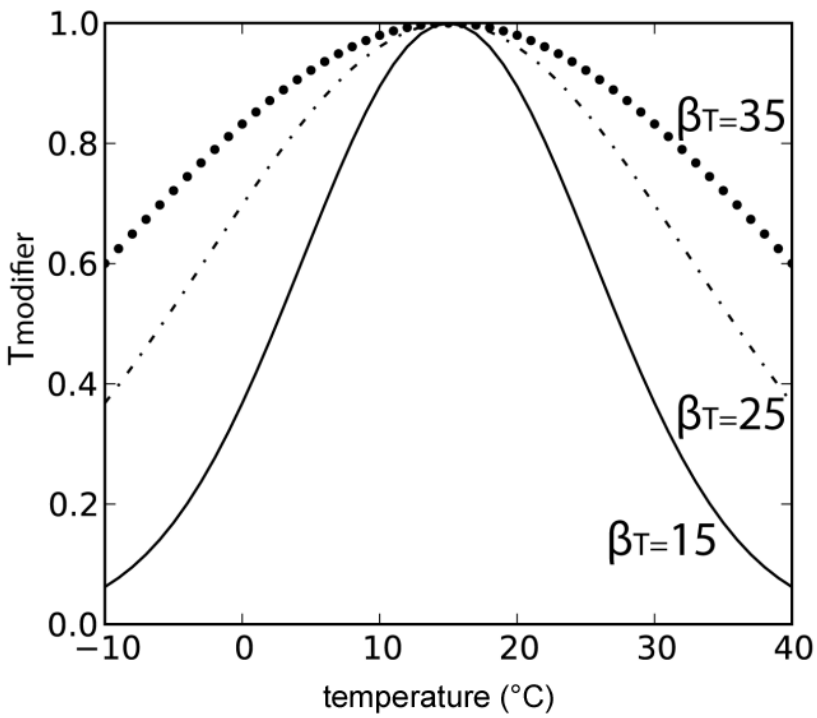

Figure 4.9: A graph illustrating the behavior of the temperature modifier function. The modifier function is a bell-shaped curve whose width increases with values for β_T and the response is constrained to the range 0 to 1 (y-axis).

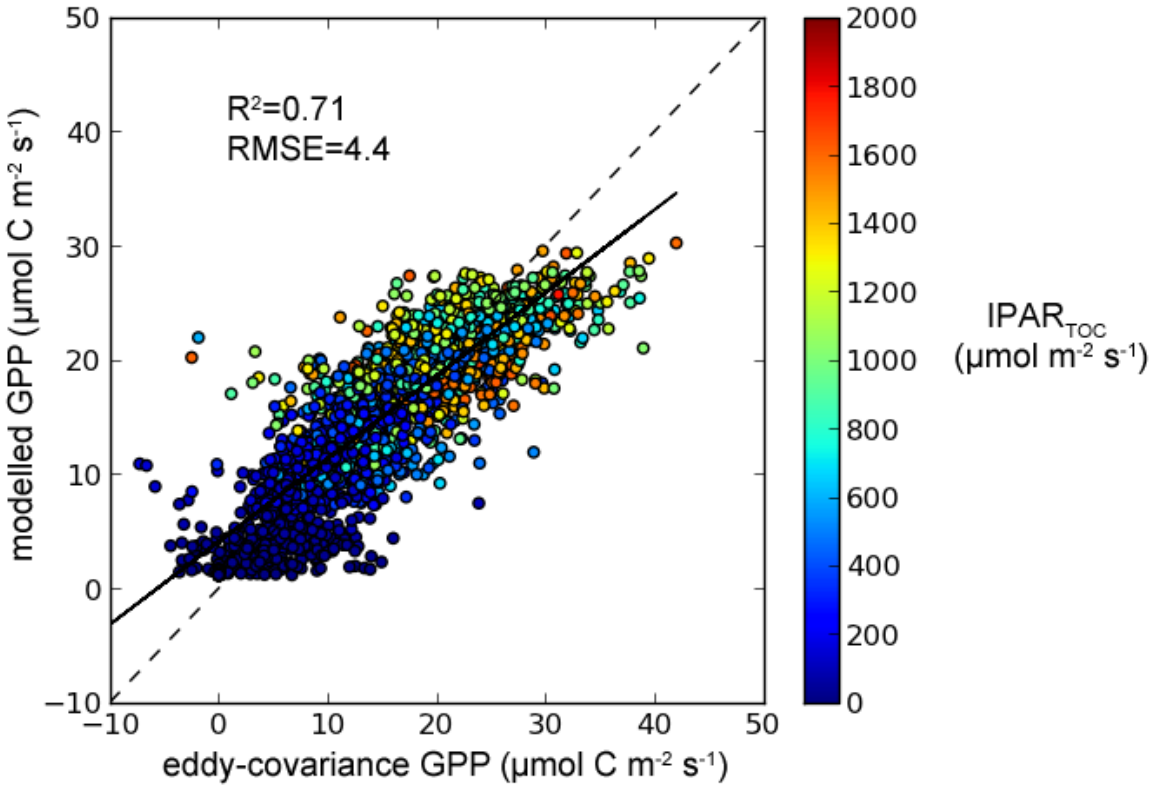

Figure 4.10: Model inversion using the Levenberg-Marquardt algorithm, and temperature and relative humidity modifiers. Colours indicate top of canopy incident photochemically active radiation [µmol photons m^{-2} s^{-1}]. Variations in eddy covariance were explained with an R^2 = 0.71 and RMSE = 4.4 µmol C m^{-2} s^{-1} (values: $P_{opt} = 11.5$, $\alpha = 0.14$, $\chi = 0.9$, $\beta_{RH} = 95$ $\beta_T = 19$, $T_{opt} = 20$, $\gamma_T = -0.24$, and $\gamma_{RH} = 0.64$).

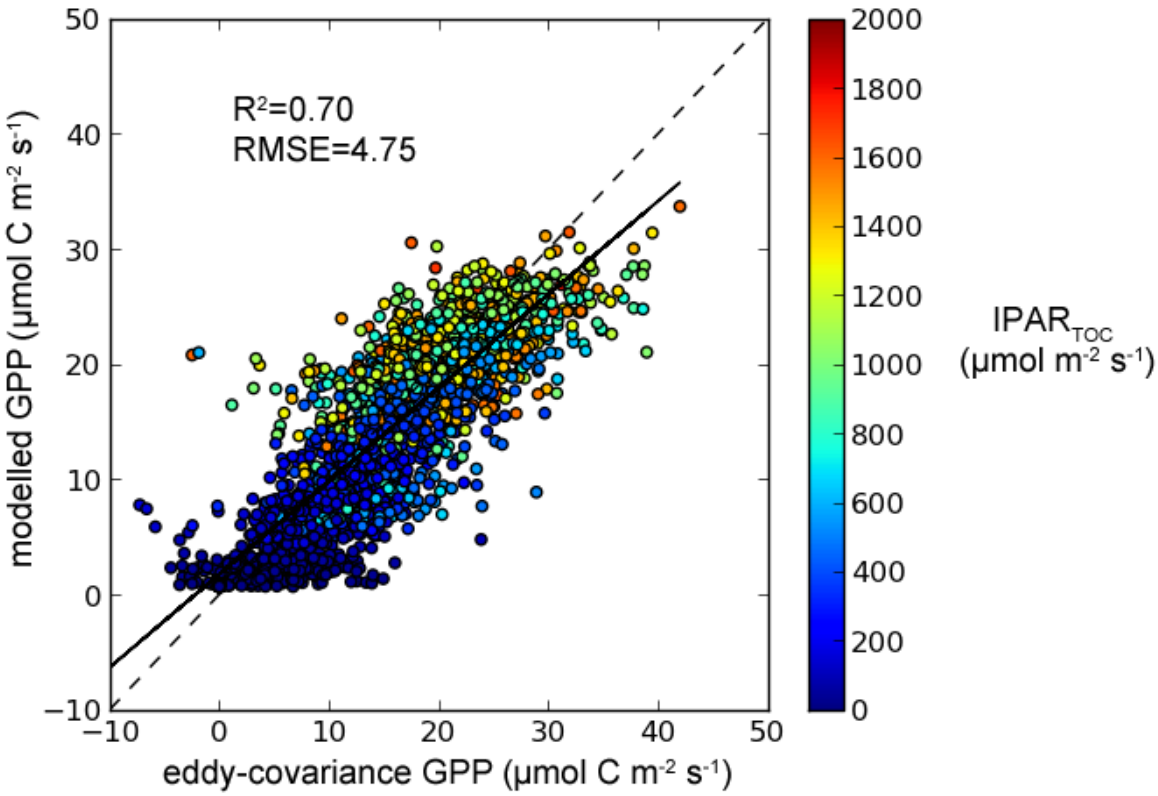

Figure 4.11: Model inversion using the Levenberg-Marquardt algorithm, and temperature and relative humidity modifiers, with quantum yield constrained (i.e. in addition to χ). Colours indicate photochemically active radiation incident on the forest canopy [μmol photons m^{-2} s^{-1}] (parameter values: $P_{opt} = 14.67$, $\alpha = 0.07$, $\chi = 0.9$, $\beta_{RH} = 86$, $\beta_T = 22.5$, $T_{opt} = 17.8$, $\gamma_T = 0.3$, and $\gamma_{RH} = 0.3$)

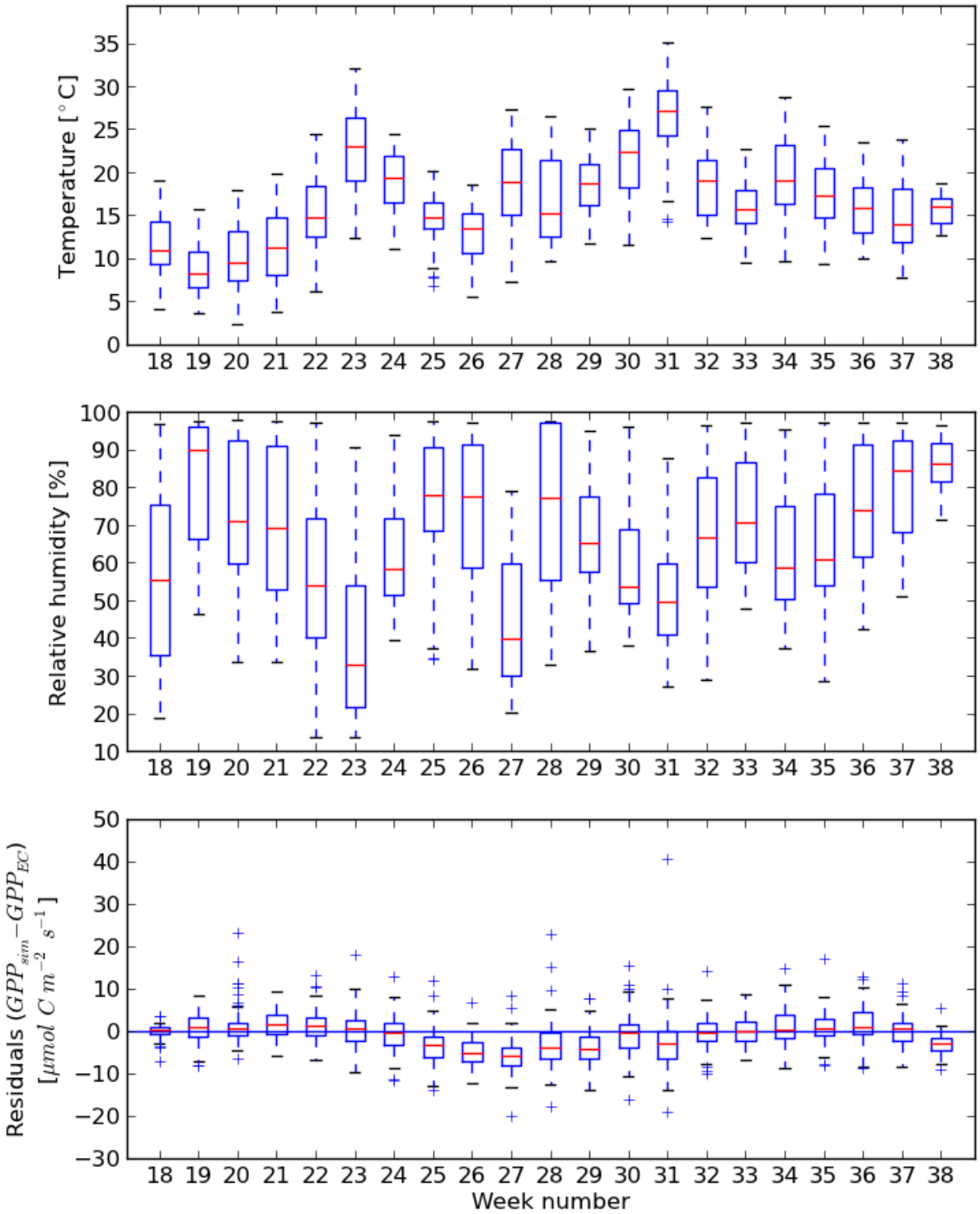

Figure 4.12: Time series box plots showing residuals between simulated and measured productivity for constrained α=0.07 µmol C µmol^{-1} photons, and for selected weeks of the year 2009.

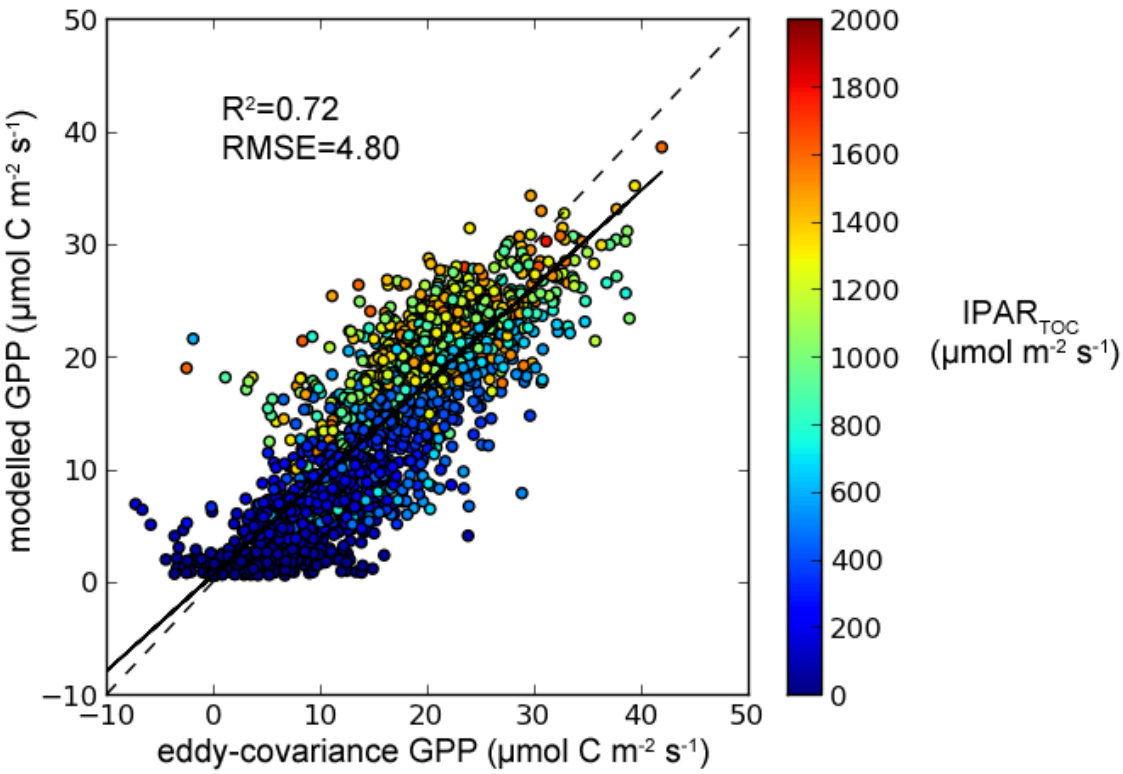

Figure 4.13: Model inversion using the Levenberg-Marquardt algorithm, with relative humidity, diurnal as well as mean daily temperature modifiers, with constrained quantum yield. Colours indicate top of canopy IPAR [μmol photons m^{-2} s^{-1}] (parameter values: $P_{opt} = 25.5$, $\alpha = 0.07$, $\chi = 0.9$, $\beta_{RH} = 89.2$, $\beta_T = 21.4$, $\beta_S = 2.7$, $T_{opt} = 15.1$, $\gamma_T = -0.4$, $\gamma_{RH} = 0.2$, $\gamma_S = 0.999$)

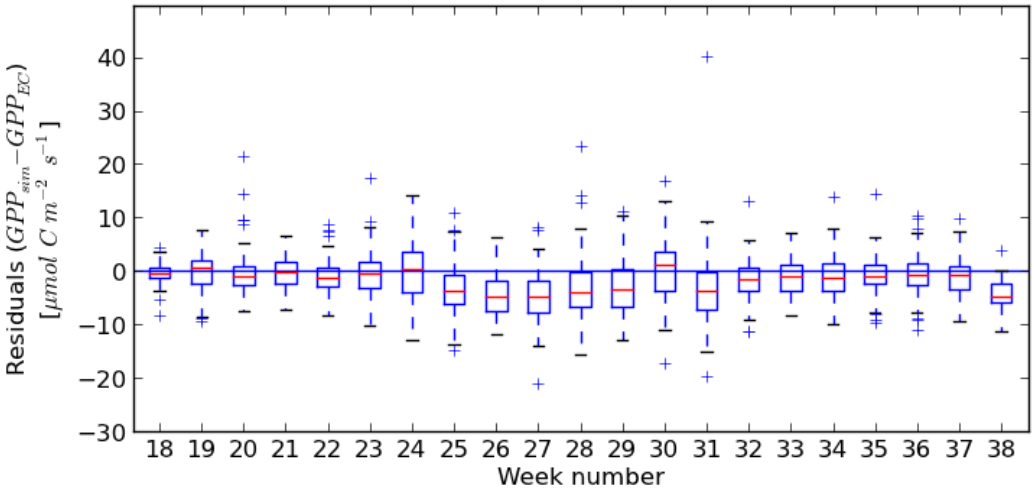

Figure 4.14: residual errors over time (week numbers for the year 2009) illustrating that some bias for the midseason is removed using modifier functions based on mean daily temperature.

4.4. Discussion

This study addressed the need for canopy radiation models that provide for the fusion of proximal- and remote sensing data. The model utilizes highly detailed canopy structural data to yield IPAR and photosynthetic assimilation at the branch level as well as plot-level GPP in a manner that provides for extensive time series analysis. IPAR was computed at the level of individual scene elements by integrating hemispherical, down-welling radiation corrected for the hit probability that is probability that a pencil of light from a specific direction in the sky penetrates the canopy and collides at a specific location in the canopy. The model was parameterized using 3D structural data that is acquired with laser scanning technology and field observations of crown architecture, time series measurements of incident diffuse and direct PAR, and leaf-level photosynthesis parameters including P_{max} or P_{opt}, α, χ, and parameters defining the down-regulation of photosynthesis resulting from changes in temperature and relative humidity. While the virtual scene is constructed in forward modeling mode, the photosynthetic parameters were determined through model inversion against EC flux-tower estimates using the Levenberg-Marquardt method. To improve conversion, two parameters (α, χ) were fixed, while other parameters remained unconstrained. Despite differences in scale between the modeled forest plot and the footprint of the eddy-covariance flux tower, model optimization resulted in simulated GPP values matching the range of error typical for the eddy-covariance technique (e.g. Baldocchi et al. 2001), while remaining model parameters were also within ranges typically reported in literature.

Model validation tests for conservation of energy show that the light transport model introduces some error that is due to approximation (Appendix A.3., A.4.). The first approximation comes from the sampling distribution to capture down-welling radiation that introduces an error by setting the sun angles to the best matching direction among a limited number of hemispherical directions. The second approximation stems from the systematic sampling introduced in computing P_{hit}. For every facet in the scene, a hit probability is computed by tracing rays originating from the centre of that facet towards unique hemispherical directions so that the hit probability of the facet centre represents the hit probability of the entire facet, and this can lead to bias in the estimated amount of radiation impinging on the facet. Other methods for computing P_{hit} may be used to avoid bias. For example, in radiosity modeling, view factors F_{ij} are computed that express the fraction of radiation leaving a facet i that reaches another facet j so that all view factors from a given facet sum to unity. (For comparison, in the current model the probabilities of a hit at facet p, before p and after p sum to unity.) Once view factors are determined, the radiosity equation is solved and has the form (Cohen & Wallace 1993):

$$B_i = E_i + \rho_i \sum_j^n F_{ij} B_j \qquad \text{e.q. 4.11.}$$

where B_i is the radiosity of surface element i (e.g. µmol photons m^{-2} s^{-1}) and is also known as radiant exitance or exitent flux density (Cohen & Wallace 1993; Schaepman-Strub et al. 2006), E_i is the surface emission and may be considered zero for woody and foliage elements and ρ_i is the surface reflectance or transmittance that is (bi-)directionally dependent.

This concept of view factors suits dynamic lighting conditions; however, it becomes computationally expensive when scenes comprise a large number of surface elements. Ray tracing methods (Disney et al. 2000; Gastellu-Etchegorry et al. 1996; Govaerts & Verstraete 1998; Chapter 3) on the other hand, handle arbitrarily large scenes and avoid bias by randomly locating ray origins as well as ray directions and provide for computing $P_{hit}(p, \phi_i, \theta_i)$ or, rather, the probability of absorbing radiation from a particular hemispherical direction; However, these benefits come at the expense of increasing the number of computational steps. Whether such computational expenses are desired, depends on the study at hand. Estimates of P_{hit} remain constant over prolonged periods of time, or undergo only modest changes due to foliage allocation, and once computed, the derivation of IPAR at the leaf level takes only a few seconds per time step (i.e. half hour), meaning that canopy radiation profiles from complex forest scenes may be obtained at a temporal resolution consistent with typical integration windows used for EC measurements or satellite overpasses.

Additional model approximations relate to the semi-empirical nature of the photosynthesis model and it was assumed that only ambient temperature and humidity affected photosynthetic down-regulation. Improvements may include the use of radiosity modeling to simulate the transfer of heat within the canopy, as opposed to the current assumption of having no spatial distribution of temperature within the canopy. The P_{max} modifier functions did not consider hysteresis in their response to changes in temperature and relative humidity. It is likely, however, that LUE responds more quickly to precipitation than to dry conditions. For example, for a drought to have a significant impact on photosynthesis a weather record of several weeks to months may need to be considered, whereas a sudden event of heavy rain after a prolonged period of dry conditions affects the growth of vegetation more quickly. Other important considerations are the allocation of nutrients and acclimation of leaves to prevalent PAR regimes (De Pury & Farquhar 1997) and temperature (Hember et al. 2010) as well as effects of transient changes in incident radiation on photosynthetic down-regulation (Pearcy 1990). An effective way to capture the combined effect of these processes is through augmenting the modeling

with proximal sensing techniques, such as sensor network data (Garrity et al. 2010). Future research will investigate model parameterization using photochemical reflectance (PRI) data that was obtained from inexpensive narrow-waveband sensor network (forthcoming). Such PRI sensor network data can be used to understand the regulative capacity of the canopy on radiation transport and vertical profiles of photosynthetic down-regulation. Combined with fine-scale models of photosynthesis and light transport these sensor network data can be fused with a broad range of existing physiology, biometeorology, and airborne and spaceborne remote sensing data sources to advance our knowledge about the variability of LUE within the canopy. Understanding gained through this fine-scale modeling may be used to formulate empirical relationships that describe the vertical variations in LUE for use in simpler productivity models such as the Monteith model for use at operational scales.

4.5. Conclusions

Canopy structure is an important driver for canopy radiation modeling and is an important component in forest GPP models as it determines how portions of diffuse and direct radiation are distributed throughout the canopy. In this study, a method was presented that provides rapid updates of the canopy radiation regime, after an initial, computationally intense model set-up phase. The model relies on the hit probability of individual branches and handles the dynamic changes in the canopy radiation that result from solar tracking and atmospheric conditions. Once canopy radiation was simulated, a single leaf-level photosynthesis model was used to model canopy productivity for a time series of over 2,000 measurements spread throughout a growing season. Through optimization of the model parameters to EC flux-tower data it was found that photosynthetic capacity was highest at cool temperatures (16 °C) and humid conditions (relative humidity > 75%) - in agreement with reported values for this climatic zone. While the current model suffers from model approximations, the research efforts presented herein offer a contribution towards the fusion of proximal and remote sensing data.

5. Conclusions

The confidence around remote sensing estimates of GPP is, in part, affected by the limitation to observe the variation in light use efficiency with canopy depth that is inherently related to the extinction of light with canopy depth. Current GPP models only use a coarse level of canopy structural detail and provide only spatially averaged estimates that make model parameterization with field observations challenging. While proximal sensing technology is increasingly able to capture fine resolution photosynthesis-related data, the fusion of these data with stand-level data is still challenging (see Figure 5.1). The objective of this thesis was to derive automated methodology for modeling canopy structure, light transport, and leaf-level photosynthesis using conventional inventory parameters, laser scanning data, and meteorological records, and to explore the feasibility to obtain leaf-level photosynthesis parameters from stand-level productivity measurements. This work was guided by three research questions (Chapter 1.4):

1. Can LiDAR remote sensing parameterize 3D radiative transfer models at scales ranging from shoot to plot level?

2. Can leaf-level IPAR be simulated over a growing season at a sub-hourly time step from arbitrarily complex canopy light models?

3. Can leaf-level physiological parameters be inferred from simulated canopy radiation and stand-level productivity estimates?

The first question relates to the potential of laser scanning technology to generate geometrically explicit models of forest canopies and is answered in Chapters 2 and 3. Chapter 2 demonstrates the use of the Hough transform to delineate individual, dominant tree crowns from LiDAR data. This delineation or segmentation of the LiDAR data into individual trees provides an important first step towards forest reconstruction. Chapter 3 demonstrates a finer resolution of modeling based on ground-based laser scanning data combined with tree-regeneration models. The reconstruction pipeline builds on the previous chapter and extends the modeling of trees by detecting individual stems and tessellating the scene into growing spaces for each stem. The wide-beam Echidna data used in this study provides for full-waveform data recordings but offers a limited point density and this makes reconstruction of individual branches challenging. However, the method demonstrates stems can be detected that are only 3 or 4 pixels wide in the range image, so that the method can be applied to low resolution data as

well as for the detection of finer stems using higher resolution scanner data. The latter also reduces the need for field observational data to parameterize the tree-regeneration models.

The second research question relates to the use of geometrically explicit models to simulate leaf-level incident PAR and this is addressed in Chapter 4. Previous models (e.g. McMurtrie et al. 1990; Wang & Jarvis 1990a, 1990b) have addressed the computation of averaged leaf-level PAR and these measures may not resemble the variability observed in the field. As a result, the fusion of shoot and canopy-level data has been challenging (Jarvis 1976). Ray tracing models have been used to simulate radiation transfer at arbitrary (Widlowski 2010) levels of detail; however, they are computationally expensive. The work presented in this thesis relies on the modeling of canopy radiation transfer based on hit probability as demonstrated by Jupp et al. (2009) and Yang et al. (2013); however, rather than a derivation of hit probabilities at the plot-level, the current work uses laser scanning data to establish a 3D-explicit forest scene for which branch or shoot-level hit probabilities can be simulated using ray tracing techniques. Once hit probabilities are determined for all scene elements, incident leaf-level IPAR can be computed rapidly to facilitate the study of diurnal as well as seasonal variations in photosynthetic assimilation at scales ranging from the leaf to the canopy-level.

The third research question investigates if parameters related to leaf-level assimilation can be inferred from eddy-covariance estimates of stand-level productivity and simulated canopy radiation. The simulation of stand-level productivity from a leaf-level photosynthesis model by integrating leaf-level assimilation over the canopy is not new and has been demonstrated in a number of models such as MAESTRO (Wang & Jarvis 1990) and BIOMASS (McMurtrie et al. 1990). However, these models require a large number of variables so that model inversion is challenging. The model developed in this thesis uses a semi-empirical photosynthesis model based on quantum yield and photosynthetic capacity and the latter is down-regulated as a function of environmental variables. A fully unconstrained optimization procedure was able to find realistic values for most photosynthesis parameters, however, quantum yield was found to exceed theoretical and observed limits that have been reported in literature. Fixing quantum yield to 0.07 µmol C µmol^{-1} photons reduced bias between simulated-, and eddy-covariance GPP estimates. Some variation among the residuals remained that appeared to be due to seasonal changes in the photosynthetic capacity and may be addressed using separate modifier functions for diurnal and seasonal trends in temperature. After parameter optimization, the correspondence between the model simulations and eddy-covariance estimates yielded an R^2 around 0.7 and RMSE around 4 µmol C m^{-2} ground s^{-1}. These results suggest that the current photosynthesis model captures some

important aspects of photosynthesis; however, more processes may need to be considered to explain variation in photosynthesis within the canopy. For example, vertical gradients in leaf temperature and relative humidity are the result of homeostatic functions of canopy structure and the creation of micro-meteorological sites within the canopy (Jarvis 1976; Parker et al. 2001), but only ambient temperature and relative humidity were used in the current study. Similarly, impacts of variations in hydraulic conductance within the canopy (Gamon & Bond 2013) on leaf-level photosynthesis were not explicitly captured in the current approach, nor were considered the age of leaves or the acclimation of leaves to direct sun or shade conditions. The results from the current study indicate that the use of increasingly fine detailed models of canopy structure facilitate the inference around photosynthesis parameters in a geometrically explicit manner, from stand level measurements of GPP, and also suggest that more physiological mechanisms may be incorporated in the modeling in future. The demonstrated progress in increasing the geometric resolution of canopy models and ability to infer leaf-level photosynthesis also indicates potential to fuse shoot and stand-level measurements, which then opens an important opportunity to leverage the significant research already on leaf and tree photosynthesis.

The outcomes of this research demonstrate the use of laser scanning data and graphically inclined tree-regeneration models for scaling measurements of canopy-level GPP to a geometrically explicit distribution of shoot-level productivity. The unique outcomes of this research include:

1) The development of a new approach to extract tree crowns and crown information from airborne and ground-based laser scanning data;

2) A new approach to detect and segment individual tree stems from ground-based laser scanning data resulting in highly accurate stem maps and DBH estimates at the plot level;

3) A new method to populate a virtual scene with trees based on a Voronoi tessellation of the derived stem map;

4) A new application of ray tracing models to simulate branch-level hit probabilities from which IPAR can be computed;

5) An innovative model to optimize leaf-level photosynthesis-related parameters to canopy-level GPP measurements.

The model developed within the framework of this thesis comprises a level of detail that is uncommon among established productivity models that typically rely on the use of spatially and

temporally averaged canopy attributes and environmental conditions; however, these models often include effective parameters that cannot be measured directly in the field (e.g. the average chlorophyll content over broad areas), or lack physical units (e.g. clumping index or soil quality), so that validation of underlying modeling assumptions can be challenging. In addition, certain physiological processes may not be resolved at these coarser levels of detail. For example, leaf-level responses to sunflecks (Pearcy 1990) may be obscured at the canopy-level where processes are primarily affected by the sunlit canopy fraction (Hall et al. 2012; Hilker et al. 2012a) that change at a much slower rate. The new model developed in this thesis overcomes these challenges to a significant extent by using conventional forest inventory information and fine structural information obtained from laser scans. This finer discretization of canopy structure provides for a spatial breakdown of PAR and photosynthetic efficiencies, and holds promise to simulate dynamic responses to changes in light (i.e. sunflecks) that are inherently related to the discrete nature of canopies (Pearcy 1990).

The reconstruction methods presented in this thesis were demonstrated for data from a 60-year-old Douglas-fir stand and the methods applied assumed a monopodial tree architecture (i.e. consisting of a single trunk that reaches from base to apex) that is typical for coniferous trees. The potential to include a broader diversity of tree species needs to be addressed in future studies. Of importance to note, however, is the potential of the stem detection method presented in Chapter 3 for branches of arbitrary order provides that the data resolution (i.e. point density) is high enough to resolve the individual branches by a minimum of 3 to 4 laser returns along the cross-sections of branches. Future studies may therefore investigate the use of high density laser scanner data as well as mobile and hand-held scanning devices to optimize point density and to address data obscuration.

The fusion of simulated radiative transfer and photosynthetic assimilation with proximal sensors provides an important means to study the variability of assimilation under transient light conditions and that may help us better understand the relationship between canopy structure and function (e.g. Pearcy 1990). Proximal sensors provide levels of detail in diurnal physiological changes that cannot be addressed with remote sensing techniques and the installation of these sensors offers a unique opportunity to study temporal variations in commonly used spectral indices. High frequency sampling of PRI or chlorophyll fluorescence, for example, provide accurate estimates of down-regulation of light use efficiency throughout the day as well as the season. In addition, their measurement is not hindered by cloud cover so that measurements represent a wider spectrum of meteorological conditions. Detailed geometric-explicit models provide for a “bottom-up” modeling approach, opposed to remote sensing

models that represent “top-down” approaches and require a break-down of signals from an aggregate level. For example, estimates of leaf-level biophysical parameters are obtained from canopy reflectance so that the confidence bounds of the estimates are based on a propagation of model errors and assumptions around the effects of geometric and volumetric scattering. The fusion of remote sensing data with data from proximal sensors and eddy-covariance stations also provides opportunities to reduce uncertainties around productivity estimates by identifying and reducing impacts of outliers in data collections.

Future efforts on the integration of proximal sensing with geometrically explicit light transport models should address reflectance, however, that currently remains a limitation of the model presented in Chapter 4. Including leaf-level reflectance in simulations provides for assimilation of top of canopy reflectance data, which can then be used for spectral mixture analysis that uses canopy reflectance data and a system of linear equations to obtain end-member reflectance data of sun and shade acclimated foliage elements (Middleton et al. 2009). For the case of single-scattering reflectance, the branch-level hit probabilities can be used to simulate the joint probability of exposure of scene elements to incoming radiation as well as the exposure of a virtual sensor to the lit scene elements. In the case of multi-scattering, a more elaborate method is required that handles multiple reflectance and collided transmittance of radiation. Such a method could be based on the ray tracer presented in Chapter 3 from which the probabilities of absorbing photons incident from a specific direction by a specific canopy element can be computed, or – when photons are reflected outside the scene towards the atmosphere – what their contribution to the canopy BRDF is. For multi-scattering, the concept of the hit probability may then be substituted by the probability of scene elements to absorb directional radiation as well as the probability of aggregates of scene elements to reflect the incoming, directional radiation towards an observer (Disney et al. 2000).

Modeling multiple scattering requires a significant amount of additional computation and it remains unclear whether improvements gained warrant this additional computational effort. The cost allowed for model simulation likely depends on the significance of the study site and long term research goals. Recent trends in the acquisition of forest inventory data in Canada have moved towards an intense use of permanent inventory plots (Gillis 2001). The continued monitoring and revisiting of study sites has reduced measurement uncertainties, and motivates investment in the geometrically explicit mapping of forest structure and computational cost of simulations. At the same time, long term maintenance of research sites imposes costs that limit the availability of ground-truth measurements of

productivity elsewhere, which then introduces uncertainty as to how well these sites represent the variation in productivity across the landscape. Proximal sensing techniques often rely on low-cost sensor network technology (Garrity et al. 2010; Soudani et al. 2012) so that the number of study areas may be increased at an affordable cost, much to the benefit of validating and calibrating a range of remote sensing products. These proximal sensing techniques monitor productivity-related variables at a scale that is common to laboratory studies as well as field mensuration. Hence, proximal techniques can be calibrated against laboratory standards before they are installed *in situ* at a study site, as opposed to remote sensing instruments for which typically only radiometric calibrations are conducted in laboratories, while the calibration of empirical relationships between spectral indices and GPP is exclusively achieved while the instrumentation is air-, or spaceborne. Proximal sensing, therefore, appears better suited to the acquisition of precision measurements and under a wider range of environmental conditions, whereas the strength of remote sensing methods primarily lies in the scaling of estimates across the landscape and broader scales.

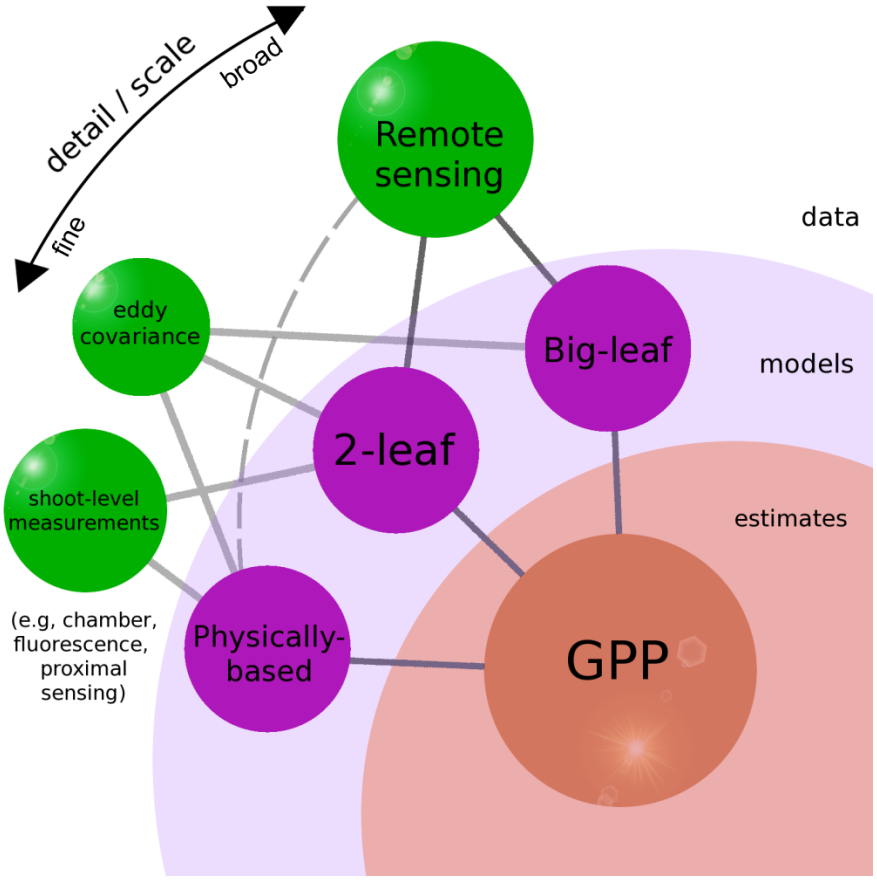

Figure 5.1: A network representation of data and models of forest gross primary productivity operating at various scales and levels of detail. The dashed arch illustrates the lack of process-based models that provide for fusion of proximal and remote sensing data sources.

References

Ahn, T. K., Avenson, T. J., Ballottari, M., Cheng, Y.-C., Niyogi, K. K., Bassi, R., & Fleming, G. R. (2008). Architecture of a charge-transfer state regulating light harvesting in a plant antenna protein. *Science*, *320*, 794–797. doi:10.1126/science.1154800

Andersen, H.-E., McGaughey, R. J., & Reutebuch, S. E. (2005). Estimating forest canopy fuel parameters using LIDAR data. *Remote Sensing of Environment*, *94*, 441–449. doi:10.1016/j.rse.2004.10.013

Andrieu, B., Sohbi, Y., & Ivanov, N. (1994). A direct method to measure bidirectional gap fraction in vegetation canopies. *Remote Sensing of Environment*, *66*, 61–66.

Arecchi, A. V., Messadi, T., & Koshel, R. J. (2007). *Field guide to illumination*. (J. E. Greivenkamp, Ed.) (p. 137). Bellingham, Washington: SPIE. doi:10.1117/3.764682

Aschoff, T., & Spiecker, H. (2004). Algorithms for the automatic detection of trees in laser scanner data. *International Archives of Photogrammetry, Remote Sensing and Spatial Information Sciences*, *XXXVI* part 8/W2, 71–75.

Asrar, G., & Myneni, R. B. (1991). Applications of radiative transfer models for remote sensing of vegetation conditions and states. In R. B. Myneni & J. Ross (Eds.), *Photon-Vegetation Interactions: Applications in Optical Remote Sensing and Plant Ecology* (pp. 538–558). Berlin Heidelberg: Springer-Verlag.

Baldocchi, D., Falge, E., Gu, L., Olson, R., Hollinger, D., Running, S., Anthoni, P., Bernhofer, Ch., Davis, K., Evans, R., Fuentes, J., Goldstein, A., Katul, G., Law, B., Lee, X., Malhi, Y., Meyers, T., Munger, W., Ochel, W., Paw. K.T., Pilegaard, K., Schmid, H.P., Valentini, R., Verma, S., Vesala, T., Wilson, K., & Wofsy, S. (2001). FLUXNET: a new tool to study the temporal and spatial variability of ecosystem-scale carbon dioxide, water vapor, and energy flux densities. *Bulletin of the American Meteorological Society*, *82*, 2415–2434.

Barton, C. V. M., & North, P. R. J. (2001). Remote sensing of canopy light use efficiency using the photochemical reflectance index model and sensitivity analysis. *Remote Sensing of Environment*, *78*, 264–273.

Ben-Arie, J. R., Hay, G. J., Powers, R. P., Castilla, G., & St-Onge, B. (2009). Development of a pit filling algorithm for LiDAR canopy height models. *Computers & Geosciences*, *35*, 1940–1949. doi:10.1016/j.cageo.2009.02.003

Beraldin, J.-A., Blais, F., Boulanger, P., Cournoyer, L., Domey, J., El-Hakim, S. F., Godin, G., Rioux, M., & Taylor, J. (2000). Real world modelling through high resolution digital 3D imaging of objects and structures. *ISPRS Journal of Photogrammetry and Remote Sensing*, *55*, 230–250. doi:10.1016/S0924-2716(00)00013-7

Bienert, A., Scheller, S., Keane, E., Mohan, F., & Nugent, C. (2007). Tree detection and diameter estimations by analysis of forest terrestrial laserscanner point clouds. In *Laser Scanning 2007 and*

SilviLaser 2007 (pp. 50–55). Espoo, Finland: International Society for Photogrammetry and Remote Sensing.

Black, A. T., Chen, J.-M., Lee, X., & Sagar, R. M. (1991). Characteristics of shortwave and longwave irradiances under a Douglas-fir forest stand. *Canadian Journal of Forest Research*, *21*, 1020–1028.

Blackburn, G. A. (2007). Wavelet decomposition of hyperspectral data: a novel approach to quantifying pigment concentrations in vegetation. *International Journal of Remote Sensing*, *28*, 2831–2855. doi:10.1080/01431160600928625

Blackburn, G. A., & Ferwerda, J. (2008). Retrieval of chlorophyll concentration from leaf reflectance spectra using wavelet analysis. *Remote Sensing of Environment*, *112*, 1614–1632. doi:10.1016/j.rse.2007.08.005

Brandtberg, T., Warner, T. A., Landenberger, R. E., & McGraw, J. B. (2003). Detection and analysis of individual leaf-off tree crowns in small footprint, high sampling density lidar data from the eastern deciduous forest in North America. *Remote Sensing of Environment*, *85*, 290–303. doi:10.1016/S0034-4257(03)00008-7

Breidenbach, J., Næsset, E., Lien, V., Gobakken, T., & Solberg, S. (2010). Prediction of species specific forest inventory attributes using a nonparametric semi-individual tree crown approach based on fused airborne laser scanning and multispectral data. *Remote Sensing of Environment*, *114*, 911–924. doi:10.1016/j.rse.2009.12.004

Bucksch, A., Lindenbergh, R., & Menenti, M. (2010). SkelTre. *The Visual Computer*, *26*(10), 1283–1300. doi:10.1007/s00371-010-0520-4

Cai, T., Black, A., Jassal, R. S., Morgenstern, K., & Nesic, Z. (2009). Incorporating diffuse photosynthetically active radiation in a single-leaf model of canopy photosynthesis for a 56-year-old Douglas-fir forest. *International Journal of Biometeorology*, *53*, 135–48. doi:10.1007/s00484-008-0196-x

Cannell, M. G. R., & Thornley, J. H. M. (1998). Temperature and CO_2 responses of leaf and canopy photosynthesis: A clarification using the non-rectangular hyperbola model of photosynthesis. *Annals of Botany*, *82*, 883–892.

Chen, J. M., & Black, T. A. (1992). Foliage area and architecture of plant canopies from sunfleck size distributions. *Agricultural and Forest Meteorology*, *60*, 249–266. doi:10.1016/0168-1923(92)90040-B

Chen, J.M. (1996). Canopy architecture and remote sensing of the fraction of photosynthetically active radiation absorbed by boreal conifer forests. *IEEE Transactions on Geoscience and Remote Sensing*, *34*, 1353–1368.

Chen, Q., Baldocchi, D., Gong, P., & Kelly, M. (2006). Isolating individual trees in savana woodland using small footprint lidar data. *Photogrammetric Engineering & Remote Sensing, 72*, 923-932.

Chen, J. M., Govind, A., Sonnentag, O., Zhang, Y., Barr, A., & Amiro, B. (2006). Leaf area index measurements at Fluxnet-Canada forest sites. *Agricultural and Forest Meteorology*, *140*, 257–268. doi:10.1016/j.agrformet.2006.08.005

Choudhury, B. (2001). Estimating gross photosynthesis using satellite and ancillary data approach and preliminary results. *Remote Sensing of Environment*, *75*, 1–21. doi:10.1016/S0034-4257(00)00151-6

Clawges, R., Vierling, L., Calhoon, M., & Toomey, M. (2007). Use of a ground-based scanning lidar for estimation of biophysical properties of western larch (Larix occidentalis). *Internation Journal of Remote Sensing*, *28*, 4331-4344.

Cohen, M. F., & Wallace, J. R. (1993). *Radiosity and realistic image synthesis* (p. 381). London: Academic press.

Coops, N. C., Hilker, T., Wulder, M. A., St-Onge, B., Newnham, G. J., Siggins, A., & Trofymow, J. A. (2007). Estimating canopy structure of Douglas-fir forest stands from discrete-return LiDAR. *Trees*, *21*, 295–310. doi:10.1007/s00468-006-0119-6

Coops, N. C., Waring, R. H., & Schroeder, T. A. (2009). Combining a generic process-based productivity model and a statistical classification method to predict the presence and absence of tree species in the Pacific Northwest, U.S.A. *Ecological Modelling*, *220*, 1787–1796. doi:10.1016/j.ecolmodel.2009.04.029

Coops, N. C., Wulder, M. A., Duro, D. C., Han, T., & Berry, S. (2008). The development of a Canadian dynamic habitat index using multi-temporal satellite estimates of canopy light absorbance. *Ecological Indicators*, *8*, 754–766. doi:10.1016/j.ecolind.2008.01.007

Côté, J.-F., Fournier, R. A., & Egli, R. (2011). An architectural model of trees to estimate forest structural attributes using terrestrial LiDAR. *Environmental Modelling & Software*, *26*, 761–777. doi:10.1016/j.envsoft.2010.12.008

Côté, J.-F., Fournier, R. A., Frazer, G. W., & Niemann, K. O. (2012). A fine-scale architectural model of trees to enhance LiDAR-derived measurements of forest canopy structure. *Agricultural and Forest Meteorology*, *166-167*, 72–85. doi:10.1016/j.agrformet.2012.06.007

Côté, J.-F., Widlowski, J.-L., Fournier, R. A., & Verstraete, M. M. (2009). The structural and radiative consistency of three-dimensional tree reconstructions from terrestrial lidar. *Remote Sensing of Environment*, *113*, 1067–1081. doi:10.1016/j.rse.2009.01.017

Daniels II, J., Ochotta, T., Ha, L. K., & Silva, C. T. (2008). Spline-based feature curves from point-sampled geometry. *The Visual Computer*, *24*, 449–462. doi:10.1007/s00371-008-0223-2

Das, S., Mirnalinee, T. T., & Varghese, K. (2011). Use of salient features for the design of a multistage framework to extract roads from high-resolution multispectral satellite images. *IEEE Transactions on Geoscience and Remote Sensing*, *49*, 3906–3931. doi:10.1109/TGRS.2011.2136381

De Groot, R., Brander, L., van der Ploeg, S., Costanza, R., Bernard, F., Braat, L., Christie, M., Crossman, N., Ghermandi, A., Hein, L., Hussain, S., Kumar, P., McVittie, A., Portela, R., Rodriguez, L. C., Ten Brink, P., & van Beukering, P. (2012). Global estimates of the value of ecosystems and their services in monetary units. *Ecosystem Services*, *1*, 50–61. doi:10.1016/j.ecoser.2012.07.005

De Groot, R., Van der Perk, J., Chiesura, A., & Marguliew, S. (2000). Ecological functions and socio-economic values of critical natural capital as a measure for ecological integrity and environmental health. In P. Crabbe (Ed.), *Implementing Ecological Integrity Restoring Regional and Global Environmental and Human Health* (pp. 191–214). Dordrecht, The Netherlands: Springer Science+Business Media.

De Pury, D. G. G., & Farquhar, G. D. (1997). Simple scaling of photosynthesis from leaves to canopies without the errors of big-leaf models. *Plant, Cell and Environment*, *20*, 537–557. doi:10.1111/j.1365-3040.1997.00094.x

Demmig-Adams, B., & Adams, W. W. (2006). Photoprotection in an ecological context: The remarkable complexity of thermal energy dissipation. *New phytologist*, *172*, 11–21. doi:10.1111/j.1469-8137.2006.01835.x

Disney, M. I., Lewis, P., & North, P. R. J. (2000). Monte Carlo ray tracing in optical canopy reflectance modelling. *Remote Sensing Reviews*, *18*, 163–196. doi:10.1080/02757250009532389

Douglas, E. S., Strahler, A., Martel, J., Cook, T., Mendillo, C., Marshall, R., Chakrabarti, S., Schaaf, C., Woodcock, C., Li, Z., Yang, X., Culvenor, D., Jupp, D., Newnham, G., & Lovell, J. (2012). DWEL: A dual-wavelength Echidna lidar for ground-based forest scanning. In *2012 IEEE International Geoscience and Remote Sensing Symposium* (pp. 4998–5001). Munich, Germany: IEEE. doi:10.1109/IGARSS.2012.6352489

Drake, J. B., Dubayah, R. O., Clark, D. B., Knox, R. G., Blair, J. B., Hofton, M. A, Chazdon, R. L., Weishampel, J. F., & Prince, S. (2002). Estimation of tropical forest structural characteristics using large-footprint lidar. *Remote Sensing of Environment*, *79*, 305–319. doi:10.1016/S0034-4257(01)00281-4

Duda, R. O., Hart, P. E., & Stork, D. G. (2001). Pattern classification (second edition). John Wiley & Sons, Inc., New York, pp. 655.

Eitel, J. U. H., Vierling, L. A., & Long, D. S. (2010). Simultaneous measurements of plant structure and chlorophyll content in broadleaf saplings with a terrestrial laser scanner. *Remote Sensing of Environment*, *114*, 2229-2237.

Eitel, J. U. H., Vierling, L. A., & Magney, T. S. (2013). A lightweight, low cost autonomously operating terrestrial laser scanner for quantifying and monitoring ecosystem structural dynamics. *Agricultural and Forest Meteorology*, *180*, 86–96. doi:10.1016/j.agrformet.2013.05.012

Ethier, G. J., Livingston, N. J., Harrison, D. L., Black, T. A., & Moran, J. A. (2006). Low stomatal and internal conductance to CO_2 versus Rubisco deactivation as determinants of the photosynthetic

decline of ageing evergreen leaves. *Plant, Cell & Environment*, *29*, 2168–2184. doi:10.1111/j.1365-3040.2006.01590.x

Ethier, G. J., & Livingston, N. J. (2004). On the need to incorporate sensitivity to CO_2 transfer conductance into the Farquhar-von Caemmerer-Berry leaf photosynthesis model. *Plant, Cell and Environment*, *27*, 137–153. doi:10.1111/j.1365-3040.2004.01140.x

Farquhar, G. D., Von Caemmerer, S., & Berry, J. A. (1980). A biochemical model of photosynthetic CO_2 assimilation in leaves of C_3 species. *Planta*, *149*, 78–90.

Farquhar, G. D., von Caemmerer, S., & Berry, J. A. (2001). Models of photosynthesis. *Plant Physiology*, *125*, 42–45.

Ferster, C. J., Coops, N. C., & Trofymow, J. A. (2009). Above-ground large tree mass estimation in a coastal forest in British Columbia using plot-level metrics and individual tree detection from LiDAR. *Canadian Journal of Remote Sensing*, *35*, 270–275.

Field, C. (1983). Allocating leaf nitrogen for the maximization of carbon gain: Leaf age as a control on the allocation program. *Oecologia*, *56*, 341–347. doi:10.1007/BF00379710

Field, C. B., Ball, J. T., & Berry, J. A. (1989). Photosynthesis: principles and field techniques. In R W Pearcy, J. Ehleringer, H. A. Mooney, & P. W. Rundel (Eds.), *Plant Physiological Ecology* (pp. 301–325). New York: Chapman and Hall.

Filella, I., Amaro, T., Araus, L. J., & Penuelas, J. (1996). Relationship between photosynthetic radiation-use efficiency of barley canopies and the photochemical reflectance index (PRI). *Physiologia Plantarum*, *96*, 211–216.

Fleck, S., Van der Zande, D., Schmidt, M., & Coppin, P. (2004). Reconstructions of tree structure from laser-scans and their use to predict physiological properties and processes in canopies. *International Archives of the Photogrammetry, Remote Sensing and Spatial Information Sciences*, *XXXVI* part 3/W52, 119–123.

Fua, P. (1993). A parallel stereo algorithm that produces dense depth maps and preserves image features. *Machine Vision and Applications*, *6*, 35–49.

Gamfeldt, L., Snäll, T., Bagchi, R., Jonsson, M., Gustafsson, L., Kjellander, P., Ruiz-Jean, M. C., Froberg, M., Stendahl, J., Philipson, Ch. D., Mikusinski, G., Andersson, E., Westerlund, B., Andren, H., Moberg, F., Moen, J., & Bengtsson, J. (2013). Higher levels of multiple ecosystem services are found in forests with more tree species. *Nature communications*, *4*, 1340. doi:10.1038/ncomms2328

Gamon, A., Penuelas, J., & Field, C. B. (1992). A narrow-waveband spectral index that tracks diurnal changes in photosynthetic efficiency. *Remote Sensing Letters*, *41*, 35–44.

Gamon, J. A., & Bond, B. (2013). Effects of irradiance and photosynthetic downregulation on the photochemical reflectance index in Douglas-fir and ponderosa pine. *Remote Sensing of Environment*, *135*, 141–149. doi:10.1016/j.rse.2013.03.032

Garrity, S. R., Vierling, L. A., & Bickford, K. (2010). A simple filtered photodiode instrument for continuous measurement of narrowband NDVI and PRI over vegetated canopies. *Agricultural and Forest Meteorology*, *150*, 489–496. doi:10.1016/j.agrformet.2010.01.004

Gastellu-Etchegorry, J. P., Demarez, V., Pinel, V., & Zagolski, F. (1996). Modeling radiative transfer in heterogeneous 3-D vegetation canopies. *Remote Sensing of Environment*, *156*, 131–156.

Gaulton, R., Danson, F. M., Ramirez, F. A., & Gunawan, O. (2013). The potential of dual-wavelength laser scanning for estimating vegetation moisture content. *Remote Sensing of Environment*, *132*, 32–39. doi:10.1016/j.rse.2013.01.001

Gaveau, D. L. A., & Hill, R. A. (2003). Quantifying canopy height underestimation by laser pulse penetration in small-footprint airborne laser scanning data. *Canadian Journal of Remote Sensing*, *29*, 650–657. doi:10.5589/m03-023

Gerstl, S. A. W., & Borel, C. C. (1992). Principles of the radiosity method versus radiative transfer for canopy reflectance modeling. *IEEE Transactions on Geoscience and Remote Sensing*, *30*, 271–275. doi:10.1109/36.134077

Gibbs, H. K., Brown, S., Niles, J. O., & Foley, J. A. (2007). Monitoring and estimating tropical forest carbon stocks: making REDD a reality. *Environmental Research Letters*, *2*, 045023. doi:10.1088/1748-9326/2/4/045023

Gillis, M. D. (2001). Canada's national forest inventory (responding to current information needs). *Environmental Modeling & Assessment*, *67*, 121–129.

Gitelson, A. A., Viña, A., Verma, S. B., Rundquist, D. C., Arkebauer, T. J., Keydan, G., Leavitt, B., Ciganda, V., Burba, G. G., & Suyker, A. E. (2006). Relationship between gross primary production and chlorophyll content in crops: Implications for the synoptic monitoring of vegetation productivity. *Journal of Geophysical Research*, *111*, D08S11. doi:10.1029/2005JD006017

Givnish, T. J. (1988). Adaptation to Sun and Shade: A whole-plant perspective. *Australian Journal of Botany*, *15*, 63–92.

Gobron, N., Pinty, B., Aussedat, O., Chen, J. M., Cohen, W. B., Fensholt, R., Gond, V., Huemmrich, R., Lavergne, T., Melin, F., Privette, J. L., Sandholt, I., Taberner, M., Turner, D. P., Verstraete, M. M., & Widlowski, J.-L. (2006). Evaluation of fraction of absorbed photosynthetically active radiation products for different canopy radiation transfer regimes: Methodology and results using Joint Research Center products derived from SeaWiFS against ground-based estimations. *Journal of Geophysical Research*, *111*, D13110. doi:10.1029/2005JD006511

Godin, C., Costes, E., & Sinoquet, H. (1999). A method for describing plant architecture which integrates topology and geometry. *Annals of Botany*, *84*, 343–357.

Govaerts, Y. M., & Verstraete, M. M. (1998). Raytran: A Monte Carlo ray-tracing model to compute light scattering in three-dimensional heterogeneous media. *IEEE Transactions on Geoscience and Remote Sensing*, *36*, 493–505. doi:10.1109/36.662732

Gruen, A., & Akca, D. (2005). Least squares 3D surface and curve matching. *ISPRS Journal of Photogrammetry and Remote Sensing*, *59*, 151–174. doi:10.1016/j.isprsjprs.2005.02.006

Hall, F. G., Hilker, T., & Coops, N. C. (2012). Data assimilation of photosynthetic light-use efficiency using multi-angular satellite data: I. Model formulation. *Remote Sensing of Environment*, *121*, 301–308. doi:10.1016/j.rse.2012.02.007

Halle, F., Olderman, R. A. A., & Tomlinson, P. B. (1978). *Tropical trees and forests. An architectural analysis.* (p. 441). Berlin: Springer-Verlag.

Heinsch, F. A., Reeves, M., Votava, P., Kang, S., Milesi, C., Glassy, J., Jolly, W. M., Loehman, R., Bowker, Ch. F., Kimball, J. S., Nemani, R. R., & Running, S. W. (2003). User's guide GPP and NPP (MOD17A2/A3) products NASA MODIS land algorithm. Retrieved from http://www.ntsg.umt.edu/sites/ntsg.umt.edu/files/modis/MOD17UsersGuide.pdf (last accessed December 31, 2013).

Hember, R. A., Coops, N. C., Black, T. A., & Guy, R. D. (2010). Simulating gross primary production across a chronosequence of coastal Douglas-fir forest stands with a production efficiency model. *Agricultural and Forest Meteorology*, *150*, 238–253. doi:10.1016/j.agrformet.2009.11.004

Herold, M., & Johns, T. (2007). Linking requirements with capabilities for deforestation monitoring in the context of the UNFCCC-REDD process. *Environmental Research Letters*, *2*, 045025. doi:10.1088/1748-9326/2/4/045025

Heurich, M. (2008). Automatic recognition and measurement of single trees based on data from airborne laser scanning over the richly structured natural forests of the Bavarian Forest National Park. *Forest Ecology and Management*, *255*, 2416–2433. doi:10.1016/j.foreco.2008.01.022

Hilker, T., Coops, N. C., Wulder, M. A., Black, T. A., & Guy, R. D. (2008). The use of remote sensing in light use efficiency based models of gross primary production: a review of current status and future requirements. *The Science of the Total Environment*, *404*, 411–23. doi:10.1016/j.scitotenv.2007.11.007

Hilker, T., Hall, F. G., Coops, N. C., Lyapustin, A., Wang, Y., Nesic, Z., Grant, N., Black, T. A., Wulder, M. A., Kljun, N., Hopkinson, Ch., Chasmer, L., & Kljun, N. (2010a). Remote sensing of photosynthetic light-use efficiency across two forested biomes: spatial scaling. *Remote Sensing of Environment*, *114*, 2863–2874. doi:10.1016/j.rse.2010.07.004

Hilker, T., Hall, F. G., Tucker, C. J., Coops, N. C., Black, T. A., Nichol, C. J., Sellers, P. J., Barr, A., Hollinger, D. Y., & Munger, J. W. (2012a). Data assimilation of photosynthetic light-use efficiency using multi-angular satellite data: II Model implementation and validation. *Remote Sensing of Environment*, *121*, 287–300. doi:10.1016/j.rse.2012.02.008

Hilker, T., Van Leeuwen, M., Coops, N. C., Wulder, M. A., Newnham, G. J., Jupp, D. L. B., & Culvenor, D. S. (2010b). Comparing canopy metrics derived from terrestrial and airborne laser scanning in a Douglas-fir dominated forest stand. *Trees*, *24*, 819–832. doi:10.1007/s00468-010-0452-7

Hilker, T., Lepine, L., Coops, N. C., Jassal, R. S., Black, T. A., Wulder, M. A., Ollinger, S., Tsui, O., & Day, M. (2012b). Assessing the impact of N-fertilization on biochemical composition and biomass of a Douglas-fir canopy—A remote sensing approach. *Agricultural and Forest Meteorology*, *153*, 124–133. doi:10.1016/j.agrformet.2011.03.014

Hilker, T., Wulder, M. A., Coops, N. C., Linke, J., McDermid, G., Masek, J. G., Gao, F., & White, J. C. (2009). A new data fusion model for high spatial- and temporal-resolution mapping of forest disturbance based on Landsat and MODIS. *Remote Sensing of Environment*, *113*, 1613–1627. doi:10.1016/j.rse.2009.03.007

Holmgren, J., & Nilsson, M. (2003). Estimation of tree height and stem volume on plots using airborne laser scanning. *Forest Science*, *49*, 419–428.

Holt, N. E., Fleming, G. R., Niyogi, K. K. (2004) Toward an understanding of the mechanism of nonphotochemical quenching in green plants. *Biochemistry*, *43*, 8281-8289.

Hough, P. V. C. (1962). Method and means for recognizing complex patterns. U.S. patent no. 3,069,654.

Humphreys, E. R., Black, T. A., Morgenstern, K., Cai, T., Drewitt, G. B., Nesic, Z., & Trofymow, J. A. (2006). Carbon dioxide fluxes in coastal Douglas-fir stands at different stages of development after clearcut harvesting. *Agricultural and Forest Meteorology*, *140*, 6–22. doi:10.1016/j.agrformet.2006.03.018

Jacquemoud, S., Baret, F., Andrieu, B., Danson, F. M., & Jaggard, K. (1995). Extraction of vegetation biophysical parameters by inversion of the PROSPECT + SAIL models on sugar beet canopy reflectance data. Application to TM and AVIRIS sensors. *Remote Sensing of Environment*, *52*, 163–172. doi:10.1016/0034-4257(95)00018-V

Jacquemoud, Stéphane, Verhoef, W., Baret, F., Bacour, C., Zarco-Tejada, P. J., Asner, G. P., François, Ch., & Ustin, S. L. (2009). PROSPECT+SAIL models: A review of use for vegetation characterization. *Remote Sensing of Environment*, *113*, S56–S66. doi:10.1016/j.rse.2008.01.026

Jarvis, A. J., Stauch, V. J., Schulz, K., & Young, P. C. (2004). The seasonal temperature dependency of photosynthesis and respiration in two deciduous forests. *Global Change Biology*, *10*, 939–950. doi:10.1111/j.1365-2486.2004.00743.x

Jarvis, P. G. (1976). The interpretation of the variations in leaf water potential and stomatal conductance found in canopies in the field. *Philosophical Transactions of the Royal Society B: Biological Sciences*, *273*, 593–610. doi:10.1098/rstb.1976.0035

Jassal, R. S., Black, T. A., Spittlehouse, D. L., Brümmer, C., & Nesic, Z. (2009). Evapotranspiration and water use efficiency in different-aged Pacific Northwest Douglas-fir stands. *Agricultural and Forest Meteorology*, *149*, 1168–1178. doi:10.1016/j.agrformet.2009.02.004

Jupp, D. L. B., Culvenor, D. S., Lovell, J. L., Newnham, G. J., Strahler, A. H., & Woodcock, C. E. (2009). Estimating forest LAI profiles and structural parameters using a ground-based laser called "Echidna". *Tree physiology*, *29*, 171–81. doi:10.1093/treephys/tpn022

Kao, W., & Forseth, I. N. (1991). Dirunal leaf movement, chlorophyll fluorescence and carbon assimilation in soybean grown under different nitrogen and water availabilities. *Plant, Cell & Environment*, *15*, 703–710.

Kato, A., Moskal, L. M., Schiess, P., Swanson, M. E., Calhoun, D., & Stuetzle, W. (2009). Capturing tree crown formation through implicit surface reconstruction using airborne lidar data. *Remote Sensing of Environment*, *113*, 1148–1162. doi:10.1016/j.rse.2009.02.010

Koch, B. (2010). Status and future of laser scanning, synthetic aperture radar and hyperspectral remote sensing data for forest biomass assessment. *ISPRS Journal of Photogrammetry and Remote Sensing*, *65*, 581–590. doi:10.1016/j.isprsjprs.2010.09.001

Krishnan, P., Black, T. A., Jassal, R. S., Chen, B., & Nesic, Z. (2009). Interannual variability of the carbon balance of three different-aged Douglas-fir stands in the Pacific Northwest. *Journal of Geophysical Research*, *114*, G04011. doi:10.1029/2008JG000912

Landsberg, J. (2003). Physiology in forest models: History and the future. *Forest Biometry, Modelling and Information Sciences*, *1*, 49–63.

Leckie, D., Gougeon, F., Hill, D., Quinn, R., Armstrong, L., & Shreenan, R. (2003). Combined high-density lidar and multispectral imagery for individual tree crown analysis. *Canadian Journal of Remote Sensing*, *29*, 633–649. doi:10.5589/m03-024

Liang, S. (2004). *Quantitative remote sensing of land surfaces*. (J. A. Kong, Ed.) (p. 534). Hoboken, New Jersey: John Wiley & Sons, Inc.

Liang, X., Litkey, P., Kaartinen, H., Vastaranta, M., & Holopainen, M. (2012). Automatic stem mapping using single-scan terrestrial laser scanning. *IEEE Transactions on Geoscience and Remote Sensing*, *50*, 661–670.

Lim, K., Treitz, P., Wulder, M., St-Onge, B., & Flood, M. (2003). LiDAR remote sensing of forest structure. *Progress in Physical Geography*, *27*, 88–106. doi:10.1191/0309133303pp360ra

Liu, C., Welham, C. V. J., Zhang, X., & Wang, R. (2007). Leaflet movement of Robinia pseudoacacia in response to a changing light environment. *Journal of Integrative Plant Biology*, *49*, 419–424. doi:10.1111/j.1672-9072.2006.00392.x

Liu, Y., Yang, H., & Wang, W. (2005). Reconstructing B-spline curves from point clouds--A tangential flow approach using least squares minimization. In *Proceedings of the International Conference on Shape Modeling and Applications 2005* (pp. 4–12). Washington, DC, USA: IEEE Computer Society. doi:10.1109/SMI.2005.39

Livny, Y., Yan, F., Olson, M., Chen, B., Zhang, H., & El-Sana, J. (2010). Automatic reconstruction of tree skeletal structures from point clouds. *ACM Transactions on Graphics*, *29*, article no. 151. doi:10.1145/1882261.1866177

Lovell, J. L., Jupp, D. L. B., Culvenor, D. S., & Coops, N. C. (2003). Using airborne and ground-based ranging lidar to measure canopy structure in Australian forests. *Canadian Journal of Remote Sensing*, *29*, 607–622. doi:10.5589/m03-026

Luo, Y., Medlyn, B., Hui, D., Ellsworth, D., Reynolds, J., & Katul, G. (2001). Gross primary productivity in Duke forest: Modeling synthesis of CO_2 experiment and eddy-flux data. *Ecological Applications*, *11*, pp. 239–252. Retrieved from http://www.jstor.org/stable/3061070 (Last accessed on December 31, 2013)

Maas, H. G., Bienert, A., Scheller, S., & Keane, E. (2008). Automatic forest inventory parameter determination from terrestrial laser scanner data. *International Journal of Remote Sensing*, *29*, 1579–1593. doi:10.1080/01431160701736406

Mäkelä, A., Pulkkinen, M., Kolari, P., Lagergren, F., Berbigier, P., Lindroth, A., Loustau, D., Nikinmaa, E., Vesala, T., & Hari, P. (2008). Developing an empirical model of stand GPP with the LUE approach: analysis of eddy covariance data at five contrasting conifer sites in Europe. *Global Change Biology*, *14*, 92–108. doi:10.1111/j.1365-2486.2007.01463.x

Mariscal, M., Martens, S., Ustin, S., Chen, J., Weiss, S., & Roberts, D. (2004). Light-transmission profiles in an old-growth forest canopy: simulations of photosynthetically active radiation by using spatially explicit radiative transfer models. *Ecosystems*, *7*, 454–467. doi:10.1007/s10021-004-0137-4

Martinez-Perez, M. E., Hughes, A. D., Stanton, A. V, Thom, S. A., Bharath, A. A., & Parker, K. H. (1999). Retinal blood vessel segmentation by means of scale-space analysis and region growing. In C. Taylor & A. Colchester (Eds.), *Medical image computing and computer-assisted intervention - MICCAI'99* (pp. 90–97). Berlin Heidelberg: Springer.

Maxwell, K., & Johnson, G. N. (2000). Chlorophyll fluorescence--a practical guide. *Journal of Experimental Botany*, *51*, 659–668.

McMurtrie, R. E., Rook, D. A., & Kelliher, F. M. (1990). Modelling the yield of Pinus radiata on a site limited by water and nitrogen. *Forest Ecology and Management*, *30*, 381–413. doi:10.1016/0378-1127(90)90150-A

McMurtrie, R. E., & Wang, Y.-P. (1993). Mathematical models of the photosynthetic response of tree stands to rising CO_2 concentrations and temperatures. *Plant, Cell and Environment*, *16*, 1–13.

Mech, R., & Prusinkiewicz, P. (1996). Visual models of plants interacting with their environment. In *ACM SIGGRAPH 96* (Vol. 96, pp. 397–410).

Medlyn, B. E., Dreyer, E., Ellsworth, D., Forstreuter, M., Harley, P. C., Kirschbaum, M. U. F., & Roux, X. L. E. (2002). Temperature response of parameters of a biochemically based model of photosynthesis. II. A review of experimental data. *Plant, Cell and Environment*, *25*, 1167–1179.

Mei, C., & Durrieu, S. (2004). Tree crown delineation from digital elevation models and high resolution imagery. *International Archives of Photogrammetry, Remote Sensing and Spatial Information Sciences*, *XXXVI* part 8/W2, 218–223.

Meidinger, D. V, & Pojar, J. (1991). *Ecosystems of British Columbia*. British Columbia Ministry of Forests. Victoria, British Columbia, Canada, pp. 330.

Middleton, E. M., Cheng, Y.-B., Hilker, T., Black, T. A., Krishnan, P., Coops, N. C., & Huemmrich, K. F. (2009). Linking foliage spectral responses to canopy-level ecosystem photosynthetic light-use efficiency at a Douglas-fir forest in Canada. *Canadian Journal of Remote Sensing*, *35*, 166–188. doi:10.5589/m09-008

Moller, T., & Trumbore, B. (1997). Fast, minimum storage ray / triangle intersection. *Journal of Graphics Tools*, *2*, 21–28.

Monteith, J. L. (1972). Solar radiation and productivity in tropical ecosystems. *The Journal of Applied Ecology*, *9*, 747–766.

Monteith, J. L. (1977). Climate and the efficiency of crop production in Britain. *Philosophical Transactions of the Royal Society of London. Series B: Biological Sciences*, *281*, 277–294.

Moorthy, I., Miller, J. R., Berni, J. A. J., Zarco-Tejada, P., Hu, B., & Chen, J. (2011). Field characterization of olive (Olea europaea L.) tree crown architecture using terrestrial laser scanning data. *Agricultural and Forest Meteorology*, *151*, 204-214.

Morgenstern, K., Black, A. T., Humphreys, E. R., Griffis, T. J., Drewitt, G. B., Cai, T., Nesic, Z., Spittlehouse, D. L., & Livingston, N. J. (2004). Sensitivity and uncertainty of the carbon balance of a Pacific Northwest Douglas-fir forest during an El Niño/La Niña cycle. *Agricultural and Forest Meteorology*, *123*, 201–219. doi:10.1016/j.agrformet.2003.12.003

Morsdorf, F., Meier, E., Kötz, B., Itten, K. I., Dobbertin, M., & Allgöwer, B. (2004). LIDAR-based geometric reconstruction of boreal type forest stands at single tree level for forest and wildland fire management. *Remote Sensing of Environment*, *92*, 353–362. doi:10.1016/j.rse.2004.05.013

Næsset, E. (1997). Determination of mean tree height of forest stands using airborne laser scanner data. *ISPRS Journal of Photogrammetry and Remote Sensing*, *52*, 49–56. doi:10.1016/S0924-2716(97)83000-6

Næsset, E., Bollandsås, O. M., & Gobakken, T. (2005). Comparing regression methods in estimation of biophysical properties of forest stands from two different inventories using laser scanner data. *Remote Sensing of Environment*, *94*, 541–553. doi:10.1016/j.rse.2004.11.010

Næsset, E., & Gobakken, T. (2008). Estimation of above- and below-ground biomass across regions of the boreal forest zone using airborne laser. *Remote Sensing of Environment*, *112*, 3079–3090. doi:10.1016/j.rse.2008.03.004

Nelson, R., Jimenez, J., Schnell, C. E., Hartshorn, G. S., Gregoire, T. G., & Oderwald, R. (2000). Technical note: Canopy height models and airborne lasers to estimate forest biomass: Two problems. *International Journal of Remote Sensing*, *21*, 2153–2162. doi:10.1080/01431160050029486

Neubert, B. (2007). Approximate image-based tree modeling using particle flows. *ACM Transactions on Graphics*, *26*, article no. 88.

Nilson, T. (1971). A theoretical analysis of the frequency of gaps in plant stands. *Agricultural Meteorology*, *8*, 25–38.

Nilsson, M. (1996). Estimation of tree heights and stand volume using an airborne lidar system. *Remote Sensing of Environment*, *56*, 1–7.

Norman, A. J. M., & Jarvis, P. G. (1974). Photosynthesis in Sitka Spruce (Picea sitchensis (Bong.) Carr.). III. Measurements of canopy structure and interception of radiation. *Journal of Applied Ecology*, *11*, 375–398.

Norman, J. M. (1979). Modeling the complete crop canopy. In B. J. Barfield & J. F. Gerber (Eds.), *Modification of the aerial environment of plants* (pp. 249–277). St. Joseph, Michigan: American Society of Agricultural Engineers.

Norman, J. M., & Campbell, G. S. (1989). Canopy structure. In R W Pearcy, J. Ehleringer, H. A. Mooney, & P. W. Rundel (Eds.), *Plant Physiological Ecology* (Vol. 80, pp. 301–325). New York: Chapman and Hall. doi:10.2307/176572

Norman, J. M., & Jarvis, P. G. (1975). Photosynthesis in Sitka Spruce (Picea sitchensis (Bong.) Carr.). V. Radiation penetration theory and a test case. *Journal of Applied Ecology*, *12*, 839–878.

Oker-Blom, P. (1985). The influence of penumbra on the distribution of direct solar radiation in a canopy of Scots pine. *Photosynthetica*, *19*, 312–317.

Oker-Blom, P. (1986). Photosynthetic radiation regime and canopy structure in modeled forest stands. *Acta Forestalia Fennica*, *197*, 1–44.

Oker-Blom, P., Lappi, J., & Smolander, H. (1991). Radiation regime and photosynthesis of coniferous stands. In R B Myneni & J. Ross (Eds.), *Photon-Vegetation Interactions: Applications in Optical Remote Sensing and Plant Ecology* (pp. 441–467). Berlin Heidelberg: Springer-Verlag.

Parker, G. G., Harmon, M. E., Lefsky, M. A., Chen, J., Van Pelt, R., Weis, S. B., Thomas, S. C., Winner, W. E., Shaw, D. C., & Frankling, J. F. (2004). Three-dimensional structure of an old-growth Pseudotsuga-Tsuga canopy and its implications for radiation balance, microclimate, and gas exchange. *Ecosystems*, *7*, 440–453. doi:10.1007/s10021-004-0136-5

Parker, G. G., Lefsky, M. A., & Harding, D. J. (2001). Light transmittance in forest canopies determined using airborne laser altimetry and in-canopy quantum measurements. *Remote Sensing of Environment*, *76*(3), 298–309. doi:10.1016/S0034-4257(00)00211-X

Passioura, J. B. (1979). Accountability, philosophy and plant physiology. *Search*, *10*(10), 347–350.

Pearcy, R. W. (1990). Sunflecks and photosynthesis in plant canopies. *Annual Review of Plant Physiology and Plant Molecular Biology*, *41*, 421–453.

Pfeifer, N., & Winterhalder, D. (2004). Modelling of tree cross sections from terrestrial laser scanning data with free-form curves. *International Archives of Photogrammetry, Remote Sensing and Spatial Information Sciences*, *XXXVI* part 8/W2, 76–81.

Piccini, D., Littmann, A., Nielles-Vallespin, S., Zenge, M. O. (2011). Spiral phyllotaxis: the natural way to construct 3D radial trajectory in MRI. *Magnetic Resonance in Medicine*, *66*, 1049-1056.

Pitkanen, J., Maltamo, M., Hyyppa, J., & Yu, X. (2004). Adaptive methods for individual tree detection on airborne laser based canopy height model. *International Archives of Photogrammetry, Remote Sensing and Spatial Information Sciences*, *XXXVI* part 8/W2, 187–191.

Polhemus. (1993). 3SPACE FASTRAK users' manual, revision G. Colchester, VT, USA.

Poorter, H., Anten, N. P. R., & Marcelis, L. F. M. (2013). Physiological mechanisms in plant growth models: do we need a supra-cellular systems biology approach? *Plant, Cell & Environment*, *36*, 1673–90. doi:10.1111/pce.12123

Popescu, S. C., & Wynne, R. H. (2004). Seeing the trees in the forest: Using lidar and multispectral data fusion with local filtering and variable window size for estimating tree height. *Photogrammetric Engineering & Remote Sensing*, *70*, 859–604.

Popescu, S. C., Wynne, R. H., & Nelson, R. F. (2003). Measuring individual tree crown diameter with lidar and assessing its influence on estimating forest volume and biomass. *Canadian Journal of Remote Sensing*, *29*, 564–577. doi:10.5589/m03-027

Porcar-Castell, A., Pfündel, E., Korhonen, J. F. J., & Juurola, E. (2008). A new monitoring PAM fluorometer (MONI-PAM) to study the short- and long-term acclimation of photosystem II in field conditions. *Photosynthesis Research*, *96*, 173–9. doi:10.1007/s11120-008-9292-3

Pradal, C., Boudon, F., Nouguier, C., Chopard, J., & Godin, C. (2009). PlantGL: A Python-based geometric library for 3D plant modelling at different scales. *Graphical Models*, *71*, 1–21. doi:10.1016/j.gmod.2008.10.001

Prusinkiewicz, P., & Lindenmayer, A. (2004). *The algorithmic beauty of plants* (p. 240). Retrieved from http://algorithmicbotany.org/papers/abop/abop.pdf

Pueschel, P. (2013). The influence of scanner parameters on the extraction of tree metrics from FARO Photon 120 terrestrial laser scans. *ISPRS Journal of Photogrammetry and Remote Sensing*, *78*, 58–68.

Pueschel, P., Newnham, G., Rock, G., Udelhoven, T., Werner, W., & Hill, J. (2013). The influence of scan mode and circle fitting on tree stem detection, stem diameter and volume extraction from terrestrial laser scans. *ISPRS Journal of Photogrammetry and Remote Sensing*, *77*, 44–56.

Rahman, M. Z. A., & Gorte, B. G. H. (2009). Tree crown delineation from high resolution airborne lidar based on densities of high points. *International Archives of Photogrammetry, Remote Sensing and Spatial Information Sciences*, *XXXVIII*(part 3/W8).

Raumonen, P., Kaasalainen, M., Åkerblom, M., Kaasalainen, S., Kaartinen, H., Vastaranta, M., Holopainen, M., Disney, M., & Lewis, P. (2013). Fast automatic precision tree models from terrestrial laser scanner data. *Remote Sensing*, *5*, 491–520. doi:10.3390/rs5020491

Raven, P. H., Evert, R. F., & Eichhorn, S. E. (2005). *Biology of Plants* (p. 686). New York: W. H. Freeman and Company.

Ross, J., & Marshak, A. (1991). Monte Carlo methods. In R B Myneni & J. Ross (Eds.), *Photon-Vegetation Interactions: Applications in Optical Remote Sensing and Plant Ecology* (pp. 441–467). Berlin Heidelberg: Springer-Verlag.

Roujean, J.-L., Leroy, M., & Deschamps, P.-Y. (1992). A bidirectional reflectance model of the earth's surface for the correction of remote sensing data. *Journal of Geophysical Research*, *97,* 20455–20468.

Runions, A., Lane, B., & Prusinkiewicz, P. (2007). Modeling trees with a space colonization algorithm. In *Eurographics Workshop on Natural Phenomena* (pp. 63–70). Downloaded from: http://algorithmicbotany.org/papers/colonization.egwnp2007.pdf

Schaepman, M. E., Ustin, S. L., Plaza, A. J., Painter, T. H., Verrelst, J., & Liang, S. (2009). Earth system science related imaging spectroscopy—An assessment. *Remote Sensing of Environment*, *113*, S123–S137. doi:10.1016/j.rse.2009.03.001

Schaepman-Strub, G., Schaepman, M. E., Painter, T. H., Dangel, S., & Martonchik, J. V. (2006). Reflectance quantities in optical remote sensing—definitions and case studies. *Remote Sensing of Environment*, *103*, 27–42. doi:10.1016/j.rse.2006.03.002

Seidel, D., Fleck, S., & Leuschner, C. (2012). Analyzing forest canopies with ground-based laser scanning: A comparison with hemispherical photography. *Agricultural and Forest Meteorology*, *154-155*, 1–8. doi:10.1016/j.agrformet.2011.10.006

Seidel, D., Fleck, S., Leuschner, C., & Hammett, T. (2011). Review of ground-based methods to measure the distribution of biomass in forest canopies. *Annals of Forest Science*, *68*, 225–244. doi:10.1007/s13595-011-0040-z

Sharkey, T. D. (1985). Photosynthesis in intact leaves of C3 plants: Physics, physiology and rate limitations. *The Botanical Review*, *5*, 53–105.

Shih, F. Y., & Pu, C. C. (1995). A skeletonization algorithm by maxima tracking on Euclidean distance transform. *Pattern Recognition*, *28*, 331–341.

Siddiqi, K., & Pizer, S. M. (2008). *Medial Representations: Mathematics, Algorithms, and Applications*. Berlin Heidelberg: Springer.

Sinoquet, H., Thanisawanyangkura, S., Mabrouk, H., & Kasemsap, P. (1998). Characterization of the light environment in canopies using 3D digitising and image processing. *Annals of Botany*, *82*, 203–212.

Soudani, K., Hmimina, G., Delpierre, N., Pontailler, J.-Y., Aubinet, M., Bonal, D., Caquet, B., De Grandcourt, A., Burban, D., Flechard, C., Guyon, D., Granier, A., Gross, P., Heinesh, B., Longdoz, B., Loustau, D., Moureaux, C., Ourcival, J.-M., Rambal, S., Saint André, L., & Dufrêne, E. (2012). Ground-based network of NDVI measurements for tracking temporal dynamics of canopy structure and vegetation phenology in different biomes. *Remote Sensing of Environment*, *123*, 234–245. doi:10.1016/j.rse.2012.03.012

Stenberg, P. (1995a). Penumbra in within-shoot and between-shoot shading in conifers and its significance for photosynthesis. *Ecological Modelling*, *77*, 215–231.

Stenberg, P., Linder, S., & Smolander, H. (1995b). Variation in the ratio of shoot silhouette area to needle area in fertilized and unfertilized Norway spruce trees. *Tree physiology*, *15*, 705–12.

Strahler, A. H., & Jupp, D. L. B. (1991). Geometric-optical modeling of forests as remotely-sensed scenes composed of three-dimensional, discrete objects. In R B Myneni & J. Ross (Eds.), *Photon-vegetation interactions: Applications in optical remote sensing and plant ecology* (pp. 415–440). Berlin Heidelberg: Springer-Verlag.

Strahler, A. H., Jupp, D. L. B., Woodcock, C. E., Schaaf, C. B., Yao, T., Zhao, F., Yang, X., Lovell, J., Culvenor, D., Newnham, G., Ni-Meister, W., & Boykin-Morris, W. (2008). Retrieval of forest structural parameters using a ground-based lidar instrument (Echidna ®). *Canadian Journal of Remote Sensing*, *34*, S426–S440. doi:10.5589/m08-046

Suffern, K. (2007). *Ray tracing from the ground up* (p. 784). Wellesley, Massachusetts: A K Peters/CRC Press.

Tan, P., Zeng, G., Wang, J., & Kang, S. B. (2006). Image-based tree modeling. *ACM Transactions on Graphics*, *26*, article no. 87.

Timmermans, J., Su, Z., van der Tol, C., Verhoef, A., & Verhoef, W. (2013). Quantifying the uncertainty in estimates of surface–atmosphere fluxes through joint evaluation of the SEBS and SCOPE models. *Hydrology and Earth System Sciences*, *17*, 1561–1573. doi:10.5194/hess-17-1561-2013

Tucker, C. J., & Sellers, P. J. (1986). Satellite remote sensing of primary production. *International Journal of Remote Sensing*, *7*, 1395–1416. doi:10.1080/01431168608948944

Ustin, S. L., Roberts, D. A., Gamon, J. A., Asner, G. P., & Green, R. O. (2004). Using imaging spectroscopy to study ecosystem processes and properties. *BioScience*, *54*, 523–534.

Van der Tol, C., Verhoef, W., & Rosema, A. (2009). A model for chlorophyll fluorescence and photosynthesis at leaf scale. *Agricultural and Forest Meteorology*, *149*, 96–105. doi:10.1016/j.agrformet.2008.07.007

Van der Zande, D., Stuckens, J., Verstraeten, W. W., Mereu, S., Muys, B., & Coppin, P. (2011). 3D modeling of light interception in heterogeneous forest canopies using ground-based LiDAR data. *International Journal of Applied Earth Observation and Geoinformation*, *13*, 792–800. doi:10.1016/j.jag.2011.05.005

Van Leeuwen, M., Coops, N. C., Hilker, T., Wulder, M. A., Newnham, G. J., & Culvenor, D. S. (2013). Automated reconstruction of tree and canopy structure for modeling the internal canopy radiation regime. *Remote Sensing of Environment*, *136*, 286–300. doi:10.1016/j.rse.2013.04.019

Van Leeuwen, M., Coops, N. C., Newnham, G. J., Hilker, T., Culvenor, D. S., & Wulder, M. A. (2011b). Stem detection and measuring DBH using terrestrial laser scanning. In *SilviLaser 2011*. October 16-19, Hobart, Australia.

Van Leeuwen, M., Coops, N. C., & Wulder, M. A. (2010). Canopy surface reconstruction from a LiDAR point cloud using Hough transform. *Remote Sensing Letters*, *1*, 125–132. doi:10.1080/01431161003649339

Van Leeuwen, M., Hilker, T., Coops, N. C., Frazer, G., Wulder, M. A., Newnham, G. J., & Culvenor, D. S. (2011a). Assessment of standing wood and fiber quality using ground and airborne laser scanning: A review. *Forest Ecology and Management*, *261*, 1467–1478. doi:10.1016/j.foreco.2011.01.032

Van Leeuwen, M., & Nieuwenhuis, M. (2010). Retrieval of forest structural parameters using LiDAR remote sensing. *European Journal of Forest Research*, *129*, 749–770. doi:10.1007/s10342-010-0381-4

Verhoef, W. (1984). Light scattering by leaf layers with application to canopy reflectance modeling: The SAIL model. *Remote Sensing of Environment*, *16*, 125–141. doi:10.1016/0034-4257(84)90057-9

Verroust, A., & Lazarus, F. (2000). Extracting skeletal curves from 3D scattered data. *The Visual Computer*, *16*, 15–25. doi:10.1007/PL00007210

Vogel, H. (1979). A better way to construct the sunflower head. *Mathematical Biosciences*, *44*, 179-189.

Vosselman, G., & Dijkman, S. (2001). 3D building reconstruction from point clouds and ground plans. *International Archives of Photogrammetry, Remote Sensing and Spatial Information Sciences*, *XXXIV* part 3/W4, 22–24.

Wada, M., Kagawa, T., & Sato, Y. (2003). Chloroplast movement. *Annual Review of Plant Biology*, *54*, 455–68. doi:10.1146/annurev.arplant.54.031902.135023

Wang, Y.-P., & Jarvis, P. G. (1990a). Description and validation of an array model - MAESTRO. *Agricultural and Forest Meteorology*, *51*, 257–280.

Wang, Y.-P., & Jarvis, P. G. (1990b). Influence of crown structural properties on PAR absorption, photosynthesis, and transpiration in Sitka spruce: application of a model (MAESTRO). *Tree physiology*, *7*, 297–316. Retrieved from http://www.ncbi.nlm.nih.gov/pubmed/14972925 (Last accessed on December 31, 2013)

Weber, J., & Penn, J. (1995). Creation and rendering of realistic trees. In *SIGGRAPH 95* (pp. 119–128). New York: ACM.

Wehr, A., & Lohr, U. (1999). Airborne laser scanning—an introduction and overview. *ISPRS Journal of Photogrammetry and Remote Sensing*, *54*, 68–82. doi:10.1016/S0924-2716(99)00011-8

Weinacker, H., Koch, B., Heyder, U., & Weinacker, R. (2004). Development of filtering, segmentation and modelling modules for lidar and multispectral data as a fundament of an automatic forest inventory system. *International Archives of Photogrammetry, Remote Sensing and Spatial Information Sciences*, *XXXVI* part 8/W2 , 50–55.

Weiss, M., Troufleau, D., Baret, F., Chauki, H., Prévot, L., Olioso, A., Bruguier, N., & Brisson, N. (2001). Coupling canopy functioning and radiative transfer models for remote sensing data assimilation. *Agricultural and Forest Meteorology*, *108*, 113–128. doi:10.1016/S0168-1923(01)00234-9

Welles, J. M., & Norman, M. (1991). Photon transport in discontinuous canopies: A weighted random approach. In R B Myneni & J. Ross (Eds.), *Photon-Vegetation Interactions: Applications in Optical Remote Sensing and Plant Ecology* (pp. 389–414). Berlin Heidelberg: Springer-Verlag.

Widlowski, J.-L. (2010). An overview of two decades of systematic evaluation of canopy radiative transfer models. In *ISPRS Archives XXXVIII part 7B* (pp. 648–653).

Widlowski, J.-L., Robustelli, M., Disney, M., Gastellu-Etchegorry, J.-P., Lavergne, T., Lewis, P., North, P.R.J., Pinty, B., Thompson, R., & Verstraete, M. M. (2008). The RAMI On-line Model Checker (ROMC): A web-based benchmarking facility for canopy reflectance models. *Remote Sensing of Environment*, *112*, 1144–1150. doi:10.1016/j.rse.2007.07.016

Widlowski, J.-L., Taberner, M., Pinty, B., Bruniquel-Pinel, V., Disney, M., Fernandes, R., Gastellu-Etchegorry, J.-P., Gobron, N., Kuusk, A., Lavergne, T., Leblanc, S., Lewis, P. E., Martin, E., Mõttus, M., North, P.R.J., Qin, W., Robustelli, M., Rochdi, N., Ruiloba, R., Soler, C., Thompson, R., Verhoef, W., Verstraete, M. M., & Xie, D. (2007). Third Radiation Transfer Model Intercomparison (RAMI) exercise: Documenting progress in canopy reflectance models. *Journal of Geophysical Research*, *112*, D09111. doi:10.1029/2006JD007821

Widlowski, J.-L., Pinty, B., Lavergne, T., Verstraete, M. M., & Gobron, N. (2006). Horizontal radiation transport in 3-D forest canopies at multiple spatial resolutions: Simulated impact on canopy absorption. *Remote Sensing of Environment*, *103*, 379–397. doi:10.1016/j.rse.2006.03.014

Wulder, M. A., Bater, C. W., Coops, N. C., Hilker, T., & White, J. C. (2008). The role of LiDAR in sustainable forest management. *The Forestry Chronicle*, *84*, 807–826.

Wulder, M. A., White, J. C., Nelson, R. F., Næsset, E., Ørka, H. O., Coops, N. C., Hilker, T., Bater, Ch. W., & Gobakken, T. (2012). Lidar sampling for large-area forest characterization: A review. *Remote Sensing of Environment*, *121*, 196–209. doi:10.1016/j.rse.2012.02.001

Yang, W., Ni-Meister, W., Kiang, N. Y., Moorcroft, P. R., Strahler, A. H., & Oliphant, A. (2010). A clumped-foliage canopy radiative transfer model for a global dynamic terrestrial ecosystem model II: Comparison to measurements. *Agricultural and Forest Meteorology*, *150*, 895–907. doi:10.1016/j.agrformet.2010.02.008

Yang, X., Strahler, A. H., Schaaf, C. B., Jupp, D. L. B., Yao, T., Zhao, F., Wang, Z., Culvenor, D. S., Newnham, G. J., Lovell, J. L., Dubayah, R. O., Woodcock, C., & Ni-Meister, W. (2013). Three-dimensional forest reconstruction and structural parameter retrievals using a terrestrial full-waveform lidar instrument (Echidna®). *Remote Sensing of Environment*, *135*, 36–51. doi:10.1016/j.rse.2013.03.020

Yao, T., Yang, X., Zhao, F., Wang, Z., Zhang, Q., Jupp, D., Lovell, J., Culvenor, D., Newnham, G., Ni-Meister, W., Schaaf, C., Woodcock, C., Wang, J., Li, X., & Strahler, A. (2011). Measuring forest structure and biomass in New England forest stands using Echidna ground-based lidar. *Remote Sensing of Environment*, *115*, 2965–2974. doi:10.1016/j.rse.2010.03.019

Ying, H., Zhou, F., Shields, A., Muzik, O., Wu, D., & Heath, E. (2004). A novel computerized approach to enhancing lung tumor detection in whole-body PET images. *Annual International Conference of the IEEE Engineering in Medicine and Biology Society. IEEE Engineering in Medicine and Biology Society*, *3*, 1589–92. doi:10.1109/IEMBS.2004.1403483

Yuan, J., Wang, D., Wu, B., Yan, L., & Li, R. (2011). LEGION-based automatic road extraction from satellite imagery. *IEEE Transactions on Geoscience and Remote Sensing*, *49*, 4528–4538. doi:10.1109/TGRS.2011.2146785

Appendix

A.1. Sensitivity analysis

A.1.1. Stem detection

The sensitivity of stem detection to changes in parameter values was analysed using plot-centre scans and by varying one parameter over specified ranges (δ = 0.1, 0.2, 0.3, 0.4, 0.5 m; *r* = 0.7, 0.8, 0.9, 0.99, 0.995; ξ = 5, 10, 15, 20, 35°; n_{MR} = 6, 12, 24, 36, 42) while the remaining parameters were kept fixed (δ = 0.3m; *r* = 0.95; ξ = 15°; n_{MR} = 12). Table A.1 summarizes the commission and omission errors caused by changes in δ, *r*, and n_{MR}. Filtering for ξ only reduced errors of commission in some scans, whereas it had no effect in others including the plot-center scans.

Table A.1: Sensitivity analysis of parameters *δ*, *r*, and n_{MR} on percentage of correctly detected stems, and errors of commission and omission. Values for *δ*, n_{MR}, or *r* were changed one at a time, while remaining parameters were kept constant. Constants used for sensitivity analysis were *δ*=0.3m, n_{MR}=12, *r*=0.95.

δ (m)	**0.1**	**0.2**	**0.3**	**0.4**	**0.5**	**trend**
Correctly detected	73.97%	82.53%	82.88%	83.90%	83.90%	+
Errors of commission	19.52%	14.73%	14.73%	12.67%	8.90%	-
Errors of omission	26.03%	17.47%	17.12%	16.10%	16.10%	-
n_{MR}	**6**	**12**	**24**	**36**	**42**	
Correctly detected	89.73%	81.85%	75.34%	66.78%	64.04%	-
Errors of commission	61.30%	16.10%	0.34%	0.00%	0.00%	-
Errors of omission	10.27%	18.15%	24.66%	33.22%	35.96%	+
r	**0.7**	**0.8**	**0.9**	**0.99**	**0.995**	
Correctly detected	82.88%	82.88%	82.88%	82.88%	82.88%	0
Errors of commission	32.53%	32.19%	25.68%	15.41%	2.74%	-
Errors of omission	17.12%	17.12%	17.12%	17.12%	17.12%	0

A.1.2. Arbaro parameters

A listing of the Arbaro parameters that were not derived from point cloud data, but that have a significant role in the construction of the geometrically explicit scenes is provided in Table A.2. Values for these parameters were obtained from field inventory data. The sensitivity of these Arbaro parameters on radiative transfer simulations was assessed by conducting a set of simulations using an arbitrary stem map and random tree heights, and by changing Arbaro parameter values by -20% to +20% (in steps of 10%). One Arbaro parameter was changed at a time, while remaining parameters were kept constant. The sensitivity analysis shows that BaseSize, defining the height of the branch free bole section and canopy depth, is the most sensitive parameter. First order down angle (1DownAngle) and its distribution (1DownAngleV) with canopy depth, both parameters regulating the angle between a branch and the main stem, causes estimates of cumulative hit distributions to vary by 16% and 8% of total absorbed radiation, respectively. The six most important Arbaro parameters were further investigated and the effect of individual parameters and their interactions are shown in Figure A.1. Along the diagonal, the effect of changing one parameter is shown. The cumulative hit distribution using the reported values is represented by a thick line and the two thinner lines indicate the range in simulation outcomes caused by changing the respective parameter value. The upper half of the matrix lists these effects for changing two parameters at a time. The lower half of the matrix plots the range in simulation outcomes against canopy depth so that the black line in plots (i,j) correspond with plots (j,i) and the blue and red lines correspond with the plots along the diagonal. For example, a change in BaseSize of +/- 20% (0.32 to 0.48) causes a change in the cumulative hit distribution from 0.18 to 0.47 around the 21-m height, indicating the significance of this parameter on the derived hit distribution profiles. In addition, varying both the value of BaseSize and 1DownAngle simultaneously causes a greater range in model outcomes than changing either of the parameters alone. This effect is disaggregated to individual parameter contributions in the lower half of the matrix. The graphs show a decrease in parameter sensitivity with branching order.

Table A.2: Parameter values used in the Arbaro architectural tree modeling software.

level 0 trunk	Value*	Level 1 branches	Value*	Level 2 branches	Value*
Shape	conical (n/a)	1DownAngle	90° (16%)	2DownAngle	45 ° **
levels	3 (n/a)	1DownAngleV	-50 (8%)	2Rotate	-90° (3%)
BaseSize	0.4 (30%)	1Rotate	140° **	2CurveRes	5 **
AttractionUp	-0.1 **	1CurveRes	25 (1%)		
		1Curve	-40° (2%)		

* Parameter sensitivity is shown between parenthesis and is expressed as the difference in cumulative hit distribution (x100%) caused by a +20% and -20% change of the listed parameter value. Sensitivities were computed for one parameter at a time, while remaining model parameters were kept constant.

** Parameters for which sensitivity was less than 1%.

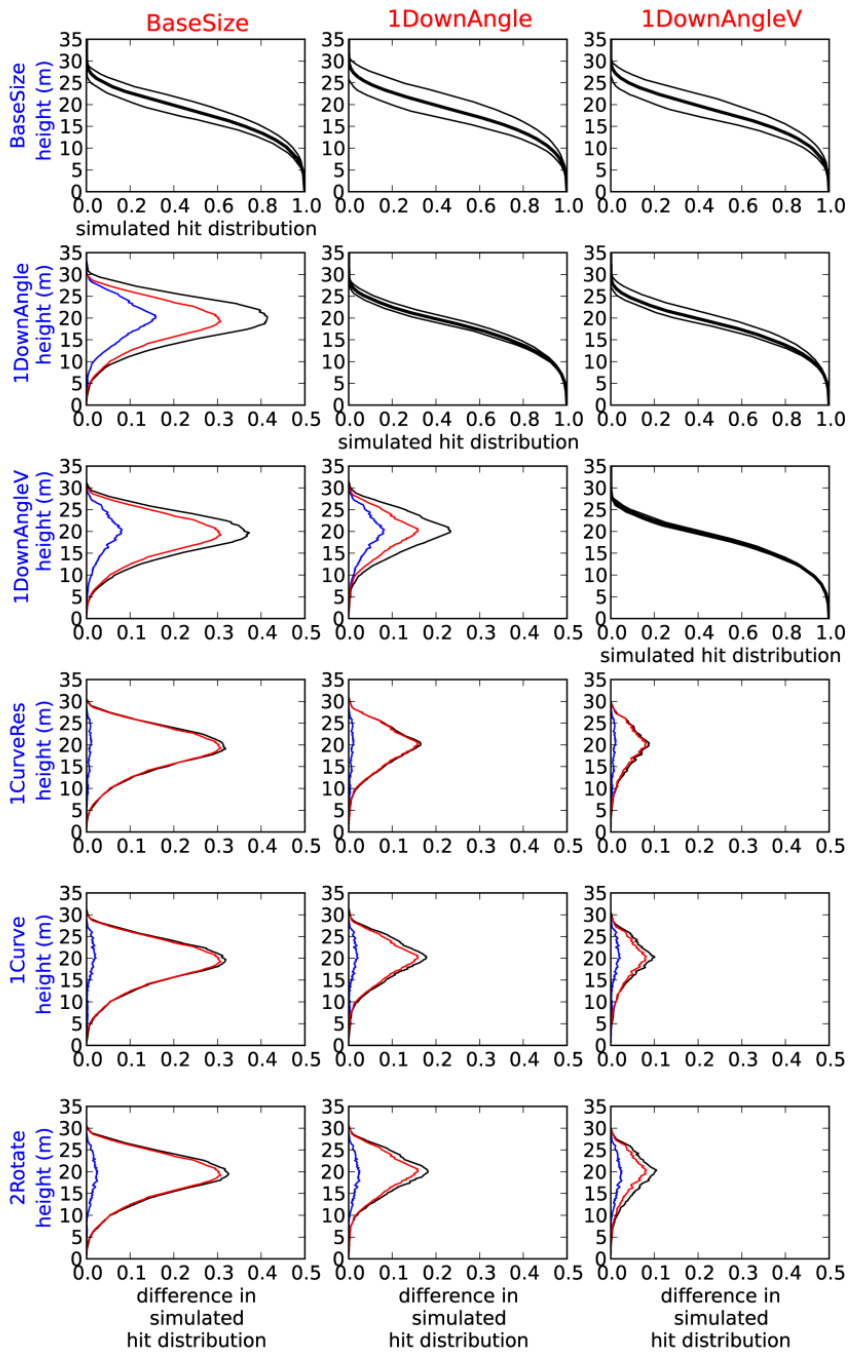

Figure A.1: Arbaro parameter sensitivity analysis. Variation induced by the six most important parameters is displayed along the diagonal of the matrix of plots, while effects of co-varying two parameters on the cumulative hit distribution is displayed in the upper half, and the observed range in model outcome in the lower half.

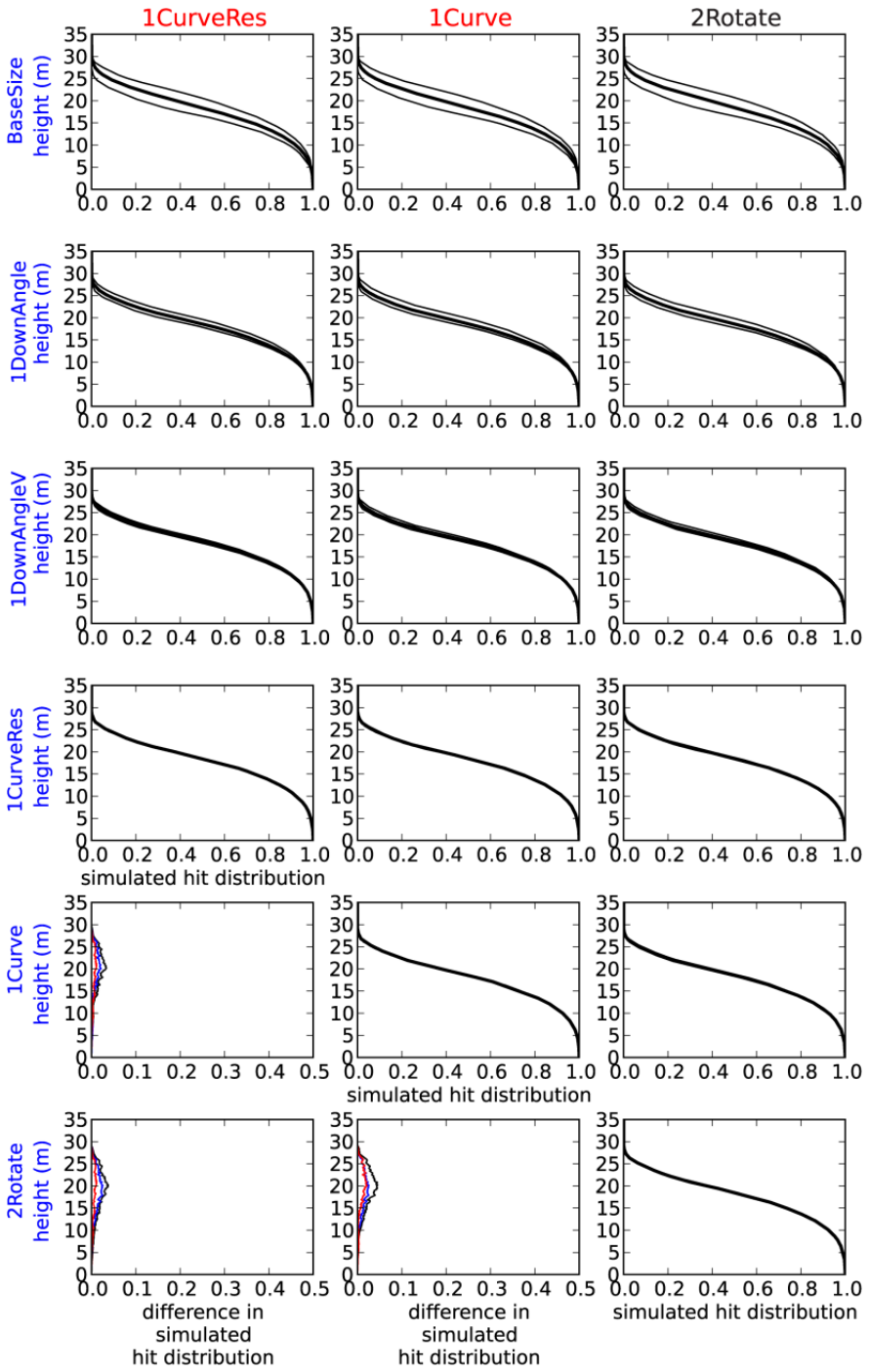

Figure A.1 *(continued)*: Arbaro parameter sensitivity analysis. Variation induced by the six most important parameters is displayed along the diagonal of the matrix of plots, while effects of co-varying two parameters on the cumulative hit distribution is displayed in the upper half, and the observed range in model outcome in the lower half.

A.1.3. Gap fraction

Besides the geometry of the mesh model, gap fraction is an important parameter and regulates un-collided transmission through the planar polygons and thus the hit distribution. Varying $g(\vartheta_i)$ from 5 to 30% resulted in a maximum difference in hit distribution at 18 m of 0.02 suggesting that most transmission occurs between crowns and outside the branch silhouettes. Values used for $g(\vartheta_i)$ are among the lower bound observed for a 30-year-old Norway spruce stand in Sweden (Stenberg et al., 1995).

An analysis of the effects of varying foliage densities on the radiation transmission properties of the virtual canopies was conducted after separating sun and shade facets. This was achieved by computing for every facet in the scene the probability of a direct line of sight in directions from a set of 1,064 uniformly distributed directions across the hemisphere. Using computed sun azimuth and zenith angles, a stratification of facets into sun and shade was made based on whether the facets were in direct line of sight with the sun (Hilker et al. 2010a). The effects of different foliage densities on the hit distribution were then investigated by altering the gap fractions of sun and shade facets (Figure A.2). The lower value is the gap fraction for sun facets and the higher value for shade facets. We can see that the impact of changing foliage densities is relatively small compared to effects of some other model parameters (e.g. BaseSize), suggesting that crown shape has a strong influence on the observed radiation profiles.

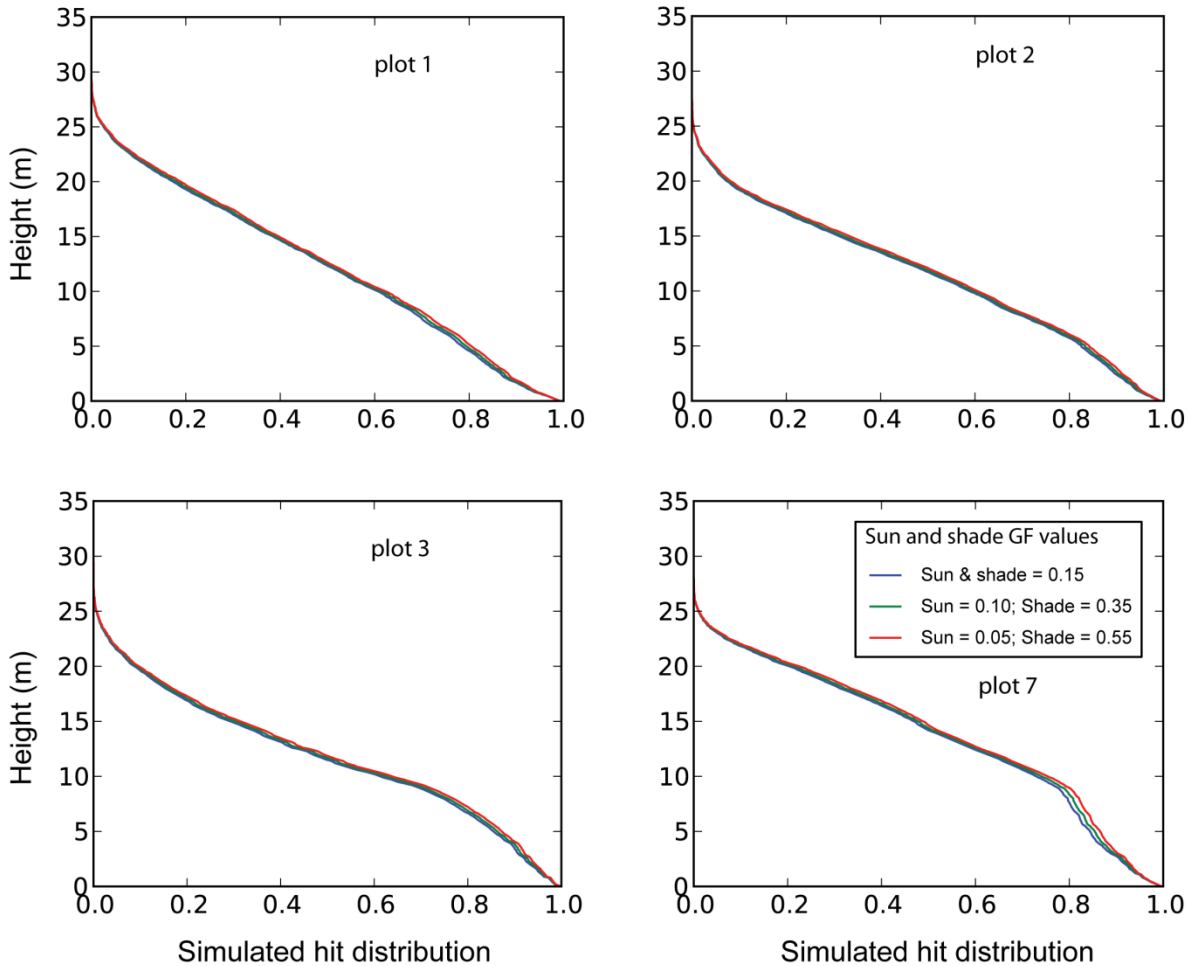

Figure A.2: Effect of altering distributions for gap fraction $g(\vartheta_i)$ on the cumulative hit distribution for all four plots.

A.2. Ray tracer details

To provide a better understanding of the ray tracer developed for this study, this appendix provides a brief overview of its main components and underlying algebra of radiation transport.

A.2.1. Radiation transport

When computing reflectance from a certain surface element into directions (φ_r, θ_r), the intrinsic scattering properties of the material under consideration in combination with the projected solid angle (Arecchi et al. 2007) are of principal importance. In the current ray tracer, reflectance and transmittance are described for a Lambertian surface, that is a surface that reflects the same amount of radiation [W m^{-2} sr^{-1}] in all directions, and its intensity [W m^{-2}] drops with the cosine normal angle (Schaepman-Strub et al. 2006). Thus, the probability of a photon hitting a Lambertian surface and reflecting (transmitting) in a certain direction is a probability density function whose values decrease with the cosine of the angle between the incident path of the photon and the surface normal.

The bidirectional reflectance distribution function (BRDF) [sr^{-1}] of a surface describes the distribution of reflection over a hemisphere of outgoing directions (φ_r, θ_r) for a beam that is incident on the surface under direction (φ_i, θ_i). The BRDF is defined as the ratio of radiance L_r [W m^{-2} sr^{-1}] that is reflected from the surface and irradiance E_i [W m^{-2}] that is incident on the surface. For any given surface, the BRDF integrated over the viewing hemisphere sums to the surface reflectance, ρ_d [unitless]. A Lambertian surface has a constant BRDF of ρ_d/π, so that when integrated over the full hemisphere (Suffern, 2007):

$$\int_{\phi=0}^{2\pi}\int_{\theta=0}^{\frac{\pi}{2}} f_{Lambert} \cdot sin(\theta) \cdot cos(\theta) \cdot d\theta \cdot d\phi \cdot dA =$$

$$2\pi \cdot \rho_d/\pi \cdot \int_{\theta=0}^{\frac{\pi}{2}} sin(\theta) \cdot cos(\theta) \cdot d\theta \cdot dA = 2\pi \cdot \rho_d/\pi \cdot \frac{1}{2} \cdot dA = \rho_d \cdot dA$$

The reflected radiance into any one direction (φ_r, θ_r) from such a surface is:

$$L_r = \frac{1}{\pi} \cdot \rho_d \cdot E_i = \frac{1}{\pi} \cdot \rho_d \cdot \int_{\omega} L_i \cdot dA \cdot cos(\theta_i) \cdot d\omega$$

Furthermore, it can be observed analytically that the reflected intensity of such a surface decreases with increasing normal angle:

$$\frac{d\Phi_r}{dA} = \frac{1}{\pi} \cdot \rho_d \cdot E_i \cdot cos(\theta_r) = \frac{1}{\pi} \cdot \rho_d \cdot cos(\theta_r) \cdot \int_{\omega} L_i \cdot dA \cdot cos(\theta_i) \cdot d\omega$$

The bidirectional reflectance of a Lambertian target can thus be described by the intensity of photons hitting a surface element and a cosine-weighted probability of reflecting into the direction (φ_r, θ_r). Transmittance is described similarly using a Bidirectional Transmittance Distribution Function (BTDF), that for a Lambertian target equals to $\frac{1}{\pi} \cdot \tau_d$, where τ_d is the materials collided transmittance.

A.2.2. Monte Carlo Ray Tracing

The ray tracer is implemented in the Python programming language, follows object-oriented coding design and was developed specifically for computing P_{hit} and P_{gap} but has been extended to compute absorptance and transmittance for model validation purposes. The ray tracer simulates absorptance and transmittance by tracing individual photon paths within a virtual scene of Lambertian targets that are all a circular or triangular shape. Intersections of photon paths with the scene elements are computed largely following Moller and Trumbore (1997) and methodology explained by D. Sunday (http://geomalgorithms.com/a06-_intersect-2.html, last accessed on December 31, 2013). Photons originate from a reference plane that is oriented horizontally and that is just above the highest element in the scene. When photons collide with the scene elements, their fate as to being absorbed or scattered is evaluated from the materials properties ρ_d, and τ_d and in the case of either reflection or transmission a new direction vector is sampled from a cosine weighted hemispherical distribution

(Suffern 2007). A new photon is generated each time a previous photon is absorbed or bounced outside the scene. Alternatively, the ray tracer provides for the simulation of P_{hit} and P_{gap} by generating rays that upon intersection with the scene are partially obstructed and for which uncollided transmittance can be computed based on a gap fraction assigned to each surface element.

A.2.2.1. Validation

Validation of the ray tracer was achieved against the Radiative Transfer Model Intercomparison (RAMI) Online Model Checker (ROMC) (Widlowski et al. 2008) that was designed to find consistency among existing radiave transfer models through the development and use of benchmark data sets. The model's performance was evaluated against four heterogeneous baseline scenarios: HET01_DIS_UNI_RED and HET01_DIS_UNI_NIR and using zenith angles of 20 and 50 degrees. For each scenario, the fraction of radiation entering the scene that is absorbed by foliage elements (*fabs*) and the fraction of radiation impinging on the background surface (*ftran*) were computed from 4 to 10 million simulated photons. All *fabs* simulations showed consistency with the ROMC-reference to within ~1%. Differences with the ROMC baseline for *ftran* were observed for the Near-Infrared case and the simulations showed a constant bias of around 4%.

A.2.2.2. Deriving gap/hit probability

The ray tracer can be used to derive gap and hit probabilities for scenes that have materials specified with certain gap fractions, i.e. the degree of porosity of a surface element from which un-collided transmission results. Individual elements that are intersected by a ray are ordered with respect to their distance from the ray's source and a hit probability is computed at every intersection based on the cosine angle with the element and the element's gap fraction. At every intersection i, in sorted order, the transmitted portion of the ray is computed as $I_i \cdot (1 - P_{hit})$, where I_i is the payload that propagates un-collided through intersection i-1 and I_0 is the payload of the primary ray, so that values I_0 of all primary rays originating from a hemisphere of light sources are equal and sum to one.

A.3. Computing hemispherical down-welling radiance

Using diffuse and total irradiance from 400 to 700 nm (PAR band) the direct irradiance was computed for every half hour:

$$E_{direct} = E_{total} - E_{diffuse}$$

Down-welling diffuse radiance was assumed to be constant throughout the hemisphere, and was computed from diffuse irradiance as:

$$L_{diffuse} = \frac{E_{diffuse}}{2\pi \cdot \int_0^{\pi/2} cos(\theta) \cdot sin(\theta)\, d\theta} = \frac{E_{diffuse}}{\pi}$$

Direct radiance was then assigned to the hemispherical sample that was located closest to the sun's position, determined using a KD-tree, and direct radiance was computed from direct irradiance by correcting for the sun zenith angle that was computed using a solar calculator, and the average solid angle spanned by the hemispherical samples:

$$L_{direct} = \frac{E_{direct}}{cos(\theta_{sun}) \cdot (2\pi/n)}$$

To test the accuracy of the methods, total irradiance was computed by integrating radiance over the full hemisphere and this value was compared with measured irradiance for all time steps involved in the study (Figure A.3). The comparison shows some inaccuracy that result from the hemispherical sampling chosen that, however, was found acceptable given the improvement in computational speed this sampling provides.

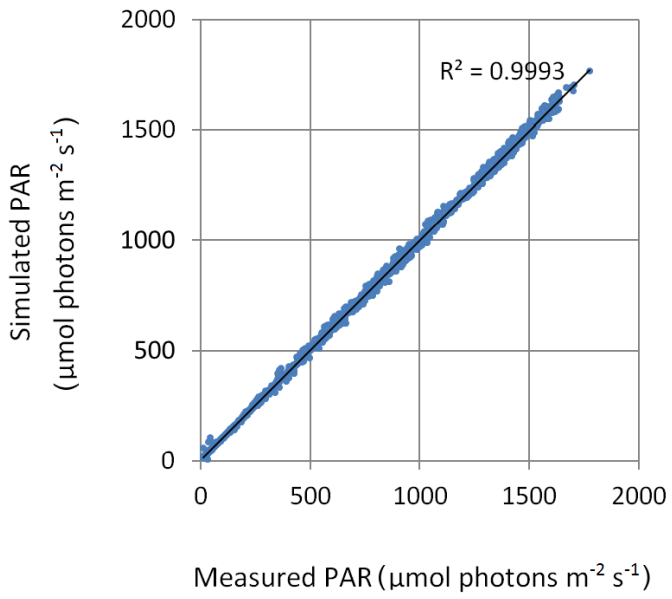

Figure A.3: Demonstration of the measured irradiance (x-axis) and test results obtained by integrating simulated radiance over the full hemisphere (y-axis).

A.4. Computing IPAR

The amount of irradiance incident on a flat, horizontal panel can be computed as the integration over the hemispherical down-welling radiance as:

$$IPAR = \int \int L(\phi, \theta) \cdot cos(\theta) \cdot sin(\phi) \; d\phi d\theta$$

Using numerical integration, the integral can be solved as a summation using a fixed step size for azimuth and zenith angles. However, using fixed step sizes, the sampling density towards the zenith increases thereby reducing the cost efficiency of computation. When a set of n hemispherical samples are distributed following the Capitulum sampling (e.g. Piccini et al. 2011; Vogel, 1979), the solid angle covered per sample can be assumed to be approximately constant ($\approx 2\pi/n$) and the hemispherical integration can be computed as:

$$IPAR \approx \frac{2\pi}{n} \cdot \sum_{i=0}^{n} L_i \cdot cos(\theta_i)$$

where the index i symbols the rank of the hemispherical sample, L_i the radiance coming from sample i [µmol m^{-2} s^{-1} sr^{-1}] and θ_i the zenith angle of the sample. When a panel p is tilted, however, the angle between the surface normal and the hemispherical sample (denoted $\alpha_{i \to p}$) needs to be considered and this is computed as the dot product between the facet normal vector $\boldsymbol{p}$ and the direction vector of incident radiation, $\boldsymbol{i}$:

$$IPAR \approx \frac{2\pi}{n} \cdot \sum_{i=0}^{n} L_i \cdot cos(\alpha_{i \to p})$$

$$cos(\alpha_{i \to p}) = \frac{\boldsymbol{p} \cdot \boldsymbol{i}}{\|\boldsymbol{p}\| \|\boldsymbol{i}\|}$$

If the panel is porous, the un-collided transmittance can be computed from the gap fraction of the panel $GF_{\perp}$ and the angle of incidence:

$$\tau_{uncollided} = GF_{\perp} \cdot \left|cos\left(\alpha_{i \to p}\right)\right|$$

For a given spatial configuration of N porous panels, the probability of a first hit from direction (ϕ_i, θ_i) on panel p is equal to the probability of having a gap through the set of panels S that fall on an intersecting line that starts from a point on panel p into direction (ϕ_i, θ_i), times the probability of colliding with panel p given the incidence angle:

$$P_{hit}(p, \phi_i, \theta_i) = \left(1 - \tau_{uncollided}(p, \phi_i, \theta_i)\right) \cdot \prod_{q}^{\substack{for\ all \\ q \in S}} \tau_{uncollided}\,(q, \phi_i, \theta_i)$$

The irradiance incident on a porous panel p received from a specific hemispherical sample can then be computed as:

$$IPAR(p, \phi_i, \theta_i) \approx \frac{2\pi}{n} \cdot P_{hit}(p, \phi_i, \theta_i) \cdot L_i \cdot cos\left(\alpha_{i \to p}\right)$$

and can be compared against measurements (Figure A.4).

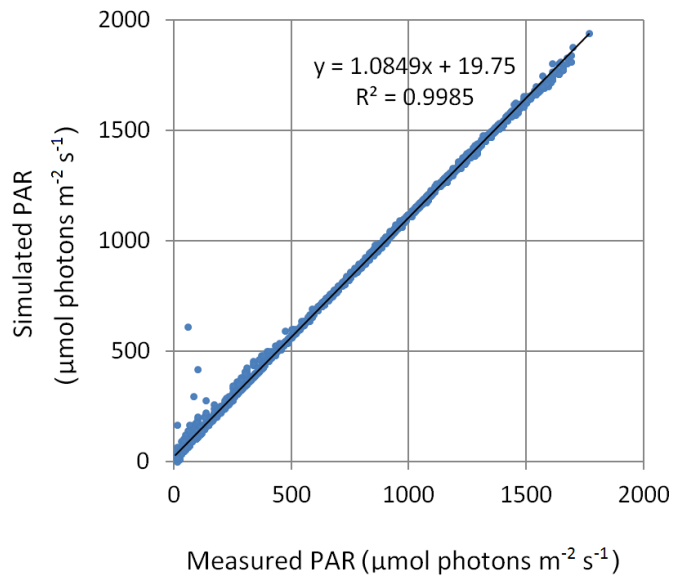

Figure A.4: Correlation and bias between simulated and measured incident PAR.